UNICA

UNIVERSITÀ
DEGLI STUDI
DI CAGLIARI

Ph.D. DEGREE IN
Industrial Engineering

Cycle XXXVIII

TITLE OF THE Ph.D. THESIS

Innovative energy systems and processes based on hydrogen from RES and its derivatives in the energy transition process

Scientific Disciplinary Sector(s)

ING-IND/09

Ph.D. Student:	Ing. Davide Micheletto
Supervisor	Prof. Ing. Daniele Cocco
Co-Supervisor	Ing. Luca Migliari

Final exam. Academic Year 2024/2025
Thesis defence session: February 2026

Part of this thesis has been based on works and results published in the following peer-reviewed papers:

- L. Migliari, D. Micheletto, D. Cocco, Journal of Energy Storage, Green hydrogen generation for mitigating the impact of curtailment in floating photovoltaic - pumped hydro energy storage (FPV-PHES) systems, 2025, DOI: 10.1016/j.est.2025.117997
- L. Migliari, D. Micheletto, D. Cocco, A hydrogen-fuelled compressed air energy storage system for flexibility reinforcement and variable renewable energy integration in grids with high generation curtailment, Energy Conversion and Management, 2024, DOI: 10.1016/j.enconman.2024.118308
- D. Micheletto, L. Migliari, D. Cocco, Assessing the energy and water impacts of seawater electrolysis for green hydrogen production, 37th International Conference on Efficiency Cost Optimization Simulation and Environmental Impact of Energy Systems ECOS 2024, 2024, DOI: 10.52202/077185-0111
- L. Migliari, D. Micheletto, M. Marchionni, D. Cocco, Integration of Floating Photovoltaics and Pumped Hydro Energy Storage with Water Electrolysis for Combined Power and Hydrogen Generation, Journal of Physics Conference Series, 2024, DOI: 10.1088/1742-6596/2893/1/012007
- D. Micheletto, L. Migliari, G. Cau, D. Cocco, Minimizing LCOA in green ammonia production: optimization of components size and scheduling under varying curtailment scenarios, Journal of Physics Conference Series, 2025, DOI: 10.1088/1742-6596/3143/1/012006
- L. Migliari, D. Micheletto, D. Cocco, Performance Analysis of a Diabatic Compressed Air Energy Storage System Fueled with Green Hydrogen, Energies, 2023, DOI: 10.3390/en16207023

Acknowledgements

I want to thank my supervisor, Prof. Daniele Cocco, my co-supervisor, Ing. Luca Migliari, and the professors and researchers of the Department of Mechanical, Chemical, and Materials Engineering (DIMCM) of the University of Cagliari for the invaluable guidance and support that helped me progress as a Ph.D. student.

I am grateful to Società Chimica Assemini S.r.l., not only for co-funding my Ph.D. but also for providing the conditions to carry out this research. I especially want to thank Dr. Domenico Greco, Ing. Ignazio Meloni, Dr. Piera Verrocchio, and the colleagues and friends I met there.

I would also like to thank the Centro Nacional del Hidrógeno (CNH2), Dr. Jesús Rodríguez Ruiz, and all the new friends I met during my unforgettable stay at the research center.

Infine, un ringraziamento di cuore ai miei genitori, Mercede e Frediano, a mio fratello Luca, a mia nonna Ada, ai miei parenti e a tutti gli amici che mi hanno supportato durante il percorso.

Abstract

This thesis investigates the integration of green hydrogen and ammonia production in renewable energy-powered energy systems, as a decarbonization pathway in the energy sector. Climate change mitigation and the transition to carbon-free energy systems are challenged by the inherent intermittency of renewable sources, which affects grid stability and can lead to energy curtailment. By converting surplus renewable electricity into chemical energy carriers such as hydrogen and ammonia, it is possible to enhance system flexibility, support grid services, and provide carbon-free fuels for hard-to-abate sectors and power generation.

In this research, mathematical modeling is used to develop, optimize and analyze integrated energy systems based on variable renewable energy generation, water electrolysis, energy storage and ammonia production. Two main approaches to system integration are examined: the first combines green hydrogen production with mechanical energy storage (via compressed air energy storage or pumped hydro energy storage) to provide grid balancing and minimize curtailment, while the second analyzes a fully dedicated green ammonia production plant. The performance of each configuration is assessed to identify the optimal system design and operational strategies.

With reference to green hydrogen and mechanical storage integrated solutions, two different configurations are analyzed in detail. In the first configuration, a photovoltaic plant is integrated with a compressed air energy storage system fueled by green hydrogen produced on-site. This approach achieves a round-trip efficiency of approximately 62%, a reduction of photovoltaic curtailment to 4%, while delivering grid flexibility services using carbon-free fuel. On the other hand, the second system integrates hydrogen production in a floating photovoltaic-powered pumped hydro energy storage plant, using surplus energy to maximize self-consumption utilizing 99.2% of renewable energy generation.

Finally, a green ammonia production system is optimized using a mixed integer linear programming approach, allowing for the simultaneous optimization of component size and operation scheduling to minimize production costs. The analysis achieves temporal decoupling of yearly ammonia production from fluctuating photovoltaic input with minimal intermediate storage, with a system efficiency of 45.5% and a levelized cost of ammonia of 995 €/ton.

Table of contents

Nomenclature

Acronyms			
AEM	Anion Exchange Membrane	MILP	Mixed-Integer Linear Programming
ASU	Air Separation Unit	NH3SS	Ammonia Storage System
AWE	Alkaline Water Electrolysis	NOCT	Nominal Operating Cell Temperature
BESS	Battery Energy Storage System	OPEX	Operational Expenditure
CAES	Compressed Air Energy Storage	PEM	Proton Exchange Membrane
CAPEX	Capital Expenditure	PHES	Pumped Hydro Energy Storage
CCUS	Carbon Capture, Utilization, and Storage	PtP	Power-to-Power
CF	Capacity Factor	PtX	Power-to-X
EL	Electrolyzer Unit	PV	Photovoltaic
EMS	Energy Management Strategy	PWA	Piece-Wise Affine
ESS	Energy Storage System	RES	Renewable Energy Source
FPV	Floating Photovoltaic	SC	Self-Consumption
GHG	Greenhouse Gas	SMR	Steam Methane Reforming
GPV	Ground-mounted Photovoltaic	SOC	State of Charge
HB	Haber-Bosch	SOEC	Solid Oxide Electrolysis Cell
HSS	Hydrogen Storage System	SOFC	Solid Oxide Fuel Cell
LCOA	Levelized Cost of Ammonia	STC	Standard Test Conditions
LCOE	Levelized Cost of Electricity	SWRO	Seawater Reverse Osmosis
LCOH	Levelized Cost of Hydrogen	TMY	Typical Meteorological Year
LHV	Lower Heating Value	VRES	Variable Renewable Energy Source

Symbols					
α	Charge transfer coefficient	-	n	Number of units or electrons	-
A	Area	m^2	OF	Objective function value	€
β	Pressure ratio	-	P	Power	W
C	Cost	€	p	Pressure	Pa
δ	Membrane thickness	m	Q	Volumetric flow rate	m^3/s
e	Specific energy	J/kg	R	Universal gas constant	J/(mol·K)
E	Energy	J	ρ	Density	kg/m^3
E^0	Standard reversible cell voltage	V	S	Surface area of a single module	m^2
η	Efficiency	-	σ	Conductivity	S/m
F	Faraday constant	C/mol	T	Temperature	K
f	Derating factor	-	τ	Solar transmittance	-
γ	Specific heat ratio	-	t	Time	s
g	Gravitational acceleration	m/s^2	θ	Temperature correction factor	1/K
GI	Global Solar Irradiance	W/m^2	V	Voltage	V
h	Hydraulic head	m	Vol	Volume	m^3
i	Current density	A/m^2	w	Weighting variable (PWA)	-
λ	Humidification factor	-	W	Water withdrawal	m^3
m	Mass	kg	z	Number of electrons	-
$\dot{m}$	Mass flow rate	kg/s	n	Number of units or electrons	-

Subscripts			
act	Activation	m	Membrane
AEM	Anion Exchange Membrane	max	Maximum
AMB	Ambient conditions	min	Minimum
BESS	Battery Energy Storage System	mod	Module
C	Compressor	nom	Nominal
cell	Cell	ohm	Ohmic
ch	Charge	oper	Operating
cons	Consumed	out	Outlet
CURT	Curtailed	P	Pump
des	Design conditions	PEM	Proton Exchange Membrane
dch	Discharge	PHES	Pumped Hydro Energy Storage
DH	Dark Hours	prod	Produced
diff	Diffusion	PtP	Power-to-Power
EL	Electrolyzer	PV	Photovoltaic system
FPV	Floating Photovoltaic	ref	Reference conditions
G	Grid	rev	Reversible
g	Gas	STC	Standard Test Conditions
gen	Generated	SUR	Surplus
H2	Hydrogen	T	Turbine
in	Inlet	t	Time step
INV	Inverter	tot	Total
lim	Limiting	UP	Upper reservoir
LOW	Lower reservoir		

List of figures

List of tables

Chapter 1

Introduction

1.1 Motivation and objective

The global energy landscape is undergoing a significant transformation, shifting away from fossil fuels towards lower carbon intensity technologies. This transition is driven by the need to mitigate climate change and limit the rise in global temperature below 1.5°C [1]. The urgency of this action is underscored by the significant environmental impact of greenhouse gas (GHG) emissions. Globally, the energy sector is among the largest contributors to these emissions, including electricity, heat, transport, and manufacturing [2]. Carbon dioxide (CO_2) from the combustion of fossil fuels is a major contributor to accelerated global warming, to the increase in extreme weather events, and to the rise in sea levels [3].

Renewable energies such as solar, wind, hydropower, biofuels, and others are at the core of this transformation. Agreements such as the Paris Accord and recent targets like the COP28 commitment to triple renewable energy capacity by 2030 demonstrate the urgency of transitioning from fossil fuel to sustainable energy economies [4], [5]. In 2025, global energy demand grew by 2.2% compared to 2024, driven by a 4.3% increase in electricity consumption, mainly due to increased cooling and industrial demand, electrification of transport, and an increase in data center consumption. For the first time, Renewable Energy Sources (RES) and nuclear power together met 80% of the additional electricity generated worldwide, with the deployment of solar, wind, electric vehicles, and heat pumps [6]. However, despite the steady increase in renewable production, the demand for fossil fuels continues to grow. In 2024, the growth in total primary energy generation is mainly attributed to 38% from renewables and 8% from nuclear, but fossil fuels still constitute 54% of this growth, with 28% from natural gas, 15% from coal, 11% from oil. In 2025, natural gas demand rose by 2.7%, and coal demand increased, particularly in emerging economies. A significant share of this continued dependency on fossil fuels derives from hard-to-abate sectors such as heavy industry, aviation, shipping, and transport, where alternatives to coal, oil, and gas remain limited and costly despite advances in electrification and clean technologies. Nevertheless, renewables increased by 38% reaching 40% of the total global energy production, mostly driven by photovoltaics [6]. The growth of renewable production is, however, insufficient to eliminate the fossil fuel system, due to a surge in global energy demand. Emerging economies account for about 80% of the total demand, primarily driven by China and India, while advanced-economy demand grew by about 1% primarily due to high cooling needs and increased industrial activity [6].

The European Union has set ambitious goals for climate neutrality in the near future, creating a policy framework involving its Member States. Initiatives set binding targets, aiming for net-zero greenhouse gas emissions by 2050 [7]. The strategy for achieving complete decarbonization is contained in the European Green Deal, not only to achieve environmental objectives, but to develop strategies for economic and social growth [8]. The pact aims for a reduction of 55% of net emissions by 2030, 90% by 2040, and net zero emissions by 2050, relative to 1990. Additionally, a core principle states the need to decouple economic prosperity from resource use, without interfering with social and environmental aspects. To establish a solid pathway, the EU introduced the Fit for 55 package, a set of laws to achieve at least 55% net greenhouse gas emissions reduction by 2030. These packages span across different regulatory strategies, aiming at achieving various directives for renewable energy, energy efficiency, and the decarbonization of transport and industry [9]. Specifically, the EU Emissions Trading System (ETS) is a carbon pricing system based on the cap-and-trade principle, in which a cap on total emissions is set on the most GHG-emitting sectors in Europe. To reduce emissions by 62% by 2030, its second iteration (ETS2) includes maritime transport, buildings, and fuels to achieve further GHG emissions reduction. The Carbon Border Adjustment Mechanism (CBAM) applies a carbon tax system to select imports to avoid relocation of carbon emissions to other countries. The Renewable Energy Directive (RED) targets 42.5% of renewable energy consumption by 2030, achieving a 14.5% reduction in GHG intensity in the transport sector, a 29% share of RES in the final consumption, and a 1.6% increase in renewable use in industry. Finally, the Energy Efficiency Directive (EED) introduces a measure to enhance efficiency, setting a target for an 11.7% reduction in energy consumption by 2030.

This transition depends on the accelerated deployment of renewable energy sources, with solar photovoltaic (PV) and wind turbines being primary contributors due to declining costs and widespread availability [10]. These systems are deployable in various scenarios, ranging from small-scale residential applications to large-scale industrial solutions. Their ever-increasing adoption in multiple contexts depends not only on the environmental benefits but also on economic advantages, demonstrating the feasibility of decarbonization pathways for the energy sector. Particularly, the industrial sector is among the largest energy-intensive sectors, mostly reliant on fossil fuels. However, due to stringent environmental legislation, the adoption of renewable energy as a primary source for industrial processes is becoming increasingly important. Hard-to-abate sectors, such as heavy industry and chemicals, still require additional effort as direct RES integration cannot be achieved due to the nature of the processes. For these applications, alternative solutions need to be implemented, including increased efficiency and the adoption of innovative technologies like clean hydrogen, carbon capture, and electrification [11].

Despite the increase in the penetration of renewables in the energy system, these technologies present technical challenges that must be addressed to ensure their safe and reliable operation. First, photovoltaic and wind are inherently intermittent, as their energy

output is directly dependent on the availability of primary sources, weather conditions, and time of day. Often, peak renewable generation does not align with peak energy consumption, resulting in oscillating production and electricity prices. Due to their fluctuating behavior, they are referred to as Variable Renewable Energy Sources (VRES). This limited control over power production generates imbalances between energy supply and demand, posing challenges to the correct management of electricity grids [12]. Increased penetration of VRES in the grid additionally creates problems for frequency and voltage regulation as well as grid inertia. Unlike conventional power plants, which rely on the inertia of rotating machinery to produce electricity at a stable frequency, VRES do not inherently provide such services. Instead, they are connected through power electronics, which decouple them from the grid's natural inertia. While VRES cannot supply inertia on their own, advanced inverter controls and other technologies can enable them to emulate these stabilizing functions. These limitations pose significant challenges in maintaining grid stability and ensuring reliability of electrical power systems and their flexibility, which refers to the capability of a power system to handle fluctuations of supply and demand across various time scales [12], [13]. Additionally, due to production and demand mismatch, another critical challenge arises when renewable production cannot be either fully consumed or stored, and excess production must be curtailed. Renewable energy curtailment occurs when high levels of solar and wind penetration lead to transmission or operational constraints and consequently economic losses, limiting the amount of energy that the system operator can manage [14]. This measure constitutes a loss of renewable energy utilization and a disadvantage for the economic viability of RES investments. Curtailment is becoming ever more frequent in high VRES penetration scenarios, such as the California grid [15].

To correctly manage electricity grids, various measures can be taken to address flexibility challenges [16]. For very short-duration needs, ranging from a few milliseconds to 5 minutes, these measures include services like primary frequency response and frequency regulation, which can be managed using technologies such as flywheels, supercapacitors, and demand-side management via load shifting. Short-duration needs, typically requiring a response within 5 minutes to 1 hour, comprise spinning and non-spinning reserves, contingency reserve, and black start. Conventionally, gas turbines are employed to provide spinning and non-spinning reserve services, but Energy Storage Systems (ESS) such as Pumped Hydro Energy Storage (PHES) plants, Battery Energy Storage Systems (BESS), and Compressed Air Energy Storage (CAES) plants can represent additional alternatives. Intermediate duration services, between 1 hour and 3 days, include load following for demand-supply balancing, load levelling by storing off-peak energy for later use during peak times, unit commitment using ESS to handle scheduling uncertainties, and energy arbitrage, which can increase the profitability of ESS. Long-duration needs, typically on seasonal scales, require energy shifting and seasonal arbitrage, which depend upon large storage capacities.

While direct electrification is the most efficient decarbonization pathway for many applications, it is not a viable solution for all sectors. Hard-to-abate industries like steel

and cement manufacturing, heavy-duty transport, aviation, and maritime shipping require high energy density fuels and chemical feedstocks that cannot be easily replaced by electricity. In these cases, Power-to-X (PtX) systems become possible alternatives. PtX technologies are employed to convert electricity, produced by renewable sources, into chemical carriers. Among those, green hydrogen is at the core of many decarbonization solutions.

Green hydrogen, produced via water electrolysis using renewable electricity to split water into hydrogen and oxygen, is a fundamental element supporting the goals outlined in the European Green Deal. Hydrogen utilization for power generation in Europe is anticipated to increase, requiring 626 TWh of electricity generation from hydrogen by 2050, from the 12 TWh expected in 2030. By 2050, this demand will constitute 7% of Europe's electricity generation, with variations in specific countries like Poland (17%), Ireland and Italy (15%), and Germany (14%). In fact, by 2030, the European Union plans to produce about 10 Mt/year and import about 10 Mt/year of low-emission hydrogen [17], and global hydrogen production is expected to reach 2.3 Gt/year by 2030 [18]. Today, less than 0.2% of electricity generation comes from hydrogen, in contrast to natural gas, which accounts for up to 30%. By 2050, about 88 Mt/year of hydrogen will be required in power generation, nearly equivalent to today's total global annual hydrogen production [19]. Specifically, in Italy, hydrogen is predicted to meet 2% of the total energy demand by 2030, which is equal to 0.7 Mt/year of hydrogen. To achieve this, Italy plans to set up 5 gigawatts (GW) of water electrolyzer capacity. This 5 GW installation is expected to fulfil 50% of Italy's domestic hydrogen demand [20].

As of today, hydrogen is mainly produced using non-renewable fossil fuels. Specifically, hydrogen is produced through steam reforming of natural gas (49%), partial oxidation of hydrocarbons (29%), coal gasification (18%), and water electrolysis (4%). Its consumption comes mainly from the petroleum industry, from ammonia production for fertilizers, from production of methanol and other chemicals, and to a lesser extent from metal processing and fuel cell usage [21], [22].

Hydrogen's low volumetric density poses storage and distribution challenges. It can be stored in gaseous or liquid form, at high pressures of 350-700 bar or liquid at -253°C, to increase its density. Advanced materials and energy expenditures are required to increase its energy density [22]. At small scales, hydrogen can be distributed with tube trailers or cryogenic trucks, while pipelines are used for long-distance transport. While they can support mild hydrogen blending, existing natural gas pipelines require modifications to sustain hydrogen transport, due to steel embrittlement and leaks [23].

While gaseous and liquid hydrogen storage systems can be advantageous in many applications, their shortcomings become relevant for large-distance transport and long-duration storage. Hydrogen can alternatively be converted into other chemical carriers, such as ammonia or various liquid organic hydrogen carriers. Ammonia, in particular, represents a promising hydrogen vector due to its high volumetric hydrogen density, well-

established global infrastructure for production and distribution, and the possibility of reconversion to hydrogen through catalytic cracking. Being liquid at about -33°C or at 10 bar at room temperature, ammonia has a significantly higher energy density compared to gaseous and liquid hydrogen, allowing for more volume-efficient energy storage. Other liquid organic hydrogen carriers are represented by toluene (which can be converted into methylcyclohexane) and dibenzyltoluene. These systems enable hydrogen to be chemically bound and released in certain thermal conditions, allowing its storage and transportation in liquid form at ambient pressure and temperature.

Currently, ammonia is mostly produced with the Haber-Bosch process using hydrogen from steam methane reforming and nitrogen from air separation. The ammonia synthesis requires a high pressure and high temperature environment, at about 200 bar and 400 °C [24], and it consumes approximately 41 GJ/ton (or 1.14 kWh/kg) of energy [25]. This process is a major contributor to global CO_2 emissions, accounting for around 1.3% of emissions from the energy sector and 2% of global final energy consumption [25].

Using RES for ammonia production would allow for a low-carbon alternative in both the chemical sector and the storage and transport of renewable energy. In fact, beyond fertilizers, green ammonia can potentially be employed in mobility as maritime fuel, hydrogen storage, and in electricity generation [26]. The already available ammonia infrastructure for ammonia storage and transport, well established globally, would need minor modifications.

The need for stable operating conditions for the synthesis process, particularly needing consistent temperature, pressure, and feedstocks of hydrogen and nitrogen, creates new challenges when powered directly by VRES. New strategies need to be implemented to address these issues, including integrating battery energy storage systems for balancing energy production and demand, employing hydrogen buffering systems to ensure a stable supply, enhancing process flexibility, and employing alternative electrochemical ammonia synthesis routes.

In this framework, the main objective of this thesis is to develop and analyze innovative plant configurations for the production of green hydrogen and green ammonia, in order to maximize energy efficiency and achieve competitive production costs. The analysis includes the development of plant configurations, the modelling and simulation of the main components and of the fully integrated system, the study of the challenges and constraints, with an outlook on future advancements, using technical and economic indices.

1.2 Thesis overview

The thesis is structured in the following chapters:

- Chapter 1: Introduction to the research scope and motivation.

- Chapter 2: State of the art and general overview on the main technologies and processes involved in the hydrogen and ammonia chain, including production from renewable sources, storage solutions, and research gaps.
- Chapter 3: Description of the system configurations studied, and in-depth analysis of the technologies considered.
- Chapter 4: Discussion of the overall research approach and the methodology of the mathematical modelling framework, encompassing thermodynamic equations, assumptions made, and optimization strategies used.
- Chapter 5: Design and analysis of integrated RES-hydrogen systems for multi-vector production and green ammonia production assessment of levelized cost minimization, through mathematical optimization and techno-economic performance analysis, including addressing the main challenges.
- Chapter 6: Conclusion summarizing the main findings of the thesis and outlook providing insights into potential future research approaches.

Chapter 2

State of the art

2.1 Renewable energy generation

Renewable energy is obtained from self-replenishing natural sources, capable of regenerating faster than they are consumed. These sources include solar, wind, hydraulic, biomass, geothermal, and marine energy. They are characterized by a low or zero carbon footprint during operation. By contrast, fossil fuels such as coal, oil, and natural gas are finite resources which release significant amounts of greenhouse gas emissions, contributing to climate change. For this reason, renewable energies are critical for the transition to a low-carbon future. The energy sector can rely on a variety of technologies to exploit the availability of natural sources, each with its advantages and limitations.

Solar energy harnesses radiation from the Sun as a primary source, converting it to electricity or heat. The Sun provides about 10,000 times the total global energy consumption [27]. The amount of energy that can be extracted depends on the geographical location, the day of the year, and the time of the day, as well as meteorological conditions. Two main technologies allow conversion of solar energy to electricity: PV cells convert sunlight directly into electrical energy through a chemical and physical reaction, while solar thermal energy uses mirrors to concentrate solar radiation and generate heat. This heat is subsequently used to drive a conventional thermodynamic cycle, typically by producing steam to power a turbine and generator. PV technology has experienced rapid cost reductions and widespread deployment due to its modularity and scalability. PV systems can be implemented at various scales, from small residential installations to large utility-scale solar farms, making them a versatile solution for decentralized and centralized power generation. Consequently, modern PV technology is characterized by enhanced performance through advancements in materials, manufacturing, and system integration. The state of the art for high-performance modules is defined by industrial-scale perovskite-silicon modules demonstrating efficiencies of 24.4%, while more advanced micro-concentrator photovoltaic modules are capable of exceeding 36%, and are deployed in systems with power capacities ranging from a few kilowatts for residential applications to several hundred megawatts for utility-scale power plants [28].

Wind energy uses turbines to extract energy from moving air by converting the kinetic energy of the rotor into electric energy with a generator. Wind energy derives directly from solar energy, which causes significant air flows due to the uneven distribution of heat on a global scale. Recent wind turbines, with tall towers and large rotor diameters,

represent a significant evolution of a technology utilized since ancient times for windmills. Depending on the location, they can be divided into onshore and offshore wind farms. The former are located on land, usually close to the end-users, while the latter are installed at sea to benefit from more consistent and constant winds. Like solar technologies, wind energy installations vary significantly in size, from small residential solutions to large industrial farms. Power generation depends on the wind speed, the orography of the plant site, the height and rotor diameter of the turbine, and meteorological conditions. Consequently, modern wind technology is characterized by a significant upscaling in both physical dimensions and power ratings, particularly in the offshore sector. The latest generation of offshore turbines is designed with nominal powers of 15–16 MW, with some manufacturers offering models over 18 MW. These larger models allow for reducing overall generation costs by achieving higher capacity factors [29].

Hydropower is one of the largest sources of renewable energy, converting the geodetical potential energy of water into electrical energy. A hydraulic turbine captures energy from water to drive a generator, coupled with a transmission. Run-of-river hydroelectric plants harness energy directly from the flow of a river, using specifically built infrastructure to collect and redirect water towards a hydroelectric turbine. Their power delivery is strictly dependent on the available water flow rate, which can vary during the year. Reservoir hydroelectric plants exploit the difference in height between two water basins, often artificially formed by dams. Their output depends largely on the difference in height between the reservoirs and the volume of water transferred. Besides electricity generation, they can serve other purposes such as providing water to downstream communities for irrigation, drinking water, and flood control. Their ample flexibility allows them to control the flow of water and supply electricity at certain times of the day. Pumped hydroelectric storage plants build upon the concept of reservoir hydroelectric, by pumping water to the higher reservoir during periods of low electricity cost and releasing it back to generate electricity at times of high demand. Hydropower technology is thus characterized by very high conversion efficiency, which can exceed 90% from water-to-wire, a long operational lifetime, and a vast scalability in terms of power capacity, with installations ranging from a few kilowatts to multiple gigawatts for large-scale reservoir plants [30].

Biomass energy is obtained from organic matter, used as a fuel source. Biomass is a large family of organic matter, including agricultural waste, forest residues, industrial shavings, livestock residues, and municipal solid waste. Even though biomass energy produces CO_2 emissions, the process is considered renewable due to the fact that organic matter can be regrown, absorbing carbon dioxide during its lifespan. Biomass can be either harvested from dedicated crops or derived from residual waste. Biomass energy can be obtained by biochemical conversion, where microorganisms activate chemical conversions to biogas, thermal conversion through pyrolysis or combustion to extract syngas or thermal energy, and various physical and chemical conversions to extract biodiesel or produce solid fuels.

Geothermal energy uses thermal energy contained inside the Earth, beneath the crust. It can be accessed through hot springs, geysers, or in volcanic areas, by extracting hot water or steam. This energy can be used directly as heat for residential and industrial purposes or converted into electricity with dedicated geothermal power plants. Used directly, heat can be provided to residential and industrial areas through hot water or steam. Geothermal power plants instead extract heat from underground reservoirs using wells and employ a thermodynamic cycle to convert heat into electricity. Geothermal heat pumps exploit the temperature difference between the surface air and the ground by using a heat exchanger to provide heat to end-users.

Marine energy harnesses the kinetic and thermal energy of bodies of water to produce electricity. Tidal energy uses ocean tides to produce electricity, while wave energy uses turbines to produce electricity from the movement of ocean waves.

These technologies provide environmental, economic, and social benefits. Reducing greenhouse gas emissions, compared to fossil fuels, is in fact crucial to mitigate climate change and limit global warming. Furthermore, these technologies help to improve air and water quality, resulting in better public health conditions. From an environmental perspective, renewables can create new job opportunities and support local economies, requiring specialized personnel for manufacturing, installation, and maintenance. By reducing the dependence on the import of fossil fuels, countries become more energetically independent and secure, being less exposed to geopolitical tensions. Ultimately, the benefits of renewable energy are interconnected, turning the necessity for more environmentally friendly energy solutions into an opportunity for a vast array of economic and social benefits.

2.1.1 Challenges and limitations

Renewable energy is the key to the energy transition process, particularly in the energy sector, where it can drastically reduce CO_2 emissions. Despite its significant advantages, renewable energy still faces inherent challenges and limitations that slow its adoption and require innovative solutions. Many renewable technologies rely on weather-dependent sources, especially on sun and wind availability, leading to intermittent generation. Consequently, unlike conventional power plants, which can adjust production based on demand, the supply-side control is very limited for the most common renewable energy plants, like solar and wind. The mismatch between supply and demand, both in terms of time and power, creates significant challenges to grid management and stability. At times of low primary source availability, energy production may be lower than demand and potentially require other sources of energy to compensate. When production exceeds demand, renewable energy may be curtailed or wasted, ultimately leading to economic disadvantages. Forecasting weather patterns and future demand is crucial for the correct balancing of the grid.

The existing energy infrastructure, built for conventional power systems, is often not capable of operating with variable and distributed renewable sources. Due to their age,

these grids are not equipped to manage the dynamic behavior of large amounts of variable power. Moreover, renewable plants are often located in remote centers, necessitating new transmission lines to connect with the grid. To achieve an even distribution of renewables over large territories or countries, new infrastructure is required for long-distance transmission. Furthermore, this issue comes from the original design philosophy of the grid. The traditional electrical infrastructure worked on a model of large-scale centralized generation from which power was distributed in a unidirectional flow to passive consumers. Distributed energy resources, particularly residential and commercial PV systems, change these passive consumers into 'prosumers' who both consume from the grid and supply power into the grid. This necessitates the management of bidirectional power flows for which the infrastructure was not designed, introducing significant technical challenges such as voltage fluctuations, reverse power flow, and increased complexity in grid protection and control.

Large installations may also affect the surroundings, requiring significant land areas and sometimes interfering with wildlife, which may restrict project implementations due to social and political issues. Clear regulatory frameworks are therefore crucial to achieve a widespread implementation of renewables, involving stable policies and market strategies.

The intermittency of power generation requires efficient systems to store excess production and reduce the mismatch between supply and demand. Energy storage systems allow for effective storage of surplus energy generated during peak production times, to be later provided during periods of low generation. Battery energy storage systems are currently used widely in small to large-scale applications, but other energy storage systems are required for an effective integration of renewables in the energy sector.

2.2 Energy storage

ESS has emerged as one of the most promising solutions for supply-demand mismatch, allowing for storing, holding, and later releasing energy when needed. ESS enhances grid performance by increasing the stability and flexibility of renewable energy systems, aiding in the energy transition.

Earliest energy storage systems trace back to the 19th century, to lead-acid batteries, and later in the development of pumped hydro storage [31]. Modern energy storage technologies operate on various thermodynamic and electrochemical principles and can be categorized based on the form in which energy is stored as: thermal, mechanical, chemical, electrochemical, electrical, and hybrid systems. This chapter presents a comprehensive analysis of the state of the art of energy storage technologies, summarized in Figure 1. The performance of each system is evaluated in terms of its technical and operational characteristics, including power and energy density, round-trip efficiency, response time, lifetime, and technological maturity.

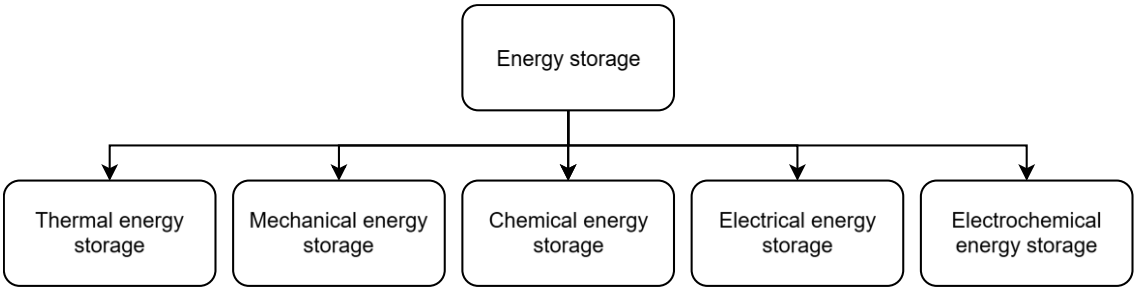

Figure 1. Energy storage technologies.

Thermal energy storage (TES) systems store energy in the form of heat. Based on the operating temperature levels, they can be divided into Low-Temperature Energy Storage (L-TES), Medium (M-TES), and High-Temperature Energy Storage (H-TES) systems. Based on the operating principle, they can be divided into Sensible Heat Storage (SHS) systems, Latent Heat Storage (LHS), and thermochemical storage systems.

- SHS systems store energy by increasing the temperature of a solid or liquid material without changing its phase. During discharge, heat is recovered by cooling the system. Liquid SHS typically employs water or organic liquids to store energy at low temperatures and is combined with solid materials like concrete to increase its temperature range. Alternatively, molten salts offer an alternative for temperatures above 100°C, and for this reason, they are often used in concentrated solar plants. Solid SHS include borehole and packed-bed TES systems. Borehole TES systems transfer heat underground using boreholes, in which a heat transfer fluid conducts heat through heat exchange pipes. Packed-bed TES is composed of an external tank filled with rock materials, which can store large amounts of energy by increasing their temperature. Operating cyclically, hot air or a heat transfer fluid flows through the packed bed material, exchanging heat directly by convection.
- LHS systems use phase change materials to store energy in the form of latent heat. When heat is added or removed from the material, it undergoes a phase change, causing the material to transform from solid to liquid form or vice versa. Phase Change Materials (PCM), which can be either of organic or inorganic nature, can store 5 to 15 times more energy than conventional sensible energy storage materials and can supply energy at nearly constant temperature.
- Thermochemical energy storage systems utilize reversible chemical reactions to store and release thermal energy. During the charging phase, heat breaks down a chemical compound into its products. These products can then be stored separately at ambient temperature with limited thermal losses, making the technology particularly suitable for long-duration or seasonal storage applications. When heat is required, the products are recombined, releasing the stored chemical energy as heat. This technology has the highest energy storage density among all TES technologies. However, the technology currently faces challenges related to slow reaction kinetics and material degradation.

Mechanical energy storage systems convert electrical energy into potential or kinetic energy. Electrical energy is used to drive a mechanical system, which stores energy in the form of kinetic or potential energy. These systems can be implemented at various scales and can provide numerous services to the grid, enabling more effective renewable energy utilization.

- PHES uses electrical energy to drive a pumping system that elevates water from a lower to an upper reservoir, converting electricity into potential energy. During discharge, when energy is required, the system generates electricity from the flow of water from the upper to the lower reservoir via a hydroelectric turbine. These systems constitute about 90% of the global installed storage capacity. PHES systems are characterized by large power capacity (from 100 MW to about 5,000 MW), long storage duration (about 4 to 20 hours), and extended operational lifetime (from 30 to 60 years). However, their deployment is constrained by specific geographical requirements and can result in significant environmental impacts.
- CAES systems store energy as compressed air in a dedicated reservoir, either above ground or underground. During the charge phase, an electric motor drives a compressor train to increase the pressure of ambient air, which is stored in a dedicated high-pressure tank or an underground cavern. Later, during the discharge phase, compressed air is expanded through a turbine, driving a generator to produce electrical energy. During compression, air undergoes both pressure and temperature increase, while the opposite occurs during expansion. CAES technologies where heat of compression is not recovered are classified as Diabatic-CAES (D-CAES), and additional energy is required to increase the air temperature before expansion. Adiabatic-CAES (A-CAES) systems employ a dedicated TES to store and later release the heat recovered during compression. Isothermal-CAES (I-CAES) uses specific machinery to increase pressure at near constant temperature, minimizing losses. Liquid air CAES (LAES) systems use dedicated heat exchangers to store air in a liquid state inside a cryogenic reservoir. Although CAES can store large amounts of energy, the low energy density of air requires vast storage facilities. Underground air storage in salt caverns or abandoned coal mines can offer a potential solution but limits the versatility of these systems to only favorable geographical locations.
- Gravity energy storage systems store potential energy by increasing the height of a mass, later released to generate electricity with a generator. Long shafts can be constructed underground using water to push a heavy mass to higher altitudes during the charge phase. During discharge, when the flow is inverted due to the mass pushing on water, electricity is produced with a hydraulic turbine.
- Flywheels are used to store kinetic energy in a rotating cylinder. The system is composed of a flywheel, located inside a vacuum chamber, connected to an electrical motor/generator with magnetic bearings. Increasing its rotational speed allows it to store more kinetic energy, later converted into electricity with the generator during the deceleration phase. High-speed flywheels can reach rotational speeds up to 10^5 rpm. These systems are characterized by very fast

response times (in the order of milliseconds) and high round-trip efficiency (up to 95%). Due to their high self-discharge rates, they can be used preferably for short-term storage and frequency regulation services.

Electrochemical storage systems, or batteries, store energy in the chemical bonds of their constituent materials and convert it back to electricity through reversible electrochemical reactions.

- Lithium-ion (Li-ion) batteries are currently the dominant electrochemical storage technology, thanks to their high energy density, high round-trip efficiency of about 90%, and long cycle life. Various cell chemistries are available, with different energy density, power density, cost, safety, and lifespan. These systems are highly modular, allowing for applications ranging from small-scale residential systems to large, grid-scale installations for frequency regulation and peak shaving.

- Lead-acid batteries are a mature and low-cost technology; lead-acid batteries are widely used for off-grid applications. Their performance is characterized by lower energy density, shorter cycle life, and lower depth of discharge compared to Li-ion batteries. A significant drawback is the environmental impact due to the use of lead.

- Flow batteries, such as the Vanadium Redox Flow Battery (VRB), allow for the decoupling of energy capacity and power rating. Energy is stored in external tanks of liquid electrolytes, while the power conversion occurs in a separate electrochemical stack. This configuration allows for highly scalable, long-duration storage (up to more than 10 hours), with a long lifetime and without degradation from deep cycling. However, they currently exhibit lower energy density and round-trip efficiency compared to Li-ion batteries.

Chemical Energy Storage (CES) systems convert electrical energy into a stable chemical carrier, which can be stored for a long duration and used later. These chemicals can be converted via combustion into mechanical energy and, with a generator, into electricity. Chemical energy storage includes a variety of substances. Among these, hydrogen derivatives such as ammonia and methanol, often referred to as e-fuels, are receiving significant attention. CES can present a high volumetric energy density, making them suitable for transport and as fuels in hard-to-abate sectors such as industry, aviation, and shipping. However, a significant challenge for CES is its lower round-trip efficiency (the ratio of the net energy recovered during discharge to the total electrical energy supplied during charging) compared to other storage methods, due to the energy losses incurred during the conversion steps. In particular:

- Hydrogen can be generated from water, usually by electrolysis or by photocatalytic water splitting using solar energy. When produced using surplus electricity, hydrogen serves as an energy storage medium because it is compressed at high pressure, stored, and later reconverted into electricity via a fuel cell system.

However, the round-trip efficiency of this cycle remains lower than that of most alternative storage technologies.

- Synthetic natural gas requires hydrogen produced from water electrolysis, which is subsequently reacted with a source of carbon dioxide, captured from CCUS, in the methanation process. The resulting product is primarily methane, produced with renewable energy.
- Methanol is synthesized by the reaction of green hydrogen with a carbon source over a catalyst. Methanol can be stored in a liquid state at ambient temperature and pressure, making it advantageous compared to gaseous hydrogen or synthetic natural gas.

Electrical Energy Storage (EES) systems store energy directly in an electric or magnetic field. This allows for extremely high power densities and nearly instantaneous response times. The primary limitation of these systems is their low energy density, which constrains their application to short-duration applications and grid stability services. More in detail:

- Capacitors store energy in the electrostatic field generated between two conductive plates separated by a dielectric material. They are commonly used in many electrical applications, but due to their low energy density, they can't support high currents for extended periods of time.

- Supercapacitors represent a significant advancement on the principle of capacitors. They comprise two electrodes with a large surface area immersed in an electrolyte and separated by a porous membrane. Energy is stored electrostatically through the formation of an electric double-layer at the interface between the electrodes and the electrolyte. This configuration allows for a much larger surface area and a smaller separation distance between charges compared to conventional capacitors, resulting in significantly higher energy storage capacity. Supercapacitors are characterized by an extremely high power density, a nearly instantaneous response time, a very high round-trip efficiency (up to 98%), and a long lifetime. However, they are used for high-power and short-duration applications due to the low specific energy density.

- Superconducting Magnetic Energy Storage (SMES) systems store electrical energy directly within a magnetic field generated by the flow of a direct current through a cryogenically cooled superconducting coil. A SMES installation is comprised of three principal subsystems: a superconducting coil, a power conditioning system connected to the grid, and a cryogenic refrigeration system to maintain the coil at temperatures near absolute zero. During the charge phase, the power conditioning system increases the current intensity in the coil. During discharge, the stored energy is released back to the grid as the current in the coil decreases. SMES technology is characterized by very high round-trip efficiencies due to its extremely small losses. It also presents very short response time.

2.3 Hydrogen as an energy carrier

Hydrogen is increasingly recognized as a versatile energy carrier. Its role is fundamentally linked to mitigating the challenges posed by the high penetration of VRES and can be employed as an energy storage solution. This is highlighted by the current and projected scale of use. Global hydrogen demand in 2023 was approximately 97 Mt, with the vast majority produced from fossil fuels, and used primarily in industrial refining and chemical synthesis. Future demand is projected to increase significantly, although exact future consumption is strongly dependent on policy implementation. In the IEA Announced Pledges Scenario (APS), which assumes all targets are met on time, demand could reach about 150 Mt by 2030. A more ambitious trajectory is defined by the Net Zero Emissions by 2050 (NZE) Scenario, where a rapid increase in low-emission hydrogen production should reach 35 Mt by 2030 [17].

Hydrogen is characterized by high energy density, with a Lower Heating Value (LHV) of 120 MJ/kg. Conversely, its energy density is very low, being only 5600 MJ/m^3 for 700 bar compressed gas and 8000 MJ/m^3 for liquid hydrogen. For this reason, storing large amounts of hydrogen energy requires substantial volumes, leading to size constraints for storage tanks, especially in mobile applications.

Due to its low volumetric energy density, hydrogen must be stored either under high pressure or in liquid form. In its gaseous state, it is typically compressed to pressures of up to 700 bar, which demands robust pressure vessels. To withstand these mechanical stresses while keeping weight low, specialized tanks are usually built from advanced composite materials such as carbon-fiber reinforced polymers.

Alternatively, hydrogen can be liquefied at cryogenic temperatures around 20 K, but this process is highly energy-intensive and requires insulated tanks, increasing cost and complexity to storage and transport. Moreover, heat transfer from the environment causes boil-off losses, due to the continuous evaporation of a portion of liquid hydrogen, thus requiring a constant cooling. When transported in metallic pipelines or stored in metal vessels, another challenge is hydrogen embrittlement, which degrades the mechanical integrity of the material and can lead to leakage.

When transported using metals, a critical issue is the embrittlement of the material, which leads to mechanical degradation and leakage. This phenomenon affects both pipeline transport and vessel storage.

1.1 Types of hydrogen

To differentiate between the various hydrogen production pathways and their environmental impacts, a color classification system has emerged as the hydrogen color spectrum. This system provides a categorizing method based on hydrogen feedstock, the primary energy source utilized, and its associated carbon intensity [32], [33].

Grey hydrogen is produced from fossil fuels, mainly through Steam Methane Reforming (SMR) of natural gas and gasification of coal. It is currently the main method used for commercial-scale hydrogen production. These technologies, being the most mature, are the most economical methods. Its high carbon footprint, however, is a significant disadvantage. In particular, SMR generates approximately 7.5-13 $kgCO_2eq/kgH_2$ [33].

Black and brown hydrogen is produced using bituminous or lignite coal for gasification. These are the most environmentally damaging forms of hydrogen, with a carbon intensity of 18-25 $kgCO_2eq/kgH_2$. This method is still highly used as coal reserves are the largest worldwide. China produces vast amounts of black and brown hydrogen at low cost, due to its large reserves.

Blue hydrogen is derived from conventional fossil-fuel technologies, but CO_2 is captured and stored with the integration of Carbon Capture, Utilization, and Storage (CCUS) technologies. Its effectiveness in reducing greenhouse gas emissions is related to the CO_2 capture rate. It is considered a low-carbon solution, which could provide a potential pathway to mitigate the emissions of conventional technologies in the short term. However, methane leakage throughout the natural gas supply chain constitutes a significant limitation to its effectiveness. Depending on the CCUS technology, blue hydrogen can have carbon intensities from 0.8 to 5.8 $kgCO_2eq/kgH_2$.

Turquoise hydrogen is produced through methane pyrolysis, by thermally cracking methane into gaseous hydrogen and solid carbon, avoiding gaseous CO_2 emissions. The solid carbon byproduct can be employed in various other industrial processes. Nevertheless, leakage of methane from the feedstock persists, resulting in CO_2 emissions of about 1.9-4.8 $kgCO_2eq/kgH_2$.

Green hydrogen is produced through water electrolysis by employing only renewable sources such as solar, wind, or hydropower. This avoids carbon emissions during both the electricity production and the hydrogen production processes. Green hydrogen is therefore considered a zero-carbon approach to hydrogen production. However, emissions associated with plant construction and end of life must be considered. When taking into account the whole supply chain, green hydrogen's impact is estimated at 0.7 to 2.8 $kgCO_2eq/kgH_2$.

Pink hydrogen is produced through water electrolysis using electricity generated with nuclear power. When the process includes heat from thermochemical water splitting, purple hydrogen is produced. Red hydrogen is instead generated with high-temperature catalytic splitting of water, powered by nuclear energy. Due to the carbon-neutral lifecycle of nuclear energy, pink hydrogen is considered low-carbon. The carbon emissions for these technologies vary from 0.1 $kgCO_2eq/kgH_2$ for red hydrogen to a maximum of 0.6 $kgCO_2eq/kgH_2$ for pink hydrogen.

Yellow hydrogen involves powering water electrolysis with energy from the electrical grid. Its environmental impact is dependent on the share of renewable and low-emitting

energy sources in the grid. If the electricity grid relies heavily on fossil fuels, yellow hydrogen presents significant carbon emissions.

White hydrogen is naturally formed and extracted from underground reservoirs. When derived from fermenting processes induced by microbes, it is called gold hydrogen. Due to limited research in the field, its carbon footprint needs further analysis.

Table 1 summarizes hydrogen production methods, including CO_2 emissions and costs [32], [33], [34].

Table 1. Carbon emissions and costs for the hydrogen colors.

	CO_2 emissions ($kgCO_2eq/kgH_2$)	Cost ($/kg)
Grey	7.5-16	0.7-2.3
Black and brown	18-25	1.2-2.5
Blue	0.8-5.8	1-3.2
Turquoise	1.9-4.8	1.6-3.4
Green	0	1.9-8.2
Pink	0	2.2-7
Yellow	Power mix dependent	4.83-13.11 (Europe)
White	Unknown	Unknown

2.3.1 Hydrogen production and usage

At present, global hydrogen demand is predominantly led by the refining and chemical industries. In refineries, hydrogen is utilized for removing impurities and upgrading heavy oil fractions into more valuable products. In the chemical industry, hydrogen is a key feedstock to produce ammonia, primarily used for fertilizers, methanol, and other chemical substances. Global hydrogen consumption depends by 47% on petroleum refining, 45% ammonia production, 4% methanol production, 2% metals production, and 2% on other uses.

Currently, almost the totality of global hydrogen production is fossil-fuel based. Steam reforming of natural gas is largely the main production technology, constituting 49% of global hydrogen production, followed by 29% from partial oxidation of hydrocarbons, 18% from coal gasification, and 4% electrolysis. These technologies are responsible for substantial CO_2 emissions. A potential short-term solution for the energy transition is the replacement of fossil fuel-based hydrogen with low-emission hydrogen in these existing applications. It primarily involves using renewables to substitute fossil fuels as primary energy sources or adopting carbon capture technologies in already established production facilities.

Figure 2 shows the main methods for the production and consumption of hydrogen.

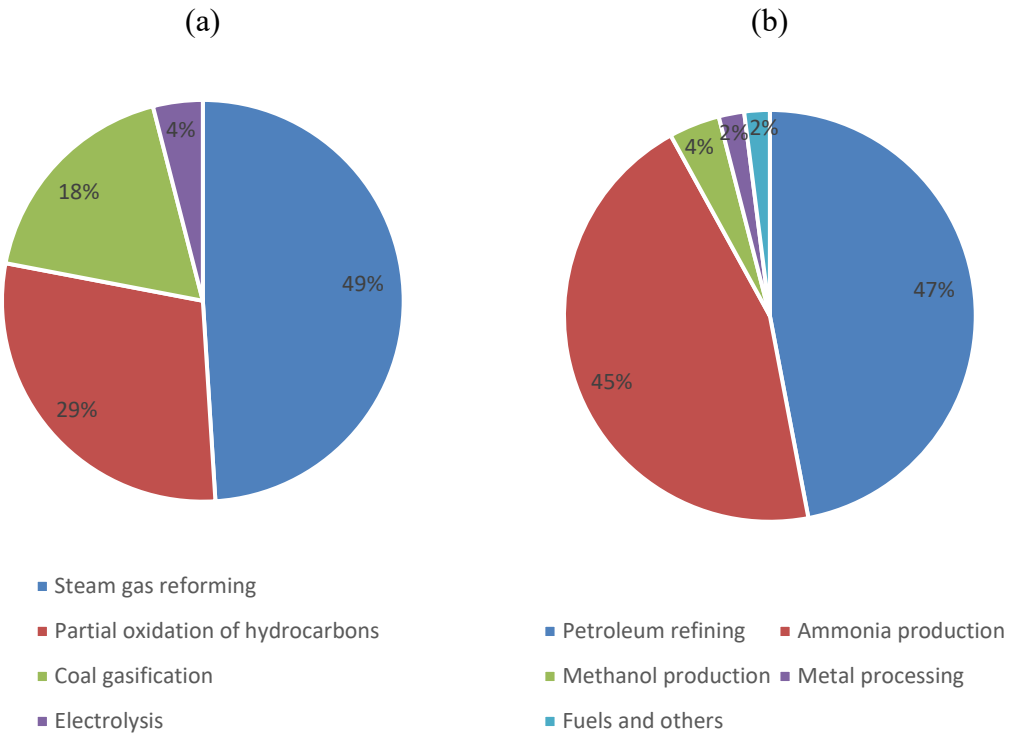

Figure 2. Hydrogen production technologies (a) and hydrogen demand sectors (b).

Beyond its traditional applications, low-emission hydrogen can serve multiple purposes to aid in decarbonizing hard-to-abate sectors: in steel production, green hydrogen can replace coal for the steel production process; in automotive mobility, fuel cell vehicles use hydrogen to power electric motors, with lower refueling times compared to battery electric vehicles; in aviation and maritime transport they can be employed to power large engines; in trains hydrogen can be employed in fuel cells to substitute diesel-powered engines.

2.3.2 Hydrogen storage

Hydrogen is characterized by the highest gravimetric energy density of any fuel, but its low density at standard temperature and pressure limits its volumetric energy capacity. Hydrogen can be stored in physical-based or material-based systems.

Physical-based systems include compressed gas and liquid hydrogen. Gaseous hydrogen is generally contained in vessels that can withstand very high pressures, typically in the range of 350–700 bar. Since the hydrogen molecule is extremely small, it tends to diffuse through materials. Therefore, storage tanks must be designed to minimize leakages and sustain high pressure levels, using materials with a high tensile strength, such as austenitic stainless steel [35].

Underground hydrogen storage is a potential solution for long-term, large-scale storage by exploiting geological formations such as aquifers, depleted reservoirs, porous rocks, and salt caverns. Conceptually, it is similar to natural gas storage, which is already demonstrated, but faces new challenges due to hydrogen's low density, viscosity, and molecular size. For these reasons, it requires higher flow rates and larger wellbores to

mitigate leakages due to diffusion. Its commercial use depends on technical and economic factors, as well as regulatory limitations [36].

In contrast, maintaining hydrogen in liquid form necessitates cryogenic conditions, since at standard atmospheric pressure its normal boiling point is −252.8 °C. Even in well-insulated systems, heat is transferred due to the large difference in temperature between liquid hydrogen and the external environment. For this reason, liquid hydrogen storage is subject to continuous boil-off losses, depending on the size, shape, and thermal insulation of the tank. Since the boil-off rate is a function of the surface-to-volume ratio, this phenomenon is reduced for large storage tanks [35]. Therefore, liquid hydrogen storage requires large energy expenditures both for liquefaction and for limiting the boil-off. For this reason, liquid hydrogen can be primarily employed in air and space applications, where the cost is not a critical problem and the gas is consumed in a short time [35].

Metal hydrides constitute a promising material-based hydrogen storage technology, offering safety and efficiency benefits compared to conventional compressed or liquefied hydrogen. Metal hydrides are formed through the reversible reaction of hydrogen with specific metals or alloys, and they enable storage at moderate pressures and temperatures while achieving high volumetric hydrogen densities. In these systems, hydrogen atoms occupy interstitial sites within the metal lattice, and storage performance is strongly influenced by factors such as lattice structure, particle morphology, surface chemistry, and material purity. These characteristics make metal hydrides attractive for mobile and stationary applications, as they reduce risks associated with high-pressure gas tanks and cryogenic liquid tanks. However, current challenges include slow hydrogen absorption/desorption kinetics, limited gravimetric storage capacity due to the high mass of host metals, degradation over repeated cycles, and the need for precise thermal management during hydrogen release. Consequently, while metal hydrides demonstrate clear potential, further advances in alloy design, nanostructuring, and thermodynamic behavior are required for large-scale commercialization [37].

2.3.3 Hydrogen challenges and limitations

A critical challenge for the widespread use of green hydrogen is the current production cost, which is estimated at approximately 2.5-5 $/kg, depending on factors such as renewable energy prices and electrolyzer investment costs. Its cost is predicted to fall below 2 $/kg by 2030 and potentially reduce to under 1 $/kg by 2050 in optimal scenarios [38]. Achieving this target requires a substantial reduction in the capital cost of electrolyzer units and of the entire production cycle. Additionally, there is a need to improve the conversion efficiency from electricity to hydrogen and then back to electricity.

The Levelized Cost of Hydrogen (LCOH) is predominantly influenced by two key factors: the capital expenditure (CAPEX) of the electrolysis system and the cost of renewable electricity. The CAPEX, which includes the cost of the electrolyzer stack and the balance-of-plant (BoP) components, is expected to decline significantly due to

economies of scale, technological innovation, and supply chain development. In terms of operating expenditure (OPEX), the cost of renewable electricity typically represents the largest share of the LCOH, often accounting for 50–70% of the total. In addition, the availability and temporal profile of renewable energy are critical determinants of production cost. Specifically, the capacity factor, defined as the ratio of actual operating hours to the maximum possible hours, directly affects electrolyzer utilization. A low capacity factor, often caused by the intermittency of renewable power supply, increases the specific cost of hydrogen, underscoring the importance of strategies that maximize operating hours and improve overall cost competitiveness.

2.3.4 Water for hydrogen production

Electrolysis involves water splitting into hydrogen and oxygen. One of the most discussed challenges of electrolysis is water consumption. The water consumption rate for hydrogen production is about 9 kgH_2O/kgH_2, or 0.27 t/MWh, considering its LHV. When considering fossil-fuel-based hydrogen production, the water consumption can increase further, reaching 4.1 t/MWh for pink hydrogen produced with nuclear energy and coal gasification. This significant increase in pink hydrogen is not attributed to the electrolysis process itself, but rather to the substantial cooling water requirements of the nuclear power plant generating electricity. Similarly, conventional grey hydrogen production via SMR also exhibits significant water consumption, used both as a feedstock in the reforming reaction and for process cooling.

Therefore, while electrolysis-based green hydrogen production has a lower direct water footprint compared to thermochemical routes that require extensive cooling, the overall impact depends heavily on the source of electricity and the local context. The geographical location of optimal RES, often in arid coastal regions with high solar irradiance or strong winds, makes freshwater availability a critical constraint. Consequently, large-scale green hydrogen facilities might rely heavily on seawater desalination to meet their water demand. This introduces an additional energy cost to the overall process, increasing both the cost of hydrogen and the total electricity demand. Furthermore, the management and disposal of the byproducts produced during desalination present a significant challenge that must be addressed to ensure the sustainability of the entire production chain.

2.4 Ammonia as an energy carrier

Green ammonia is increasingly considered a viable alternative to green hydrogen because it offers substantially higher volumetric energy density, easier liquefaction at moderate cryogenic conditions (−33 °C at atmospheric pressure), and more practical storage and transport compared to compressed or liquid hydrogen. Green ammonia is produced using renewable energy to power the process and using green hydrogen and nitrogen from the air. The current ammonia infrastructure facilitates the adoption of green ammonia in many sectors, substituting conventional fossil-fuel-based production and therefore aiding in reducing greenhouse gas emissions.

Ammonia can be stored and transported as a liquid at about -33°C or about 10 bar at ambient temperature. It presents a high volumetric hydrogen density of 121 kgH_2/m^3, about 1.7 times higher than liquid hydrogen (70.9 kgH_2/m^3). Its energy density is equal to 3.83 MWh/m^3 compared to 2.64 MWh/m^3 for liquid hydrogen. Consequently, ammonia can store more energy in a given amount of volume and in much less demanding conditions. Additionally, it is characterized by a low boil-off rate of about 0.025 %/day, compared to about 0.52 %/day for hydrogen. For these reasons, ammonia is a promising candidate for long-duration and long-distance transport, minimizing energy losses over time.

Ammonia is currently traded globally, transported via marine vessels, and with a mature infrastructure that is not currently available for other alternative low-emission fuels. This network for production, storage, and transport can be exploited, significantly accelerating its adoption as an energy carrier. The infrastructure includes refrigerated tanks, pipelines, road transport tanks, and ships. For these reasons, ammonia can be a near-term solution for the energy transition in many sectors such as chemical production, agriculture, and marine transport. In 2020, global ammonia production was approximately 185 Mt. This consumption is dominated by agricultural applications, with approximately 70% of all ammonia used for fertilizers. The production of urea is the largest driver, accounting for around 55% of total ammonia demand, with approximately 75% of urea used as a fertilizer. Only about 2% is used for the direct application of ammonia to pastures. The remainder, about 30%, is used in industrial applications such as the manufacturing of plastics, explosives, and synthetic fibers, or as a chemical agent in the form of urea to reduce nitrogen oxide (NOx) emissions from power plants and diesel engines [39].

Several potential trajectories for ammonia consumption are estimated up to 2050. In the Stated Policies Scenario of the IEA, total ammonia production for conventional uses is expected to grow by 37%, reaching 253 Mt by 2050. In the Sustainable Development Scenario and the Net Zero Emissions by 2050 Scenario, demand for ammonia should lower to 230 Mt, due to the projected increase in fertilizer efficiency use. These scenarios also highlight the use of ammonia as an energy carrier. An additional 125 Mt of ammonia is expected to be used as maritime fuel and for power generation by 2050. Therefore, the total consumption is expected to increase to 355 Mt. The most ambitious scenario projects a total consumption of 568 Mt of ammonia by 2050, considering power generation and transport [39].

Conventional ammonia production relies mainly on fossil fuels, primarily methane via steam methane reforming or coal gasification, to produce hydrogen. This reliance on fossil fuels makes ammonia a significant contributor to global greenhouse gas emissions, accounting for approximately 1.8% of annual carbon dioxide emissions. It is, therefore, crucial to develop pathways to decarbonize the ammonia industry. As a first step, green ammonia can be utilized to substitute conventional ammonia, reducing its carbon footprint. Second, it can be used as an energy carrier in other hard-to-abate sectors.

Currently, green ammonia research is focused on developing small, distributed production facilities, particularly in locations with agricultural needs. In fact, the vast majority of ammonia is used for agricultural fertilizer production.

However, this approach introduces significant operational challenges, primarily related to the intermittent nature of renewable energy sources. The conventional Haber-Bosch process, which is the dominant technology for ammonia synthesis, operates most efficiently under steady-state conditions at high pressures and temperatures. Integrating this process with fluctuating power from solar or wind energy requires innovative process control strategies, energy storage solutions such as BESS or hydrogen storage, and flexible operation to maintain high efficiency.

To overcome the limitations of the Haber-Bosch process at small scales, alternative synthesis technologies are also being investigated. These include electrochemical synthesis, producing ammonia from water and nitrogen at ambient conditions, potentially offering a more direct and flexible integration with RES. While promising, these technologies currently face challenges related to low Faradaic efficiency, catalyst stability, and low production rates, and are therefore at a lower Technology Readiness Level (TRL).

Table 2 summarizes the key performance metrics for the most promising energy carriers. Pure hydrogen presents a high LHV, but a very low volumetric energy density. Even in the liquid state, its energy density is still lower compared to other fuels. Ammonia can be stored in milder conditions, but it shows low hydrogen content and low LHV. Liquid methane has the highest volumetric density but needs more demanding storage conditions.

Table 2. Electrochemical properties of the main energy carriers [26], [40], [41].

	LHV (MJ/kg)	Volumetric energy density (MJ/m^3)	Hydrogen (wt%)	Storage conditions
Ammonia	18.6	12.679	17.6	-33°C / 1 bar
Liquid hydrogen	120.1	8.502	100	-253°C / 2 bar
Gaseous hydrogen	120.1	4.823	100	25°C / 700 bar
Liquid methane	48.6	20.527	25.1	-162°C / 1 bar
Methanol	19.9	15.741	12.6	25°C / 1 bar

2.5 Research gaps and thesis contribution

The review presented in this chapter highlights the significant advancements in individual renewable energy, energy storage, and chemical conversion technologies. The transition towards a decarbonized energy sector depends on the deployment of these systems. However, this analysis also shows that several research gaps currently limit the optimal design and integration of such energy systems.

While the existing literature offers extensive insights into the performance of individual components, further analysis is required at the integrated system level. In particular, the

integration of hydrogen production and use in efficient energy systems must be analyzed to identify plant configurations that can synergically exploit surplus VRES production to reduce green hydrogen technical and economic drawbacks. Additionally, the operational mismatch between the variability of VRES generation and the steady-state demands of processes like the Haber-Bosch loop requires further investigation. Some existing works consider simplified approaches for the challenges of optimizing buffer technologies. Moreover, the assumption that surplus electricity can be consistently sold to the grid is increasingly less applicable. Therefore, comprehensive system studies are required to assess how integrated configurations can improve economic performance by utilizing otherwise curtailed energy.

To address these identified gaps, a mathematical framework is designed in this thesis to analyze and optimize the design and operation of integrated green hydrogen and green ammonia production systems. These models are applied to conduct a techno-economic analysis under realistic grid constraints, including VRES curtailment, to evaluate the role of these systems in providing grid flexibility. The thesis further contributes by providing an assessment of different multi-vector energy systems, including the integration of hydrogen with mechanical storage and its use in dedicated green ammonia production. Additionally, the work also investigates critical resource consumption by evaluating the water footprint of large-scale electrolysis and the viability of seawater as an alternative to freshwater sources.

Chapter 3

System configuration and processes

3.1 General framework for integrated energy systems

In this thesis, energy systems are developed and analyzed to address the challenges of VRES production, especially from PV plants. In these integrated systems, hydrogen is employed not only as an energy vector for storing and recovering energy, but also as a chemical feedstock for downstream processes. The configurations investigated in this thesis leverage green hydrogen to achieve these objectives. While each configuration addresses specific applications, they all originate from the framework illustrated in the general diagram in Figure 3.

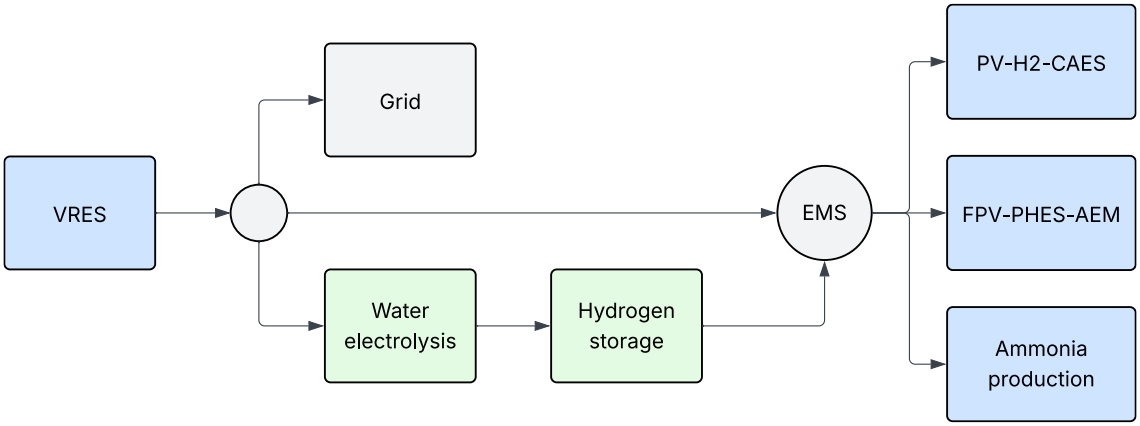

Figure 3. General system integration framework

In all configurations, the primary energy that powers the processes is directly provided by the VRES plant. An Energy Management Strategy (EMS) is applied, in each configuration, to divide the energy flow into its main components: the energy system itself, the water electrolysis process, and the grid for managing surplus production.

Following the general scheme, three configurations are studied:

- PV-H2-CAES configuration: in the first configuration, hydrogen is used as a carbon-free fuel in a diabatic CAES system. In this layout, renewable energy is used to power both the CAES system and a PEM electrolyzer, such that hydrogen is produced, stored, and used on-site.
- FPV-PHES-AEM configuration: the second configuration analyzes the integration of hydrogen production via an AEM electrolyzer into an existing PHES facility, where all the primary energy is provided by a Floating Photovoltaic (FPV) plant.

- Ammonia production configuration: the third configuration examines a fully dedicated green ammonia production plant. In this system, hydrogen serves as a primary feedstock for the Haber-Bosch synthesis loop.

3.1.1 Integrated CAES configuration

Among the energy storage technologies characterized by medium-high storage capacities, CAES systems are one of the most interesting options, potentially more cost-effective compared to batteries and somewhat comparable to pumped hydro systems [42]. Thanks to their suitability in providing flexibility services, CAES are TMES systems have recently regained attention, despite the fact that their technology is not novel: in fact, the McIntosh [43] and Huntorf [44] plants have been operational for over 30 years. Like A-CAES systems, the hydrogen-powered D-CAES concept avoids the use of fossil fuels but overcomes the flexibility limitations through the introduction of electrolyzers, whose operational range is much broader. The Net Zero 2050 scenario, in which the electricity output from unabated methane is foreseen to virtually disappear [1], requires that the hydrogen used by these H_2-powered D-CAES systems comes from RES. In the configuration analyzed in this thesis, a diabatic CAES plant is fueled with green hydrogen, produced directly on site, powered by a PV plant. The CAES system considered originates from the McIntosh plant, which consists of a compression train with four compressors, an air storage unit, a turboexpander train with two turbines, two combustion chambers, and a regenerator. The energy management strategy is devised so that the plant operations are dependent on the production profile of the PV plant, using surplus electricity to generate hydrogen.

3.1.2 Integrated PHES configuration

PHES is among the most mature energy storage technologies, currently representing 96% of global energy storage capacity [45]. The plant considered is derived from an existing facility, which includes a 20 MW Francis turbine for electricity generation and 6 electric pumps that can operate individually or in parallel with a power range from 600 kW to 6 MW. In the configuration analyzed, an FPV plant provides the primary energy that powers the pumps, while its surplus production is directly employed for green hydrogen production. Apart from the hydrogen generation, the introduction of the hydrogen production section also allows for reducing the imbalances on the power grid caused by the FPV-PHES system. This way, the integrated system can decouple FPV electricity production from feed-ins, as well as produce hydrogen for external uses.

3.1.3 Integrated ammonia production configuration

The integrated ammonia production configuration is developed with the aim of generating green ammonia from VRES. The system comprises a photovoltaic plant, a battery energy storage system, a proton exchange membrane water electrolyzer, a hydrogen storage unit, and a Haber-Bosch reactor for ammonia synthesis. A Mixed-Integer Linear Programming approach is employed to optimize component sizes and operation scheduling, with a target annual production of 1 kton of ammonia. The performance of this configuration is assessed by conducting a techno-economic optimization of a photovoltaic powered green

ammonia production system, operating under grid curtailment conditions, to minimize the levelized cost of ammonia. Two curtailment scenarios are considered: one in which surplus electricity sold to the grid is valued at the Levelized Cost of Electricity, and an extreme scenario where surplus electricity has zero value.

3.2 Water electrolysis

Hydrogen is essential for each of the configurations considered. High-purity hydrogen from renewable sources is achieved through water electrolysis. This process is inherently energy-intensive, requiring a minimum energy input corresponding to the formation enthalpy of water (285.9 kJ/mol), which corresponds to a theoretical specific energy consumption of 3.55 kWh/Nm³. However, the power consumption for commercial industrial electrolyzers is higher, around 4.5 to 5.0 kWh/Nm³. The overall cell reaction can be described by:

$$H_2O \rightarrow H_2 + \frac{1}{2}O_2 \tag{3.1}$$

Four main technologies for hydrogen production through water electrolysis are currently available [46]: Alkaline, Proton Exchange Membrane, Solid Oxide Electrolyzer Cell (SOEC), and Anion Exchange Membrane (AEM). Alkaline electrolyzers are the most commercially mature and cost-effective, offering high efficiency but with slower response times. PEM electrolyzers show fast response times, high efficiency, and operate at lower temperatures, but require precious metal catalysts, making them more expensive. SOEC electrolyzers stand out for their higher efficiencies due to their operation at high temperatures, though they are limited by longer start-up and response times. AEM electrolyzer, which is now a mature and commercially available technology, has recently gained interest in research and industry, due to the use of cost-effective catalysts, low concentration alkaline solutions [47], and low LCOH when PV-powered (4 $/kg) [48].

3.2.1 Alkaline electrolysis

Alkaline Water Electrolysis (AWE) represents the most mature and commercially established technology for hydrogen production, due to its long operational lifetime that can exceed 90,000 hours, and comparatively low capital costs [49]. This economic advantage depends primarily on the use of a highly alkaline liquid electrolyte, typically an aqueous solution of potassium hydroxide (KOH) or sodium hydroxide (NaOH). This allows for the use of cost-effective non-noble metal electrocatalysts such as nickel, for both the anode and cathode [50]. The system architecture employs a porous separator or diaphragm to physically separate the resulting hydrogen and oxygen gas streams while allowing for the transport of hydroxide ions (OH^-) from the cathode to the anode. The fundamental electrochemical processes occurring at the electrodes are expressed by (3.2) and (3.3).

Anode $$2OH^- \rightarrow H_2O + \frac{1}{2}O_2 + 2e^- \quad (3.2)$$

Cathode $$2H_2O + 2e^- \rightarrow H_2 + 2OH^- \quad (3.3)$$

Commercial AWE systems typically operate at temperatures between 70–90 °C and pressures below 30 bar, with current densities in the range of 0.2 to 0.4 A/cm².

The performance of AWE depends on the total cell voltage, which is a sum of the thermodynamic reversible potential (equal to 1.23 V at standard conditions) and significant voltage losses from various overpotentials. The activation overpotential, particularly at the anode, is a significant problem due to the kinetics of the oxygen evolution reaction, which requires substantial energy to initiate. The ohmic overpotential is a cumulative resistance from the electrodes, the diaphragm, and the electrolyte. This resistance is further increased by the formation of hydrogen and oxygen gas bubbles, which adhere to the electrode surfaces, blocking active catalytic sites, and decreasing the effective conductivity of the electrolyte [50], [51]. The zero-gap geometry, where electrodes are directly in contact with the diaphragm, significantly reduces the ohmic resistance, allowing for higher operational efficiency [51].

These characteristics create some challenges for dynamic operation, particularly when coupled with intermittent VRES. The systems are generally designed for steady-state operation, and their relatively slow dynamic response presents a significant challenge for flexible operation. The dynamic range of AWE is typically 15–100% of its nominal load. Below this minimum value, the correct operation of the electrolyzer becomes problematic due to the increase in gas crossover through the porous diaphragm. Consequently, this reduces the purity of the produced hydrogen and can lead to safety risks [49].

Consequently, research is focused on overcoming these limitations with various approaches. In order to reduce the activation overpotential, researchers are developing advanced electrocatalysts with high surface areas, such as Ni-wire meshes dipped in zinc, Ni-Co alloy nanowires, and complex nanostructures [50]. Innovative separator materials, such as composites of Zirfon with ZrO_2 or Al_2O_3, which offer lower ionic resistance, allow for minimizing gas crossover. This results in improved efficiency and safer operation at lower current densities. Dynamic modeling is being used to design control strategies that can optimize electrolyzer performance under fluctuating power inputs. Recent experimental work has demonstrated that single-cell alkaline electrolyzers can respond rapidly to current variations [49]. For electrolyzers with a narrow dynamic range, large electrochemical storage systems are required to balance the variable power input from VRES with the power requirements of the electrolyzer.

3.2.2 Proton Exchange Membrane

Proton Exchange Membrane (PEM) water electrolyzers are a mature and highly dynamic technology for hydrogen production. PEM electrolyzers present a solid polymer electrolyte, typically a perfluorosulfonic acid membrane such as Nafion, which functions

as both a proton-conductive medium and a physical separator for the gaseous products [52], [53]. At the anode, water is oxidized in the oxygen evolution reaction to form molecular oxygen, hydrogen ions H^+ and electrons. The H^+ migrate through the membrane to the cathode, where they combine with electrons in the hydrogen evolution reaction, forming hydrogen gas. The specific reactions are expressed in (3.4) and (3.5).

Anode $$2H^+ + 2e^- \rightarrow H_2 \quad (3.4)$$

Cathode $$2H_2O \rightarrow H_2 + \frac{1}{2}O \quad (3.5)$$

The PEM cell is composed of a Membrane Electrode Assembly (MEA), which consists of the membrane with catalyst layers, between porous Gas Diffusion Layers (GDLs). Outside, two Bipolar Plates (BPs) are used to manage the transport of water, gases, heat, and electrons [52], [53]. PEM electrolyzers operate under moderate temperatures, typically 50–80°C, and at high pressures of 20–70 bar [54]. They usually operate at nominal current densities of 1-2 A/cm^2, with high efficiencies of up to about 80% [52].

A key advantage of PEM technology is the fast response time and dynamic performance. When supplied with rapid changes in input current, these electrolyzers can reach steady state rapidly [54]. These characteristics make them suitable for VRES implementation, as they are able to follow rapid power input variations. However, a significant challenge comes from the high capital cost, which depends on the material requirements. PEM electrolyzers require platinum-group metal catalysts, which contribute significantly to increasing their costs [53], [54]. The bipolar plates and gas diffusion layers can account for about two thirds of the stack cost [53]. Due to the larger dynamic range compared to alkaline electrolyzers, PEM systems are more compliant with variable power inputs from VRES, allowing for reduced electrochemical storage requirements.

3.2.3 Anion Exchange Membrane

AEM water electrolysis is an emerging technology that aims at offering the combined benefits of AWE and PEM [47], [55]. This system uses a solid polymer membrane to facilitate the selective transport of hydroxide ions OH^- from the cathode to the anode, allowing for the use of non-precious metal catalysts, similar to AWE [56], [57]. This mechanism is described in (3.6) and (3.7).

Anode $$2OH^- \rightarrow H_2O + \frac{1}{2}O_2 + 2e^- \quad (3.6)$$

Cathode $$2H_2O + 2e^- \rightarrow H_2 + 2OH^- \quad (3.7)$$

AEM electrolyzers allow for the use of low-cost transition metals like nickel, cobalt, and iron, for both the OER and HER [55]. In contrast with PEM electrolyzers, these systems do not rely on scarce and expensive platinum group materials. Currently, AEM technology allows for achieving the benefits of PEM systems, such as compact zero-gap cell designs to minimize ohmic losses, while allowing for high-pressure operation and

rapid dynamic response. For these reasons, AEM is being studied for coupling with VRES production to reduce green hydrogen costs [56]. Since their dynamic range allows for easier coupling with VRES, AEM does not require large battery storage systems.

AEM electrolyzers typically operate at temperatures between 40°C and 80°C and can achieve current densities of about 1 A/cm^2. Further studies show potential for up to 2 A/cm^2, which makes it competitive with established technologies [47], [58]. However, this technology still requires research to increase commercial deployment. A significant challenge is the limited chemical stability and durability of AEM in high-pH environments, which limits its lifetime due to high degradation [57].

3.2.4 Solid Oxide Electrolysis Cell

SOEC uses solid ceramic membranes as an electrolyte. A key operational characteristic of SOEC is the requirement for very high operating temperatures, typically in the range of 600–900 °C, which results in high conversion efficiencies due to favorable thermodynamics and reaction kinetics [59], [60]. Compared to PEM, from a thermodynamic point of view, SOEC requires less electric power at nominal temperature conditions [61]. A large portion of the energy required for the electrolysis process is supplied in the form of heat, allowing for the integration in industrial processes or power generation systems where high-temperature waste heat can be recovered and utilized, significantly reducing the specific electric energy consumption and enhancing the overall plant efficiency [60], [62]. The point at which the heat generated by the resistance of the cell is equal to the heat demand of the reaction is the thermoneutral voltage, equal to 1.29 V at 800 °C. Below this voltage, external heat input is required, while above it results in an exothermic process generating excess heat [59], [63].

The process requires steam, which is fed to the porous cathode, where electrical potential allows hydrogen gas and oxygen ions to form. These ions are transported across the electrolyte, usually yttria-stabilized zirconia (YSZ), to reach the anode, where oxygen gas is formed. The reactions are expressed by (3.8) and (3.9).

Anode $$O^{2-} \rightarrow \frac{1}{2} O_2 + 2e^- \tag{3.8}$$

Cathode $$H_2O + 2e^- \rightarrow H_2 + O^{2-} \tag{3.9}$$

The high operating temperatures of up to 900 °C allow for reaching the highest efficiencies among electrolysis technologies, while operating at ambient pressure. SOEC can also operate at high current densities and lower overpotentials, which lead to energy efficiency up to 14% higher than PEM at 1 A/cm^2 [61]. Due to their demanding thermal operating conditions, SOEC might need large battery energy storage to support VRES in providing the thermal energy required.

However, the high temperatures also lead to challenges for long-term durability, which limit industrial implementation. Degradation of the components is a critical problem,

which requires extensive research to develop stable materials and optimized operational strategies [60].

Table 3 summarizes the key characteristics of water electrolysis technologies.

Table 3. Main characteristics of water electrolysis technologies.

	Alkaline	PEM	AEM (anion)	SOEC
Nominal current density [A/cm^2]	0.2-0.8	1-2	0.2-2	0.3-1
Operating temperature [°C]	70-90	50-80	40-60	700-850
Cell pressure [bar]	<30	<70	<35	1
H_2 purity [%]	99.5-99.9998	99.9-99.9999	99.9-99.9999	99.9
Efficiency [%]	50-78	50-83	57-59	89
Stack lifetime [h]	60000	50000 - 80000	>30 000	20 000
Cell area [m^2]	<4	<0.3	<0.1	<0.01
Lower dynamic range [%]	10-40	0-10	5-15	>30
System response	seconds	milliseconds	milliseconds	seconds
Cold start time [min]	<60	<20	<15	<60
Capital cost [€/kWe]	1000-1200	1860-2320	800-1500	>2000

3.2.5 Water for hydrogen production

Water has a critical role in the ammonia production process, being the primary feedstock for electrolysis for hydrogen production. Unlike renewable electricity, water is physically constrained, and its availability varies in different regions.

The fundamental electrochemical reaction for water splitting provides a stoichiometric requirement of about 9 kg of water to produce 1 kg of hydrogen. However, this is a theoretical ideal value, and industrial hydrogen production plants require not only the electrolysis section but also ancillary systems for water treatment and cooling, which significantly increase the overall water demand [64]. The total water withdrawal for alkaline electrolysis is as high as 32.2 L/kgH_2, about 3.6 times higher than the theoretical consumption [64]. The difference between these two values is mainly due to the water consumption required for cooling. Furthermore, the quality of the freshwater feed is critical, particularly for PEM electrolyzers. These systems are highly sensitive to impurities and require high-purity deionized water [65], [66]. For this reason, most hydrogen production plants currently include an on-site purification system, which consumes a small fraction of additional water and energy.

While the water intensity of electrolysis is significant, its impact on freshwater sources may not be critical when compared with other users' consumption. As a matter of fact, the global water demand for future large-scale green hydrogen production could be negligible compared to existing water uses, particularly agriculture and industry [67]. In some cases, large-scale hydrogen production could also reduce water consumption

compared to current fossil fuel energy production. However, this depends on local and regional water availability conditions. About 35% of global planned green and blue hydrogen production plants are located in highly water-stressed regions [64]. Providing freshwater to hydrogen production plants in those areas can generate new problems for local uses. Therefore, in such regions, research on seawater use for electrolysis is essential.

3.2.6 Seawater for hydrogen production

Seawater constitutes over 96% of the total water available, and can be an alternative to freshwater sources, especially in water-stressed regions [66]. Two fundamental methods for seawater use are indirect seawater electrolysis and direct seawater electrolysis. The indirect method uses mature desalination technology to produce freshwater for conventional electrolyzers, while the direct method requires seawater splitting in newly developed electrolyzers.

The indirect method involves a two-step process, where an industrially mature technology such as seawater reverse osmosis (SWRO) is employed for desalination, followed by conventional water electrolysis. The main challenges regard economic and energetic aspects. However, the cost associated with desalination is marginal when compared to the overall cost of hydrogen production. Due to the specific energy consumption of SWRO, the overall consumption for desalination is almost negligible compared to water splitting, as is the capital cost. Overall, the cost of desalination is about 1% of the total cost of green hydrogen [65], [68]. Additionally, this two-step process only increases CO_2 emissions by about 0.1% [65]. Therefore, the existing SWRO infrastructure can provide a technologically ready solution for accelerating green hydrogen production even in areas of scarce freshwater availability and even provide additional purified water for local communities. However, a major challenge concerns the environmental impact of water desalination, which can discharge byproducts at sea due to the use of additives for water treatment.

Direct seawater electrolysis is currently being investigated as a potential one-step solution to hydrogen production from seawater. By avoiding the need for an external desalination unit, the design can be much more compact and simpler [69]. However, seawater as the electrolyte presents various challenges. Seawater is not only saline water, but it also contains various ions, organic matter, and dissolved gases. During electrolysis, chlorine gas is released, leading to degradation of the components [66], [69].

3.3 Ammonia production technologies

Figure 4 illustrates the functional layout of a hydrogen and ammonia production plant. The essential energy and material flows are represented by continuous lines, while the optional energy and material flows are represented by dashed lines. The input power for the system can be provided by a RES plant, such as a photovoltaic plant or a wind turbine plant, but it can also be integrated by the grid. The electrolyzer utilizes electrical energy and water to produce hydrogen and oxygen. Ammonia synthesis requires hydrogen and

nitrogen, where the latter is obtained from an Air Separation Unit (ASU), also generating oxygen. An optional BESS can be included in the plant layout to stabilize the RES plant power fluctuations and provide continuous input power to the components of the plant. Additionally, a desalination unit can produce high-purity water. Dedicated hydrogen and ammonia storage systems are used to regulate the output flows.

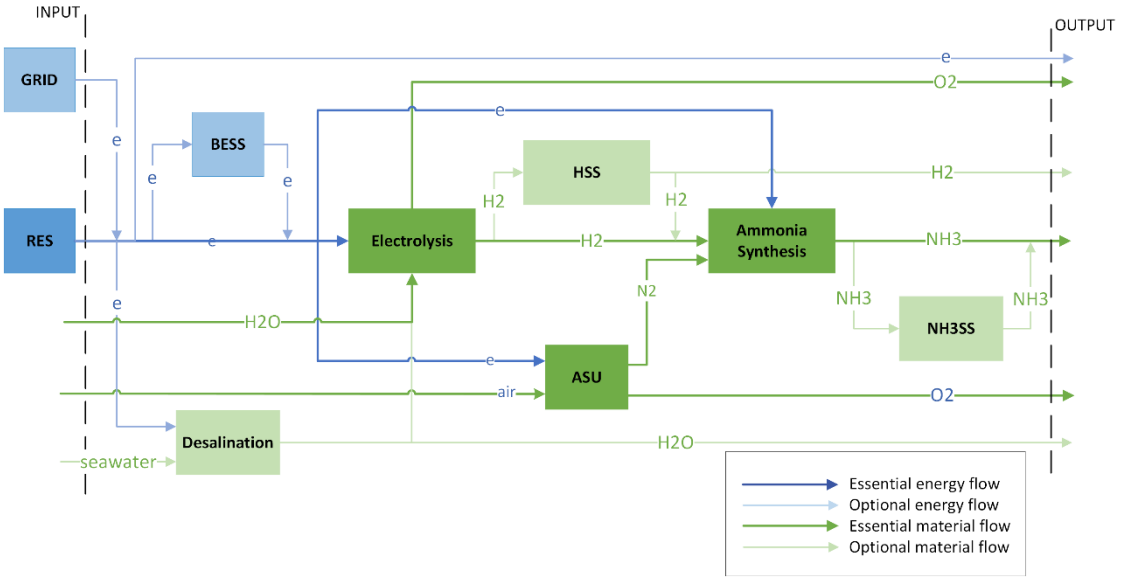

Figure 4. Green ammonia plant configuration.

More in detail, the system's primary power is supplied by a RES source such as a photovoltaic array or wind farm. To address the inherent intermittency and variability of RES generation, a BESS allows for absorption of surplus power during peak generation and releases it to ensure operational stability during periods of low or no generation. Furthermore, a grid connection allows the plant to either draw power to maintain continuous operation or export surplus electricity, thereby creating potential revenue and contributing to grid stability.

The electrolyzer, which consumes a significant share of the electrical energy to perform water electrolysis, produces hydrogen and oxygen from water splitting. The essential material input is high-purity water, which can be provided either by an optional desalination unit, particularly relevant for installations utilizing seawater as a primary water source, or by freshwater sources. The electrolysis process yields the essential hydrogen feedstock for ammonia synthesis and a potentially valuable oxygen byproduct.

In parallel, the ASU is powered by the RES to process atmospheric air, providing the essential nitrogen stream required for the synthesis reaction, while also producing an additional stream of byproduct oxygen. The hydrogen and nitrogen streams are the feedstock input for the NH_3 synthesis unit, typically a Haber-Bosch reactor, where they are catalytically converted into ammonia.

The Haber-Bosch process, first commercialized in the early 20th century, is still by far the most widespread industrial ammonia production technology. Its use is mainly adopted in the fertilizer industry. The process allows for the synthesis of ammonia from its elemental components, nitrogen, and hydrogen. While nitrogen is extracted from air through cryogenic or pressure systems, hydrogen is primarily derived from fossil fuels through steam methane reforming. To develop carbon-free pathways for the energy transition, it is fundamental to conduct research on the chemistry and engineering of the ammonia synthesis loop and finally achieve industrial green ammonia production solutions.

To decouple the variable production rates from the operational requirements of downstream processes, the configuration includes optional tanks. A dedicated HSS can act as a buffer, absorbing fluctuations in hydrogen production from the electrolyzer and ensuring a stable, continuous feed to the synthesis unit, which often requires steady-state conditions for optimal efficiency. Similarly, the Ammonia Storage System (NH3SS) can be employed to store the final product, allowing for strategic management of output flows to align with market demand or transportation logistics. The final outputs of the plant consist of the primary product, ammonia, along with potential byproducts such as oxygen, hydrogen, excess purified water, and electricity.

3.3.1 Haber-Bosch process for green ammonia production

Currently, the process is driven by electrical energy from the grid, and hydrogen is extracted from methane via SMR. Achieving green ammonia production requires adopting RES as the primary energy for each step of the entire process. The core synthesis loop remains the same, but inputs and operational strategies are adapted to operate under RES conditions.

The most significant modification is the complete replacement of the SMR unit. In a green ammonia plant, the feedstock is supplied by two electrically powered units: a water electrolysis unit for green hydrogen production and an ASU for nitrogen production. Therefore, the primary inputs for the plant no longer require natural gas and steam, but only water, air, and renewable energy [26]. All processes are therefore driven by electricity, including the ASU, which in principle remains the same, but uses electric motors instead of steam turbines used in large-scale applications.

An important aspect to be considered in the implementation of RES in the ammonia production system concerns heat integration. In conventional plants, the heat generated from the HB exothermic reactor is used to provide heat to the SMR process. Without the SMR, heat must be managed differently. Some proposed solutions include using heat to drive a steam turbine in a Rankine cycle, generating electricity [53]. While enhancing the overall process efficiency, this solution, however, increases capital costs. Another approach is the integration of a high-temperature Solid Oxide Electrolysis Cell (SOEC) in the system. Heat from the ammonia synthesis loop (exothermic) can be provided to the

SOEC (endothermic) to produce hydrogen, significantly reducing the electricity consumption of the electrolysis step [53].

3.3.2 Ammonia synthesis

The fundamental ammonia synthesis reaction is exothermic and is described by the chemical equation (3.10)

$$N_2 + 3H_2 \rightleftarrows 2NH_3 + 46.1\ kJ\ mol^{-1} \quad (3.10)$$

In the equation, the equilibrium conversion of reactants to products depends on the temperature, pressure, and concentration of the species. Since the reaction is exothermic, lower temperatures favor a higher equilibrium concentration of ammonia. Moreover, higher pressure shifts the equilibrium towards the product side, favoring the formation of ammonia. The ammonia equilibrium concentration can approach 100% at low temperatures and high pressures [70]. However, at low temperatures, the reaction kinetics are extremely slow for industrial applications. The most critical challenge is associated with the dissociative adsorption of dinitrogen, which is the rate-limiting step in the overall reaction [70]. The N_2 triple bond requires significant breaking energy, making the process feasible only at high temperatures. Therefore, in the Haber-Bosch process, high temperatures are required to achieve industrial production rates, but at the same time, this results in an unfavorable equilibrium, reducing the maximum yield. For this reason, modern systems operate a recycle synthesis loop with a single-pass conversion rate of approximately 10-15%, at temperatures of about 400-500 °C [70], [71].

3.3.3 Nitrogen production

Apart from green hydrogen, ammonia production requires gaseous nitrogen as feedstock for the reaction process. Nitrogen must be extracted from air in a dedicated ASU [26].

In large-scale applications, ranging from 1,000 to over 3,000 metric tons per day, the most widely adopted technology is cryogenic distillation, where atmospheric air is cooled to condensation, causing the gases to separate based on their different boiling points [72]. The different boiling points are -196 °C for nitrogen, -183 °C for oxygen, and -186 °C for argon. These systems can produce highly pure nitrogen, but they are generally energy-intensive processes. In smaller applications of approximately 20 to 300 metric tons per day, Pressure Swing Adsorption (PSA) is used as an alternative way to produce nitrogen from air. Composed of a membrane separator and operating at high pressure, these systems, in general, offer better dynamic response [73].

Like the other components of the plant, the ASU has operational constraints regarding cyclical operation and frequent startup and shutdown procedures. To achieve a stable feedstock of nitrogen for the HB unit, a buffer tank is required. Current nitrogen infrastructure is highly developed and industrially mature, allowing for addressing storage issues without significant modifications [74], [75]. Additionally, similarly to electrolyzers, the ASU generates high-purity oxygen as a byproduct, which can provide additional revenues [76].

3.3.4 Haber-Bosch synthesis loop

The primary components of the synthesis loop are: a compressor, an ammonia converter, and a condenser for the separation of the product [70]. A schematic representation of the Haber-Bosch loop is presented in Figure 5.

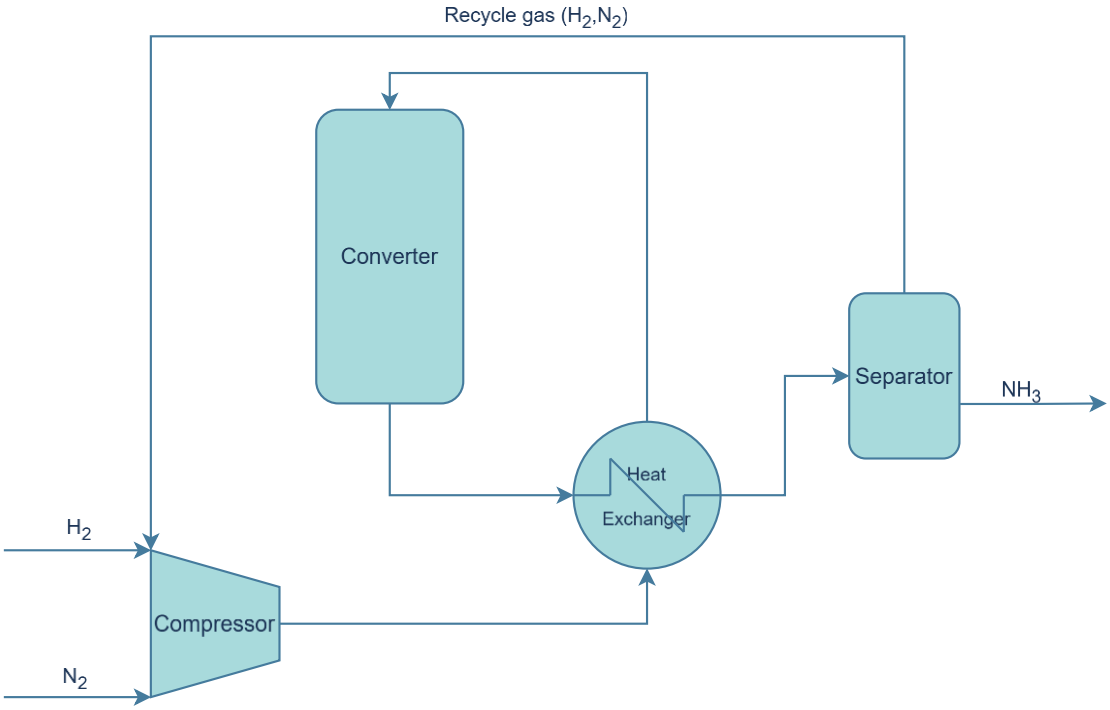

Figure 5. Haber-Bosch synthesis loop.

The first component is the compressor, where syngas composed of high-purity hydrogen and nitrogen is compressed to very high pressures, typically between 140 bar and 200 bar [53]. In large-scale plants, multi-stage centrifugal compressors are employed.

After compression, the syngas flows into the converter, a catalytic reactor where ammonia is synthesized. The most critical component, fundamental for the reaction, is the ammonia catalyst. As discussed, low temperatures favor high equilibrium conversion but slow reaction kinetics, while high temperatures accelerate the reaction, reducing the yield. The role of the catalyst is to increase the rate of reaction without worsening the equilibrium [73].

Currently, industrial ammonia catalysts can be fused iron based or supported metallic catalysts. Fused-iron catalysts are the most common in industrial applications, and they are derived from iron oxides such as hematite (Fe_2O_3), magnetite (Fe_3O_4), or wüstite ($Fe_{1-x}O$). Supported metallic catalysts are based on ruthenium (Ru) or cobalt (Co), supported on a less expensive material to reduce overall costs and increase catalyst activity. Generally, supported metallic catalysts offer a higher activity at lower temperatures compared to fused-iron catalysts [70]. Research on advanced catalysts is focused on increasing activity at low temperatures. Electrides in supported catalysts offer the ability to donate electrons effectively, improving on the rate limiting step of N_2 adsorption [70].

As the process is exothermic, heat dissipation is important to ensure that the catalysts can operate in nominal conditions. In industrial applications, ammonia converters can be classified based on cooling technology, either as quench converters or tube-cooled converters.

Quench converters are the most common design, and they employ multiple adiabatic catalyst beds in series. The gas passes through each bed as the temperature increases. A cold unreacted feed gas is passed through each bed, lowering the temperature of the main gas [53], [70].

Tube-cooled converters include an internal heat exchanger composed of tubes running through the catalyst bed. The cold feed gas, flowing through these tubes, extracts heat from the main gas, preheating itself while removing heat from the catalyst bed [70].

Finally, the last step includes cooling and separation of the feed gas. After exiting the reactor, a series of heat exchangers is used to extract heat from the gas, and usually recycled to preheat the inlet flow, increasing the overall efficiency of the process. Then, a condenser brings the temperature to the boiling point of ammonia at -33.4 °C, which is used to liquefy ammonia. A high-pressure separator removes liquid ammonia from the product, leaving unreacted hydrogen and nitrogen to be recycled back in the compressor at the beginning of the loop, where they are mixed with fresh syngas [71].

3.3.5 Challenges of Haber-Bosch integration with VRES

The most critical challenge for green ammonia production is managing the imbalance in production and consumption, derived from the intermittency of VRES like wind and photovoltaic power plants. Industrial HB plants are optimized for steady-state operation, and frequent startups and shutdowns, as well as ramping up and down, can damage the catalysts, increase degradation, reduce the lifetime, and generally worsen the efficiency. Various strategies can be employed to partially decouple the VRES power supply from the steady-state HB operation, including a buffer hydrogen storage system.

Using high-pressure tanks, hydrogen production can be offset from ammonia production, allowing for the exploitation of the electrolyzers' dynamic response to better adapt to RES variations, while the HB synthesis loop can run continuously at or near its optimal design point by using stored hydrogen at times of low or no power generation [26]. A critical aspect is the sizing and operation scheduling of the hydrogen buffer tank: large storage volumes allow for better decoupling from HB operations at the expense of increased capital costs, while small storage volumes require advanced operational management strategies for HB scheduling with lower investments.

Future developments include flexible synthesis loop operation. HB operation flexibility is defined as the ability of the plant to adjust its production rate in response to changes in feedstock availability and power input. This flexibility involves the turndown ratio, which is the minimum load as a percentage of nominal capacity, its ramp rate, and startup and shutdown times [74]. Current HB plants are designed to operate at constant conditions,

and have a very narrow off-design window of operation in stable conditions, and the ramp-up is typically around 20% of the nominal load per hour [77]. Recent studies show that the most influential parameter for the performance of the plant during ramping operations is the reactor inlet temperature [77]. The part load performance of the HB reactor can be primarily controlled by adjusting the hydrogen to nitrogen ratio, reducing the hydrogen intake to operate at lower turndown ratios, but reducing ammonia yield [72], [74]. Therefore, HB flexibility requires finding a balance between the need for energy and feedstock storage, but with advanced control systems and innovative materials as catalysts, to operate safely in off-design conditions [75].

3.3.6 Alternative ammonia production technologies

Beyond Haber-Bosch technology, significant research is being carried out for alternative ammonia synthesis options, especially for renewable integration. The primary objective is to address the main limitations of the conventional process, such as the high energy consumption, its reliance on fossil fuels, and the need to operate under demanding temperature and pressure conditions [78], [79]. Several new technologies have been developed, including thermochemical, electrochemical, photochemical, and plasma-assisted processes. Among these, thermochemical and electrochemical have emerged as the most promising near-term alternatives due to their higher technological feasibility [79].

Thermochemical ammonia production includes the non-catalytic thermocyclic process, where ammonia is synthesized directly by splitting the reaction into two steps. The main advantage is the ability to operate at atmospheric pressure, eliminating the need for high-pressure reactors, as well as eliminating the hydrogen production process. Therefore, significant capital and operational cost reductions can be achieved [41], [79]. However, this technology requires extremely high temperatures reaching up to 1500 °C for the reduction step, which requires specialized materials and high energy input.

Electrochemical synthesis is another promising process since it can be directly integrated with renewables and operates at moderate conditions. This process can be up to 20% more efficient than the Haber-Bosch process and does not require water electrolysis for hydrogen production [79], [80]. Electrochemical synthesis can be categorized into high-temperature and low-temperature processes. High-temperature electrochemical systems, operating between 300–800 °C, use solid-state, molten salt, or composite electrolytes to facilitate ion transport [81]. A significant challenge is the fact that, while high temperatures increase proton transport and reduce ohmic resistance, they also increase the thermal decomposition rate of ammonia [79], [82]. Low-temperature electrochemical synthesis operates at near ambient conditions, using aqueous electrolytes. In these systems, the main challenge is the fact that most of the electrical energy is consumed in producing hydrogen gas rather than ammonia, with low faradic efficiencies [79], [81]. Research is focused on developing highly selective electrocatalysts to increase the nitrogen reduction reaction rate.

Photochemical synthesis uses semiconductor photocatalysts to absorb solar radiation and generate the nitrogen reduction reaction. This way, sunlight is directly employed for ammonia production. Plasma-assisted synthesis uses an electrical discharge to generate a plasma state where hydrogen and nitrogen molecules can directly combine to form ammonia. These processes, however, are currently only available at lab scale [79].

Chapter 4

Mathematical models

4.1 Mathematical modeling

This chapter presents the mathematical framework employed for the analysis and optimization of the proposed green hydrogen and green ammonia production systems. It presents a set of models that describe the performance of each key component within the plant configurations under study. These models, implemented in MATLAB and GAMS, are used as the basis for the system simulations for technical and economic assessments conducted in this thesis.

The models are presented following the primary energy conversion process, from electricity generation to the final synthesis of ammonia. The equations account for key variables for each technology, including thermodynamic and electrochemical performance, polarization curves, and calculation of overpotentials. These models are used for predicting hydrogen and ammonia production rates as a function of electrical input. The models for ancillary and energy management systems are also presented. These include the compression and expansion trains, as well as the energy storage systems. Finally, individual component models are integrated into the models of the various plant configurations analyzed to determine their technical and economic performance.

To optimize the size and scheduling of the components of the plant, a Mixed-Integer Linear Programming (MILP) model was developed. A MILP model is a mathematical optimization model used to solve problems where a linear objective function is optimized subject to a set of linear equality and inequality constraints [83]. This programming model is capable of handling both continuous decision variables, which can take any value within a given range, and integer variables, which are restricted to integer values. Additionally, binary variables are used to model logical on/off decisions. A MILP optimization model was developed to determine the optimal sizing and hourly operational scheduling of the entire plant. In this analysis, the MILP model is designed to minimize the LCOA and meet a target annual ammonia production while respecting the operational constraints, ramp rates, and physical limits of each component. This modeling approach was selected because the green ammonia plant optimization problem must account for both continuous and discrete decision variables: decision variables such as the power dispatched to and from the BESS are continuous, while decision variables like the number of active electrolyzer units at any given hour are inherently integer. Furthermore, modeling the operational status (on/off) of the Haber-Bosch unit and the activation of different operating segments in component efficiency curves necessitates the use of

binary variables. The linear nature of the framework is maintained by formulating the economic objective function as a linear combination of costs and by approximating the nonlinear performance of components, such as the electrolyzer, through Piece-Wise Affine (PWA) approximations.

4.2 Photovoltaic plant

The PV power production is calculated as:

$$\dot{E}_{PV} = n_{PV} \cdot S_{PV} \cdot GI \cdot f_{PV} \cdot \eta_{INV} \cdot \eta_{PV} \tag{4.1}$$

where n_{PV} is the number of PV modules, S_{PV} the module surface, GI the Global Solar Irradiation, f_{PV} the derating factor for secondary losses, η_{INV} the inverter efficiency (as represented in Figure 6 [31]) and η_{PV} the module conversion efficiency. The module conversion efficiency and the cell temperature are calculated according to Duffie et al. [32] :

$$\eta_{PV} = \eta_{PV,STC} \cdot [1 + \theta \cdot (T_{CELL} - T_{STC})] \tag{4.2}$$

$$T_{CELL} = max\left(T_{AMB}; \frac{T_{AMB} + \left(NOCT - T_{AMB,NOCT}\right)\frac{GI}{GI_{NOCT}}\frac{(1 - \eta_{PV,STC}(1 - \theta T_{STC})}{\tau_\alpha}}{1 + \left(NOCT - T_{AMB,NOCT}\right)\frac{GI}{GI_{NOCT}}\frac{\theta \cdot \eta_{PV,STC}}{\tau_\alpha}} \right) \tag{4.3}$$

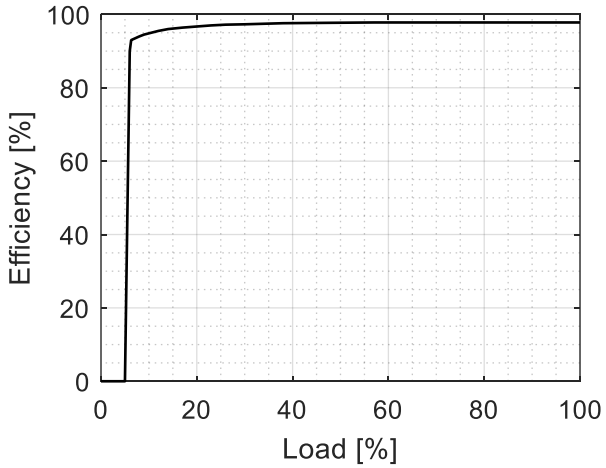

Figure 6. Inverter efficiency as a function of the load.

4.2.1 Floating photovoltaic

The power generation of the FPV system is calculated based on the conversion efficiency of the module, where T_{mod} is the temperature of the module, calculated based on GI, ambient temperature (T_{amb}), and wind speed (U_{wind}) as:

$$T_{mod} = 2.0458 + 0.9458\, T_{amb} + 0.0215\, GI - 1.2376\, U_{wind} \tag{4.4}$$

The equation is an empirical correlation calculated for a tilt angle of 30°, which can be considered valid also for lower tilt angles, given the results of Chowdhury et al. [84], who

found that temperature variations of the module with tilt angles in the range of 10°-30° are negligible.

4.3 PEM electrolyzer

The mathematical model for the PEM electrolyzer is developed based on the work by Zhao et al. [35]. It is a steady-state model, used to calculate the performance of the electrolyzer considering the various losses. The cell voltage V_{cell} is calculated as:

$$V_{cell} = E + \eta_{act} + \eta_{ohm} + \eta_{diff} \tag{4.5}$$

where E is the open circuit voltage, η_{act} is the activation overpotential, η_{ohm} is the ohmic overpotential, and η_{diff} is the diffusion overpotential. The open circuit voltage is calculated from the Nerst equation:

$$E = E_{rev}^{0} + \frac{RT}{zF} \ln\left(\frac{P_{H_2} P_{O_2}^{\frac{1}{2}}}{P_{H_2O}}\right) \tag{4.6}$$

where E_{rev}^{0} is the reversible cell voltage, R is the gas constant, T is the temperature, z is the number of electrons, F is Faraday constant, and P_{H_2}, P_{H_2O} and P_{O_2} are the partial pressures of hydrogen, water, and oxygen, respectively.

The three overpotentials are calculated with the following equations:

$$\eta_{act} = \frac{RT}{\alpha_{PEM} zF} ln\left(\frac{i}{i_0}\right) \tag{4.7}$$

$$\eta_{diff} = \frac{RT}{\beta_{PEM} zF} ln\left(1 + \frac{i}{i_{lim}}\right) \tag{4.8}$$

$$\eta_{ohm} = \frac{\delta_m I}{A \sigma_m} \tag{4.9}$$

where α is the transfer coefficient, i_0 is the exchange current density, β is the constant coefficient, i_{lim} is the diffusion limit current density, δ_m is the thickness of the membrane, and A is the membrane cross section area.

The conductivity of the proton exchange membrane σ_m is calculated as:

$$\sigma_m = (0.005139\lambda_E - 0.00326) \exp\left[1268 \left(\frac{1}{303} - \frac{1}{T}\right)\right] \tag{4.10}$$

where λ_E is the humidification factor.

Finally, the hydrogen production is calculated with the Faraday Law:

$$n_{H_2} = \frac{I}{2F} \tag{4.11}$$

where I is the operating current, calculated based on the input power of the considered electrolyzer [36].

4.4 AEM electrolyzer

The steady-state AEM electrolyzer model is derived from Vidales et al. [85]. The model allows for the estimation of the hydrogen production for a given input power, considering the polarization curve and efficiency of the cell. The number of cells is calculated as the ratio between the nominal power of the stack and the nominal power of the cell, considering a parallel cell configuration.

According to Vidales et al. [85], the activation overpotential - which accounts for kinetic effects - is determined with the Butler-Volmer equation:

$$\eta_{act} = \frac{RT}{\alpha_a F} arcsinh\left(\frac{i}{2i_{0,a}}\right) + \frac{RT}{\alpha_c F} arcsinh\left(\frac{i}{2i_{0,c}}\right) \tag{4.12}$$

where α_a is the charge transfer coefficient for the anode, defined as [86]:

$$0.0675 + 0.00095T \tag{4.13}$$

and α_c is the charge transfer coefficient for the cathode [86]:

$$0.1175 + 0.00095T \tag{4.14}$$

i is the current density, $i_{0,a}$ is the exchange current density for the anode ($5.6 \cdot 10^{-3}$ mA/cm^2 [85]), $i_{0,c}$ is the exchange current density for the cathode (0.191 mA/cm^2 [85]).

The ohmic overpotential is calculated considering both electrolyte and membrane resistances as:

$$\eta_{ohm} = E\left[\frac{1}{\sigma_{KOH}}\left(\frac{d_{am}}{S_a} + \frac{d_{cm}}{S_c}\right) + \frac{\delta_m}{S_m \sigma_m}\right] I \tag{4.15}$$

where σ_{KOH} is the ionic conductivity of the electrolyte (calculated according to Gilliam et al. [87]), d is the distance between the anode and cathode to the membrane respectively, S is the cross-section area for anode, cathode, and membrane, δ_m is the thickness of the membrane, σ_m is the membrane conductivity, and I is the operating current.

The diffusion overpotential is determined [85] as:

$$\eta_{diff} = \frac{RT}{4F} ln\left(\frac{C_{O_2,m}}{C_{O_2,m_0}}\right) + \frac{RT}{2F} ln\left(\frac{C_{H_2,m}}{C_{H_2,m_0}}\right) \tag{4.16}$$

where $C_{O_2,m}$ and $C_{H_2,m}$ are the oxygen and hydrogen concentrations at the interface between membrane and electrolyte, and C_{O_2,m_0} and C_{H_2,m_0} are reference values in working conditions [88].

The oxygen and hydrogen concentrations are determined considering temperature and pressure at the anode and cathode, the geometrical characteristics of the anode and cathode, the molar flows of hydrogen, oxygen, and water, the porosity of the electrodes, and the water transport through the membrane, considering diffusion, electro-osmotic drag, and pressure effects [85].

Figure 7a shows the AEM electrolyzer polarization curve and the hydrogen generation for a cell temperature of 60 °C [85], while Figure 7b shows the specific stack production as a function of the input power, for part load conditions.

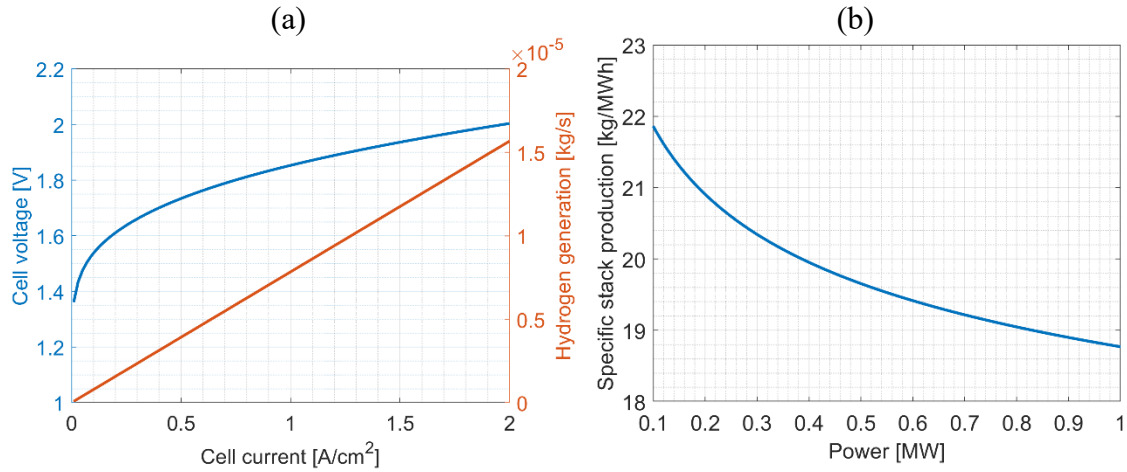

Figure 7. Polarization curve and hydrogen production for the AEM cell (a) and specific stack production as a function of the AEM input power (part-load conditions) (b).

4.5 Compression train

The power required by each compressor of a compression train is calculated as:

$$\dot{E}_{C,i} = \dot{m}_{ch,i} \frac{\gamma_i}{\gamma_i - 1} R_i T_{i,in} \left(\beta_{C,i}^{\frac{\gamma_i - 1}{\gamma_i \eta_{c,i}}} - 1 \right) \tag{4.17}$$

where $\dot{m}_{ch}$ is the mass flow rate of the compressor during the charge phase, γ is the specific heat ratio, R is the gas coefficient of air, T_{in} is the temperature at the inlet side of the compressor, β_C is the pressure ratio of the compressor, η_c is the polytropic efficiency, and the subscript i indicates either air or hydrogen. During charging, when employed in a CAES system, the pressure ratio increases according to the pressure inside the respective storage tank.

The model of the compressor is based on the Casey-Robinson method [89], which allows for the accurate prediction of performance in both design and off-design conditions. The model is specifically adapted to represent the performance of centrifugal compressors. The mathematical model accounts for the aerodynamic stability limits of the centrifugal

compressors to prevent surge. Withing the Casey-Robinson modeling method, the stable operating range of each stage is defined considering a minimum mass flow rate to ensure correct operation at partial load. This limit represents the surge line, below which the flow becomes unstable. When implemented in CAES systems, the compressors operate within the boundaries of the energy management strategy, where if the available renewable power is not sufficient to maintain the operating point within the stable region of the compressor map, the compression train is deactivated, and the power is directed elsewhere.

As the target outlet pressure varies, the compressor operates with a variable pressure ratio and, for a given mass flow rate, the rotational speed changes accordingly. Figure 8 shows the generalized efficiency profile of the compressor as a function of the generalized pressure ratio. It can be observed that the polytropic efficiency is highly sensitive to the pressure ratio. When decreasing the pressure ratio, the efficiency decreases significantly, with reduced rotational speeds. At low pressure ratios, the efficiency is significantly lower compared to the design point. Instead, for a generalized pressure ratio higher than 0.7, the efficiency is more than 90% of the design efficiency.

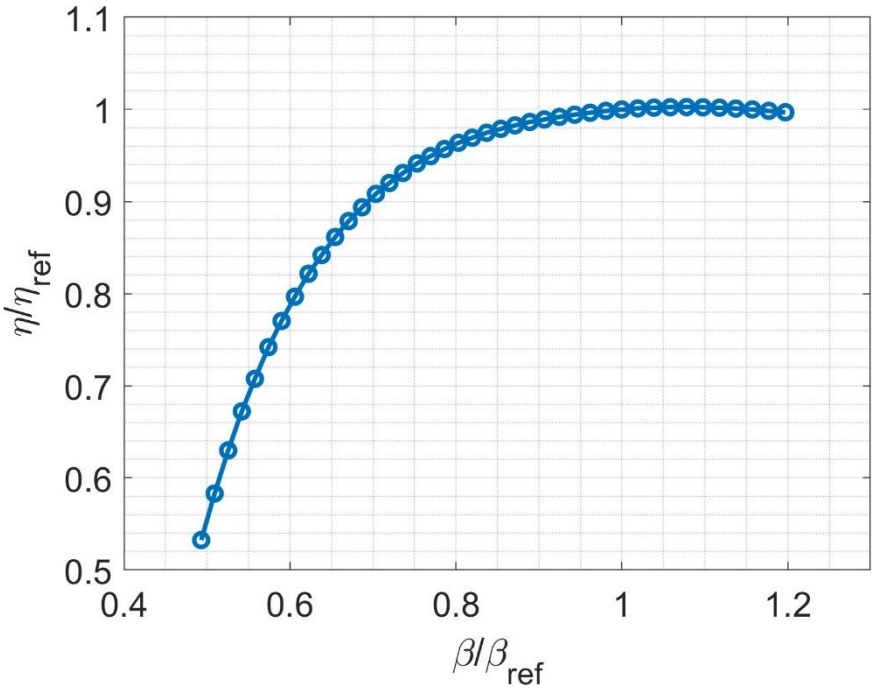

Figure 8. Compressor generalized efficiency profile.

4.6 Expansion train

According to Skabelund et al. [39], the expansion train is assumed to operate in a steady-state condition and with constant isentropic efficiencies for the turbines. Furthermore, except for the combustion chambers (CC), all components are modeled without thermal and pressure losses.

The mass flow rate at the inlet of each turbine $\dot{m}_T$ is the sum of the mass flow rates of air $\dot{m}_{air}$ and fuel $\dot{m}_{fuel}$ and depends on the air-fuel ratio, which is calculated by solving the CC energy balance equation:

$$\alpha_{CC} = \frac{\dot{m}_{air}}{\dot{m}_{fuel}} = \frac{(LHV + h_{H2}) \cdot \eta_{CC} - h_g}{h_g - h_{air}} \tag{4.18}$$

where α_{CC} is the air-fuel ratio, LHV is the lower heating value of the fuel, and h_{H2}, h_{air} and h_g are the enthalpies of hydrogen, of the air, and of the exhaust gas, respectively.

The power of each turbine is calculated by the following equation:

$$\dot{E}_t = \dot{m}_{dch} \frac{\gamma_g}{\gamma_g - 1} R_g T_{in} \left(1 - \beta_t^{\frac{\gamma_g - 1}{\gamma_g} \eta_t} \right) \tag{4.19}$$

where $\dot{m}_{dch}$ is the mass flow rate of the turbine during the discharge phase.

To operate the expansion train in constant pressure mode [29], pressure regulators (PR) are modeled as adiabatic processes [40]:

$$T_{out} = T_{in} \cdot \left(\frac{p_{out}}{p_{in}} \right)^{\frac{\gamma - 1}{\gamma}} \tag{4.20}$$

4.7 Storage volume for air and hydrogen

In a CAES system, for given values of both the rated power of the compression train and the turbines, the charge time and the discharge time strictly depend on the air and hydrogen storage capacities. The air storage volume and the hydrogen storage volume are calculated by starting from the required nominal flow rate of air and fuel [40].

The storage reservoirs for both compressed air and hydrogen are modeled as isochoric fixed volume systems. The storage phase is considered isothermal, assuming that the stored gas reaches thermal equilibrium with the surroundings at the constant storage temperature. Consequently, while the state of charge is governed by the mass balance of the gas, the simulation dynamically calculated the internal pressure variation at each time step. Therefore, the power consumption of the compressors varies as a function of the pressure inside the storage volume and increases as the state of charge decreases.

The following system of equations is solved to determine the total storage volume and the mass stored at minimum pressure for both the air and hydrogen storage systems.

$$\begin{cases} p_{min,i} Vol_{tot,i} = m_{min,i} R_i T_{st,i} \\ p_{max,i} Vol_{tot,i} = (m_{min,i} + \dot{m}_i t_c) R_i T_{st,i} \end{cases} \tag{4.21}$$

where p_{min} is the minimum storage pressure, Vol_{tot} is the total storage volume, m_i is the mass stored, R_i is the gas coefficient, T_{st} is the storage temperature, p_{max} is the maximum storage pressure, $\dot{m}_i$ is the charge mass flow rate, and t_c is the charge time and the suffix i stands for either air or hydrogen.

4.8 Hydroelectric turbine and pump

The power output of the Francis turbine is a function of the water flow rate (Q_T) and of the head (h_T), which is directly proportional to the volume of water stored in the upper reservoir (V_{UP}).

$$P_T = (\rho g h_T Q_T)\, \eta_T \tag{4.22}$$

The generalized $P_T/P_{T,ref}$ and $\eta_T/\eta_{T,ref}$ curves (that is referred to the reference values) are reported in Figure 9 as a function of the generalized $Q_T/Q_{T,ref}$ values [90]. The hydraulic efficiency curve, denoted by the solid blue line, represents the usual non-linear performance behavior of reaction turbines. At high loads these turbines operate at high-efficiency, that drastically decline at partial loads due to off-design hydraulic losses. The region between the minimum and maximum allowed heads shows the operating range between full and empty reservoir capacity. It can be observed that, at constant reduced volumetric flow rates, the efficiency is highly dependent on the head, resulting in highly variable power outputs. Specifically, the turbine power range is constrained by the minimum (66 m) and maximum (118 m) allowable head while η_T is included within the range 50.9-91.1%, with the peak occurring for $Q_T/Q_{T,ref}$ around 0.8 (that is Q_T around 24 m^3/s).

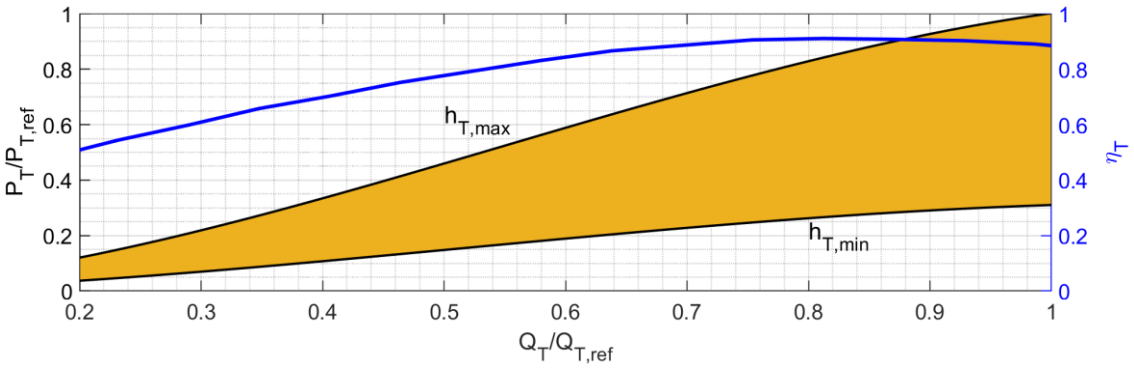

Figure 9. Generalized power and efficiency curves as a function of the generalized volumetric flow rate for the Francis turbine.

The performance of the water pumping section is evaluated by considering six constant-speed electric pumps, two of Type 1 (0.627 MW) and four of Type 2 (1.205 MW). Figure 10 reports the characteristic curves and the efficiency of each electric pump and shows the maximum and minimum values for head and volumetric flow rate for both pumps. In particular, the curves show how these pumps must overcome higher geodetic heads as the upper reservoir fills, consequently leading to a reduction in the volumetric flow rate. The head required by the pumps is modeled by considering the geodetic head between the two reservoirs and the piping energy losses. Variations in atmospheric pressure between the elevations and the fluid velocities at the intake and discharge points were considered negligible. Furthermore, piping energy losses include only distributed losses, while concentrated losses were considered negligible.

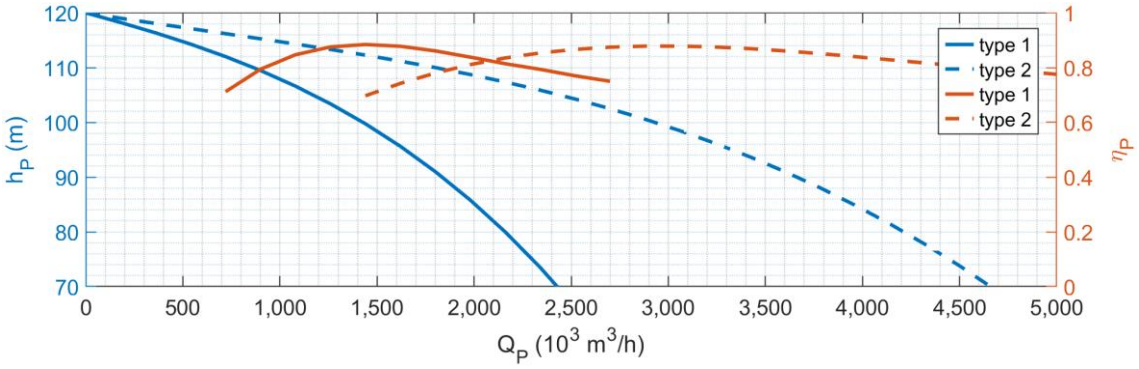

Figure 10. Type 1 and type 2 electropump characteristic curves.

4.9 Ammonia production optimization

To optimize the size and scheduling of the components of the plant, a MILP model was developed. The model aims at minimizing the total system cost over its lifetime, while determining the optimal sizing of key components and their optimal hourly operation strategy, to meet the predefined ammonia production target while minimizing the LCOA. The model is characterized by an optimization horizon of 8760 hours (1 year) with a time step of 1 h. The model was implemented using the software General Algebraic Modeling System (GAMS) version 39.3.0 [91] and employing the CPLEX solver.

The decision variables include power dispatch from the PV plant to the various components, the number of active electrolyzer units, the BESS charge and discharge cycles, the HB operation, and their respective loads. The model is devised to meet an annual total production target of 1 kton of green ammonia, while the residual hydrogen in the HSS and BESS state of charge must be equal to zero.

The approach also includes some assumptions and limitations. First, a perfect forecast is assumed for the PV generation profiles. This assumption allows to calculate the optimal size and scheduling. Secondly, the HB unit is operated only at nominal load, due to the fact that its flexibility is very limited [72], therefore, the model does not take into account part load performance. Additionally, its startup and shutdown times are simplified.

4.10 Objective function

The objective function is expressed as the minimization of the net present cost of the system over the plant lifetime. This cost includes the CAPEX and the Operational Expenditures (OPEX), accounting for the discount rate [92]. The objective function is formulated as:

$$\min OF = \sum_{k \in K} CAPEX_k \cdot S_k + \left(\sum_{k \in K} OPEX_k \cdot S_k \right) \cdot \sum_{y=1}^{N} \frac{1}{(1+r)^y} \qquad (4.23)$$

where OF is the objective function, K represents the set of the components of the plant, $CAPEX_k$ is the specific capital expenditure of the component k, $OPEX_k$ is the specific annual operational expenditure of the component k, S_k represents the specific size of the

component k, N is the plant lifetime in number of years, r is the discount rate and y is the specific year.

The total CAPEX is defined as:

$$CAPEX = C_{PV} + C_{BESS} + C_{EL} + C_{H2SS} + C_{HB} \tag{4.24}$$

The total OPEX is defined as:

$$OPEX = O_{PV} + O_{BESS} + O_{EL} + O_{H2SS} + O_{HB} \tag{4.25}$$

While S_k is represented by:

$$S_k = n_{PV} + SOC_{BESS,max} + n_{EL} + SOC_{H2SS,max} + n_{HB} \tag{4.26}$$

where C represents the capital costs and O the operational costs.

4.11 Balance equation

The model presents several equations to represent the interaction between the components and constraints to ensure the correct operation of the components within their operational limits.

The energy balance equation, which establishes that the total power generated is equal to the total power consumed, is represented as:

$$P_{PV}(t) + P^{d}_{BESS}(t) = P^{c}_{BESS}(t) + P_{EL}(t) + P_{HB}(t) + P_{grid}(t) \quad \forall t \tag{4.27}$$

Where P_{PV} is the photovoltaic power output, P^{d}_{BESS} is the BESS discharge power, P^{c}_{BESS} is the BESS charge power, P_{EL} is the power required by the electrolyzer, P_{HB} is the power required by the ammonia synthesis unit, P_{grid} is the power exchanged with the grid.

4.12 BESS model and constraints

The State Of Charge (SOC) of the BESS is modelled considering the charging and discharging power and efficiency as:

$$SOC_{BESS,t} = SOC_{BESS,t-1} + P^{c}_{BESS,t}\eta^{c}_{BESS} - \frac{P^{d}_{BESS,t}}{\eta^{d}_{BESS}} \quad \forall t \tag{4.28}$$

The SOC is bounded by its minimum ($E_{BESS,min}$) and maximum ($E_{BESS,max}$) capacity, and the charge and discharge power are correlated by the C-rate, which is set to 0.25 [93].

$$SOC_{BESS,ini} = 0.25 \tag{4.29}$$

$$SOC_{BESS,min} \leq SOC_{BESS,t} \leq E_{BESS,max} \quad \forall t \tag{4.30}$$

$$P^{c}_{BESS,t} \leq 0.25 \cdot E_{BESS,max} \quad \forall t \tag{4.31}$$

$$P^{d}_{BESS,t} \leq 0.25 \cdot E_{BESS,max} \quad \forall t \tag{4.32}$$

4.13 HSS model and constraints

The hydrogen storage system is modeled by means of the state of charge equation, by the constraints on the maximum and minimum mass of hydrogen stored, and the final state of charge, which is set to zero.

$$SOC_{H2SS,t} = SOC_{H2SS,t-1} + \dot{m}^{prod}_{H2,t} - \dot{m}^{cons}_{H2,t} \quad \forall t \tag{4.33}$$

$$0 \leq SOC_{H2SS,t} \leq m_{H2SS,max} \quad \forall t \tag{4.34}$$

$$SOC_{H2SS,end} = 0 \tag{4.35}$$

4.14 Ammonia storage model and constraints

The ammonia storage system is modeled by means of the state of charge equation, by the constraints on the maximum and minimum mass of ammonia stored, and the final state of charge, which is set to reach a yearly production target.

$$SOC_{NH3SS,t} = SOC_{NH3SS,t-1} + \dot{m}^{prod}_{NH3,t} \quad \forall t \tag{4.36}$$

$$0 \leq SOC_{NH3SS,t} \leq m_{NH3SS,max} \quad \forall t \tag{4.37}$$

$$SOC_{NH3SS,end} = m_{NH3,target} \tag{4.38}$$

4.15 Electrolyzer model and constraints

The part-load performance of the electrolyzer was modelled by considering the nonlinear correlation between power and hydrogen production. The nonlinear efficiency is implemented in the linear optimization model by employing a PWA function for the linear approximation [94], [95]. The input power and the hydrogen production mass flow rate are linked by means of weight variables ($w_{bp,t}$) at various power breakpoints. The power of the electrolyzer and its hydrogen yield are represented as:

$$P_{EL,t} = \sum_{bp} P_{EL,bp} \cdot w_{bp,t} \quad \forall t \tag{4.39}$$

$$\dot{m}^{prod}_{H2,t} = \sum_{bp} \dot{m}^{prod}_{H2,bp} \cdot w_{bp,t} \quad \forall t \tag{4.40}$$

The sum of the weight variables equals the number of operating electrolyzer units ($n^{oper}_{EL,t}$):

$$\sum_{bp} \lambda_{bp,t} = \mathrm{n}_{\mathrm{EL,t}}^{\mathrm{oper}} \quad \forall t \tag{4.41}$$

The number of operating electrolyzer units, which can vary at each time step, must be lower or equal to the total installed units:

$$\mathrm{n}_{\mathrm{EL,t}}^{\mathrm{oper}} = \mathrm{n}_{\mathrm{EL}} \quad \forall t \tag{4.42}$$

The power of the electrolyzer is constrained by the minimum and maximum power limits of the operating unit, as well as the maximum (RU_{EL}) and minimum (RU_{EL}) ramp rates:

$$P_{EL,min} \leq P_{EL,t} \leq P_{EL,max} \quad \forall t \tag{4.43}$$

$$P_{EL,t+1} - P_{EL,t} \leq RU_{EL} \quad \forall t \tag{4.44}$$

$$P_{EL,t-1} - P_{EL,t} \leq RD_{EL} \quad \forall t \tag{4.45}$$

4.16 Ammonia synthesis model and constraints

Ammonia production is directly proportional to the power consumed by the HB unit and its specific energy consumption. The specific energy consumption comprises the energy consumption of the ammonia synthesis loop, the energy consumption of the ASU, and the energy consumption of the hydrogen compression unit. In fact, the synthesis requires both nitrogen, extracted from air through the ASU, and hydrogen, which is compressed from 30 bar to 200 bar before entering the HB unit.

Ammonia production and hydrogen consumption are calculated as:

$$\dot{m}_{NH3,t}^{prod} = e_{HB} \cdot P_{HB} \quad \forall t \tag{4.46}$$

$$\dot{m}_{H2,t}^{cons} = \sigma_{HB} \cdot \dot{m}_{NH3,t}^{prod} \quad \forall t \tag{4.47}$$

The HB unit operation is constrained by the minimum and maximum power limits, as well as the ramp-up and ramp-down rates.

$$P_{NH3,min} \leq P_{NH3,t} \leq P_{NH3,max} \quad \forall t \tag{4.48}$$

$$P_{NH3,t+1} - P_{EL,t} \leq RU_{NH3} \quad \forall t \tag{4.49}$$

$$P_{EL,t-1} - P_{EL,t} \leq RD_{EL} \quad \forall t \tag{4.50}$$

4.17 Levelized cost of ammonia

As the objective function of the model is the minimization of costs, the LCOA is calculated after solving the MILP problem. As a previous step, the Levelized Cost Of Ammonia (LCOA) is calculated considering the CAPEX, OPEX, discount rate, lifetime, annual degradation, and total ammonia production. The LCOA is calculated as:

$$LCOA = \frac{CAPEX_{tot} + \sum_{n=1}^{N} \frac{OPEX_{tot}}{(1+r)^n}}{\sum_{n=1}^{N} \frac{m_{NH3,tot}}{(1+r)^n}} \quad (4.51)$$

Where $m_{NH3,tot}$ is the total ammonia production.

4.18 Water footprint assessment

To determine the water withdrawal required to substitute a specific amount of electricity generated from fossil fuels with electricity generated via a green hydrogen chain, a mathematical model is developed.

The required renewable energy input required to match the target fossil fuel generation is calculated by dividing the target energy generation by the round-trip efficiency of the PtP process:

$$E_{in,RES} = \frac{E_{gen}}{\eta_{PtP}} \quad (4.52)$$

Where $E_{in,RES}$ is the energy input from RES, E_{gen} is the target energy generation, and η_{PtP} is the Power-to-Power efficiency.

The corresponding mass of hydrogen produced by using this renewable energy input is then calculated based on and the specific energy consumption of the electrolyzer:

$$m_{H2} = \frac{E_{in,RES}}{e_{EL}} \quad (4.53)$$

Where m_{H2} is the mass of hydrogen produced, and e_{EL} is the specific energy consumption of the electrolyzer.

The total water withdrawal for the green hydrogen scenario is calculated as the sum of the water withdrawal required by the renewable power generation plant and the water withdrawal associated with the electrolysis process:

$$W_{tot} = W_{RES} + W_{EL} \quad (4.54)$$

Where W_{RES} and W_{EL} represent the water demand of RES and electrolyzer systems respectively, calculated considering the corresponding water specific consumptions.

4.19 Limitations and uncertainties

The mathematical framework presented in this chapter provides a basis for the techno-economic optimization of the integrated energy systems here analyzed. However, the results include specific limitations due to some adopted assumptions.

The modeling of the Haber-Bosch synthesis unit assumes operation at nominal steady-state conditions. This approach, although in line with current industrial ammonia plant constraints, simplifies the dynamics and control strategies required for flexible operation mode with high ramp rates. The MILP model for the optimization of the ammonia production plant operates under the assumption of perfect forecast regarding photovoltaic irradiance profiles. In real applications, rolling horizon strategies allow for error prediction and may produce deviations from the global optimum calculated in this analysis. The economic indicators are in some cases simplified as they depend on cost projections for future technological implementations that have not reached full commercial maturity. Similarly, degradation is not described through a physics-based model; rather, it is represented using an economic approach. In particular, for electrolyzer stacks, degradation is linearized and included through economic indexes, where progressive performance deterioration is modeled as a time-dependent increase in operational expenditure, representing the associated economic impact.

Chapter 5

Integrated green hydrogen and ammonia systems

5.1 Introduction to integrated systems

This chapter presents a comprehensive analysis of two integrated green hydrogen system configurations in the context of an increasing share of VRES in modern electrical grids. The increasing share of VRES poses significant challenges to the electric grids: in many countries with a VRES share above 20% and limited synchronous interconnections with neighboring states, the lack of grid flexibility requires frequent generation curtailment and load shedding to maintain grid security [96]. For example, California's yearly PV curtailments, which reached 22% in April 2023, almost doubled during the last five years, rising from 3.2% in 2019 up to 6.2% in 2022 [97]. Apart from the environmental detriment, RES generation curtailment entails other adverse effects: in fact, it reduces RES economic convenience and attractiveness [98]. For these reasons, several authors, including López et al. [99], stated that, in regions like California, the foreseen growth in VRES penetration will increasingly require measures to mitigate generation curtailment and address grid flexibility challenges. Among the useful actions, IEA [100], in agreement with the scientific community, considers as key measures the introduction of ESS, the deployment of RES power plants able to provide inertia, and the growth of demand response services.

The surplus energy generation from VRES is increasing globally, and it also comes from a large number of small-scale systems. This energy surplus is primarily managed in three ways: it can be stored, exported to neighboring countries (even at a zero or negative price), or curtailed [96]. Instances of the latter are becoming more frequent worldwide: in the EU, surplus energy from neighboring countries is sometimes imported for free and used to operate PHES systems.

Apart from BESS, which are expected to account in Europe for a 20-30% share of total dispatchable capacity energy by 2050, Thermo Mechanical Energy Storage (TMES) and hydrogen are among the most promising technologies for decarbonizing energy systems [101], providing flexibility services [102] and improving grid adequacy [103], even for small scale applications.

To mitigate these issues, Energy Storage Systems have been identified as a crucial technology. Particularly, two systems for hydrogen integration have been studied and are

presented in this chapter: one coupled with Compressed Air Energy Storage and another with Pumped Hydro Energy Storage.

However, the production of green hydrogen via electrolysis is an energy and water-intensive process. Consequently, a thorough assessment of the water footprint associated with hydrogen-based energy systems is conducted and presented in this chapter.

5.2 Impact of hydrogen production on freshwater sources

Large-scale hydrogen production will create significant demand for freshwater, critically impacting water-scarce regions. Water use for hydrogen production should be taken into account when developing new plants, as suggested by IRENA and Bluerisk (2023). Water use is calculated based on water withdrawal and consumption. Water withdrawal is returned to the body of water from which it was extracted, while water consumption includes all water that cannot be returned. The impact of freshwater abstractions from the local network can be measured using the water stress indicator, a Sustainable Development Goal (SDG) of the 2023 Agenda program, which determines the pressure on freshwater resources caused by abstractions [104].

On a global scale, the impact of water use for hydrogen production is low, but on a local scale, it can become a critical issue, especially in water-stressed areas [69], as electrochemical water splitting is an energy-intensive process that requires about 9 kg of water per kg of hydrogen produced. Moreover, water is not only required for H_2 production but also for cooling needs. Future predictions indicate a global annual water consumption of about 20.7 Gt by 2040, and the water withdrawal share for hydrogen production in the energy sector will account for about 2.4% by 2040 [64].

Green hydrogen production is favorable in areas with high availability of RES, such as North Africa or the southern regions of Europe. However, the water use associated with the electrolysis process may cause problems for the water network, where freshwater is scarce and water stress is high. A promising solution for hydrogen production without freshwater consumption is represented by seawater electrolysis. To address these issues, some studies suggest the use of seawater electrolysis technologies in coastal and arid regions [69]. Two seawater electrolysis technologies exist: Direct Seawater Electrolysis (DSE) uses seawater as a direct water feed, while Indirect Seawater Electrolysis (ISE) is a two-step process that requires water treatment and purification before electrolysis.

Recently, many researchers have focused their efforts on investigating seawater electrolysis technologies, as demonstrated by the increased number of publications in the last few years [65], [66]. Many studies compared the performance of direct and indirect water electrolysis systems. Khan et al. [65] compared the performance of direct seawater electrolysis to a PEM electrolyzer coupled with a SWRO plant, evaluating energy consumption, costs, and environmental impact. They concluded that the indirect system using SWRO shows a minimal increase in the LCOH, energy consumption, and CO_2 emissions. Specifically, they determined a 0.1% increase in energy consumption and a

0.6% increase in LCOH. Hausmann et al. [68] analyzed the energy consumption and costs of DSE compared to a two-step seawater purification and electrolysis process. In the study, DSE is proposed to reduce freshwater use, even if the authors highlighted the challenges of this new technology. They concluded that DSE does not show significant benefits compared to ISE and suggested driving research efforts towards more advanced purification systems to increase water purity. In their study, the authors estimated that, if all electrical energy were produced using hydrogen fuel cells, the freshwater required for electrolysis would constitute just 0.4% of global freshwater use and 2% for all primary energy. Dresp et al. [69] conducted a thorough analysis of hydrogen production from renewable sources, particularly in arid and coastal areas. This paper analyzes the electrochemical reactions and the challenges of DSE. Moreover, the energy consumption of reverse seawater electrolysis, using a fuel cell to generate electricity and freshwater, is calculated. They also compared DSE and ISE technologies, concluding that DSE may be implemented in offshore applications. Farràs et al. [66] reviewed scientific literature on the topic of hydrogen production from seawater. They concluded that currently, DSE is not competitive against ISE because of technical challenges that must first be addressed. However, future developments in this technology field are fundamental, as DSE is a promising solution in specific applications. The authors highlight the mismatch between the small scale of current commercial electrolyzers and SWRO plants, which are usually large. Moreover, they point out the importance of assessing the footprint of these systems. Beswick et al. [67] conducted a study to determine the water use of green hydrogen production. The study demonstrates that water use for electrolysis has a negligible impact on global resources. SWRO's increase in energy consumption is marginal, and so is the increase in LCOH. Moreover, the analysis suggests that substituting RES and hydrogen for fossil fuels for electricity production will result in water use reduction. The authors finally suggest increasing efforts to develop high-efficiency electrolyzers.

The results of these studies indicate a minor difference in energy and costs between the two technologies, in favor of DSE. However, there is limited consideration of the impact of seawater electrolysis on local freshwater resources, focusing instead on broader-scale applications. Moreover, many studies lack a thorough assessment of the energy use of the two systems at the local scale, considering different electrolyzer and water purification systems. The size mismatch between commercial SWRO and water electrolyzers has not been addressed yet. Additionally, real data for energy production should be used. Moreover, the energy sector is currently dominated by fossil fuels, with renewable energy rising rapidly, especially in Europe. As increasing amounts of green hydrogen for electricity generation will increase water abstractions, the associated challenges must be evaluated and addressed.

Within this context, the water and energy consumption of green hydrogen in the energy sector is investigated, with a focus on seawater electrolysis as a sustainable alternative to freshwater usage. The analysis is carried out considering the entire power-to-power process, involving renewable energy generation, water electrolysis, and electricity generation using solid oxide fuel cells. The water and energy impacts of both indirect and

direct seawater electrolysis are assessed and compared across nine countries with varying levels of water stress and different energy mixes. A comprehensive analysis of water and energy use for hydrogen production is conducted, spanning from Northern Europe to North Africa regions. Specifically, focusing on Algeria (DZ), Denmark (DK), Germany (DE), Italy (IT), Libya (LY), the Netherlands (NL), Norway (NO), Sweden (SE), and Tunisia (TN). Each region is characterized by different levels of water stress, water withdrawal, energy generation levels, energy generation shares by source, and RES penetration, but they all have direct access to seawater.

5.2.1 Water stress and withdrawal

Water stress [104] data used for this analysis were obtained from the UN Water Organization database, which provides data for agricultural, industrial, and service use [105]. While the latest available data refers to 2020, historical trends demonstrate minimal variations in water use over time.

Figure 11 shows the water stress levels (Figure 11a) and annual water withdrawal (Figure 11b) for the regions considered. Figure 11a shows a significant variability in water stress levels across the regions. Arid regions and countries with limited access to freshwater resources tend to have higher water stress levels. Figure 11b illustrates the annual total withdrawal of water for the countries considered. Considerable differences can be observed across the regions, ranging from about 1 Gm^3/year to about 34 Gm^3/year. Regional patterns can be identified, where European countries have generally higher water withdrawals compared to North African regions. Comparing water stress and withdrawal data, the disparities can be attributed to geographic factors like climate and freshwater availability, but also to the efficiency of the different water management strategies of the countries.

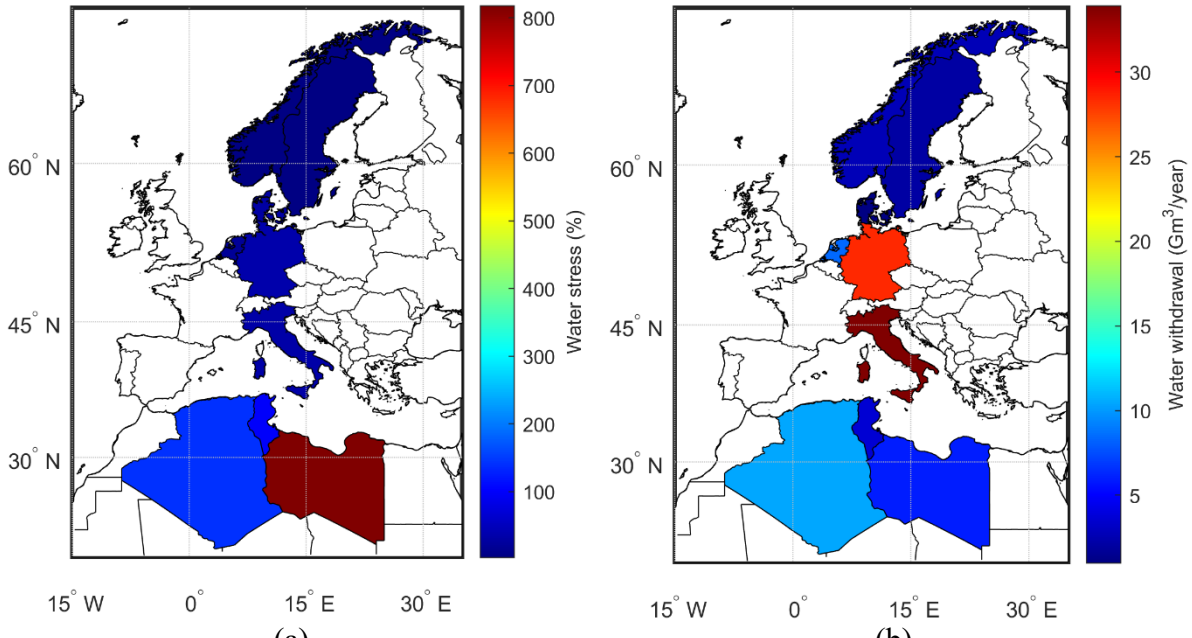

Figure 11. (a) Water stress levels and (b) water withdrawal for the countries analyzed.

Figure 12 illustrates the electricity generation mix and the total energy generation for each region. The electricity generation mix data, divided by source, was derived from the IEA database [106] for the year 2020, to maintain consistency with the water data used in this analysis.

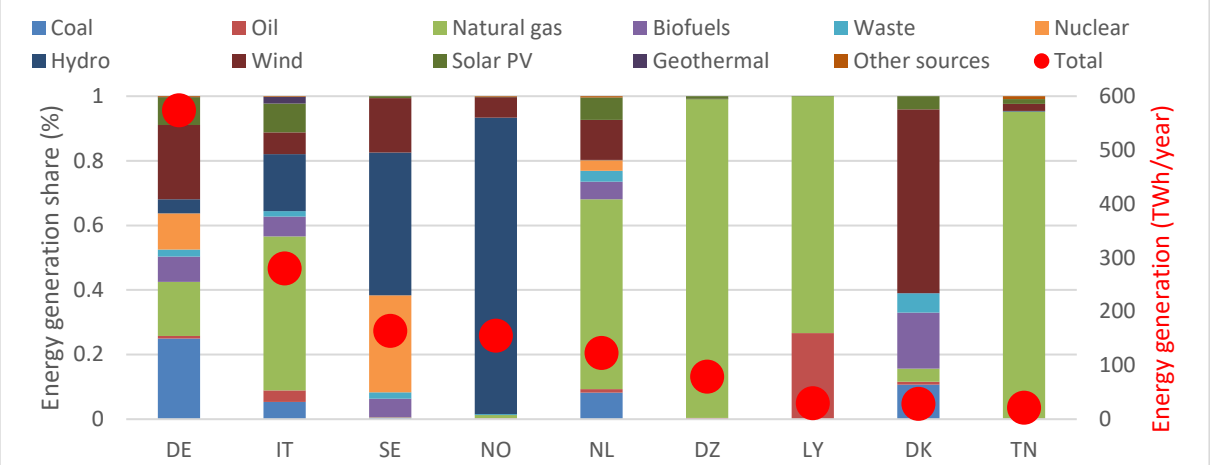

Figure 12. Energy generation share and total annual energy generation for each region analyzed.

Table 4 summarizes the data used in this analysis regarding water stress, annual water withdrawal, and annual electricity generation for each country. Various degrees of water stress are categorized into five levels, such as no stress (<25%), low (25-50%), medium (50-75%), high (75-100%), and critical (>100%) stress. All data refers to 2020. Overall, the data shows the diverse challenges regarding water resource utilization in hydrogen production for electricity generation across different regions.

Table 4: Summary of data regarding water stress, annual water withdrawal, and annual electricity generation for each country.

	NO	SE	DK	DE	NL	IT	LY	TN	DZ
Water stress (%)	2.05	3.58	26.40	33.50	16.8	29.81	817.14	98.11	137.92
Water withdrawal (Gm^3/year)	2.69	2.07	0.98	28.48	8.31	33.89	5.83	3.59	10.46
Energy generation (TWh/year)	155.2	163.8	28.7	575.5	123.3	280.5	29.5	21.5	79.1

5.2.2 Water withdrawal for electricity and hydrogen generation

Extensive research has been conducted over the last decades to assess the water intensity of different technologies for electricity production [107], [108], [109], determining specific water withdrawal rates. In this analysis, the most recent data available [110] was

selected for the analysis of the water withdrawal of different technologies. In their study, the authors analyzed water use from surface or irrigation for different applications and considered different regions. Figure 13 shows the water withdrawal of different technologies for electricity generation.

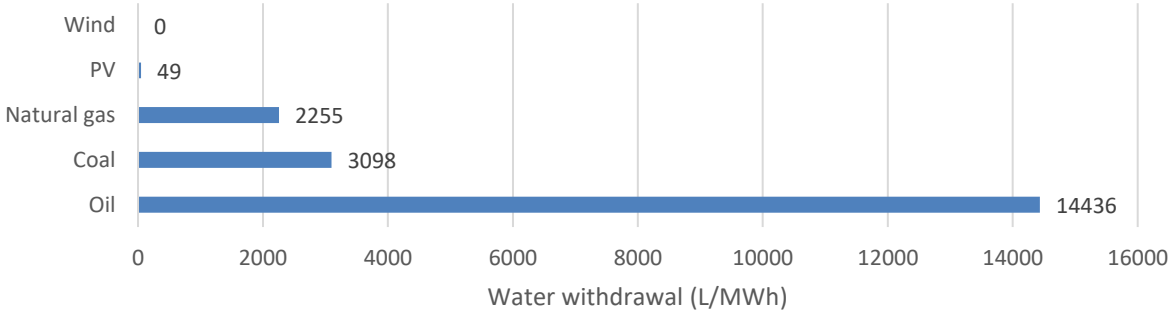

Figure 13. Water withdrawal for electricity generation from different sources.

Data on water intensity for hydrogen production processes were derived from the IRENA report "Water for hydrogen production" [64], which provides an analysis of the challenges of water use for hydrogen production. The data includes water withdrawals for grey hydrogen from SMR and coal gasification, blue hydrogen from CCUS technologies, and green hydrogen from electrolysis. Water withdrawal for blue hydrogen production from natural gas is examined both from SMR and Autothermal Reforming (ATR). Figure 14 displays the water withdrawal required to produce 1 kg of hydrogen, using both fossil fuels and renewable energy sources.

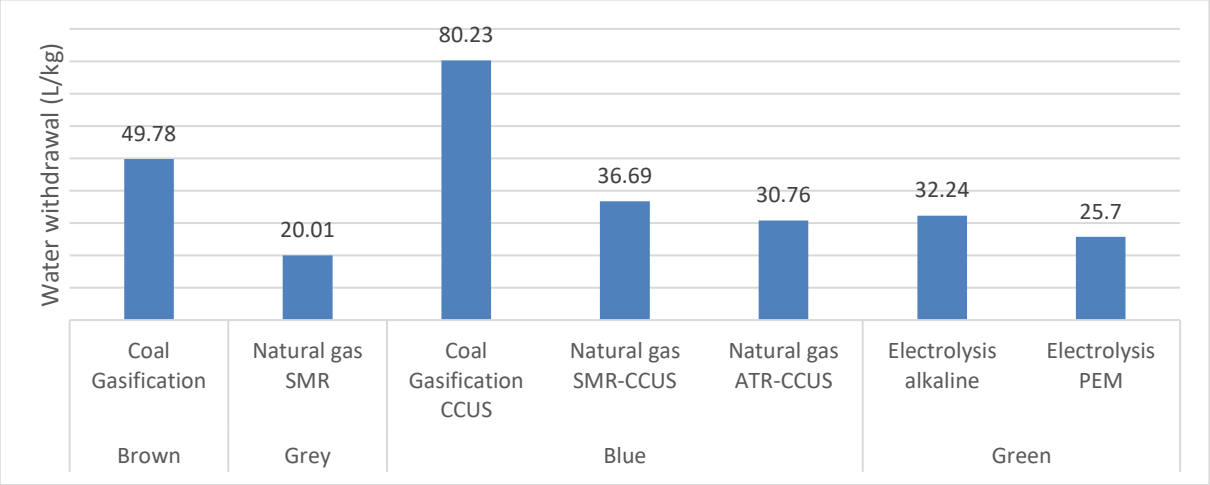

Figure 14. Water withdrawal for hydrogen production using different technologies.

5.2.3 Water withdrawal for green hydrogen from RES

The methodology presented herein aims to estimate the water withdrawal requirements for green hydrogen production using RES, to substitute fossil fuels in the energy sector.

The first step consists of calculating the amount of hydrogen required. To match the real electricity generation for each country by source, hydrogen generation requires high amounts of RES power. This is calculated by dividing the energy generation per source by the Power-to-Power (PtP) round-trip efficiency. The total mass of hydrogen produced is then calculated as the ratio between the electricity generation for each country by source and the specific consumption of the electrolyzer. Given the mass, water withdrawal for hydrogen generation is calculated considering the specific water withdrawal of the electrolyzer.

Additionally, the water withdrawal of the RES power plant for green hydrogen production is calculated as the product between the electricity generation for each country by source and the specific water requirements of either PV or wind. According to the data in Figure 13, the total water withdrawal of the wind power plant is equal to zero. Based on the energy generation data for each country, the water withdrawal requirements for fossil fuel technologies are calculated and reported in Figure 15.

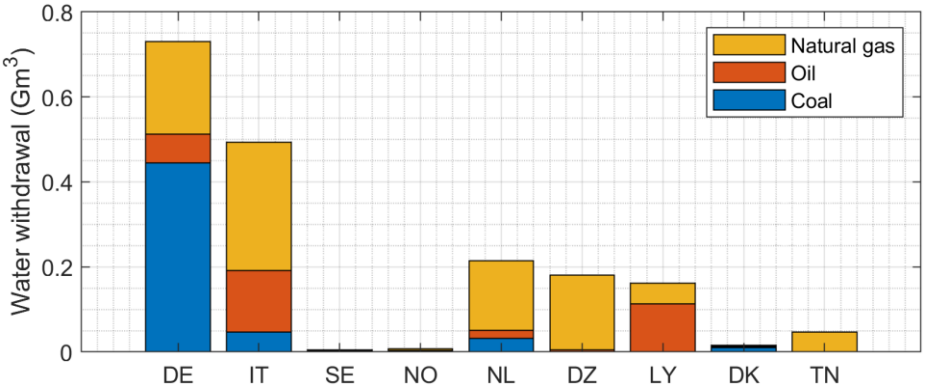

Figure 15. Water withdrawal for electricity generation from fossil fuel technologies.

5.2.4 Water withdrawal from RES and hydrogen in the energy sector

In this analysis, two water electrolysis technologies are studied and analyzed, i.e., alkaline and PEM electrolyzers. As demonstrated in Figure 14, they are characterized by very low water withdrawals, comparable with natural gas technologies. Hydrogen can be used for electricity generation in the Power-to-Power process [111], where electrical energy is converted to hydrogen, which is an energy carrier, and then reconverted back to electricity. This way, excess renewable energy can be used to generate hydrogen, later used for electricity production.

Various technologies allow for hydrogen use in electricity generation, mainly open-cycle gas turbines, combined-cycle, and Solid Oxide Fuel Cells (SOFC). In this analysis, SOFC technology was used for energy generation, exploiting its capability to produce water as a byproduct when combining hydrogen and oxygen, thereby contributing to further decreasing stress on freshwater resources.

The energy consumption of hydrogen production varies based on the technology and the efficiency of the process. However, the latest data shows that energy consumption for

PEM electrolyzers amounts to about 57 kWh/kg and for alkaline electrolyzers to about 52 kWh/kg, as of 2020 [112]. Given the lower heating value of 120 MJ/kg [113], the conversion efficiency of the PEM and alkaline electrolyzers is calculated to be about 58.5% and 64.1% respectively. For the efficiency of the SOFC, a conservative estimate of 55% is assumed [114].

Transitioning from fossil fuels in the energy sector necessitates increased capacity of RES hydrogen production. In this analysis, the effects on water withdrawal of increasing shares of RES and green hydrogen are analyzed. The analysis assesses the water usage across varying proportions of electricity generation directly from RES or using green hydrogen as energy storage, considering the entire PtP process to convert hydrogen back to electricity. Figure 16 shows the total water withdrawal for different shares of RES and hydrogen-based electricity generation as a replacement for fossil fuels, focusing on Germany. Figure 16 refers to the use of PV for energy production and a PEM electrolyzer for hydrogen generation. The results consistently reveal that, across all scenarios, the RES to H_2 share with comparable water withdrawal is about 97%, indicating that RES withdrawal is relatively low compared to electrolyzer water usage.

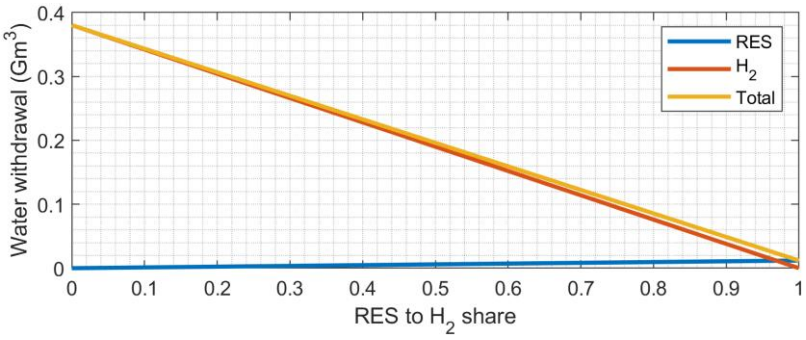

Figure 16. Water withdrawal for different shares of RES and hydrogen electricity generation.

5.2.5 Hydrogen water withdrawal in the energy sector

The following analysis adopts a very conservative approach, considering the worst-case scenario in terms of water withdrawal, i.e., RES to hydrogen share equal to zero, or in other words, all energy generation from fossil fuels is substituted by green hydrogen generated from RES. Figure 17 shows the results of the analysis, illustrating the water withdrawal of the entire PtP process using green hydrogen for electricity generation. Each graph displays the water withdrawal of current technologies for each considered country (in blue) and the potential withdrawal when substituting their energy production with a PtP process with hydrogen produced through PEM (a-c) and alkaline (d-f) electrolyzers, powered from PV and wind turbines. It can be observed that, in all cases, even for a complete substitution of fossil fuels, transitioning to green hydrogen leads to water savings.

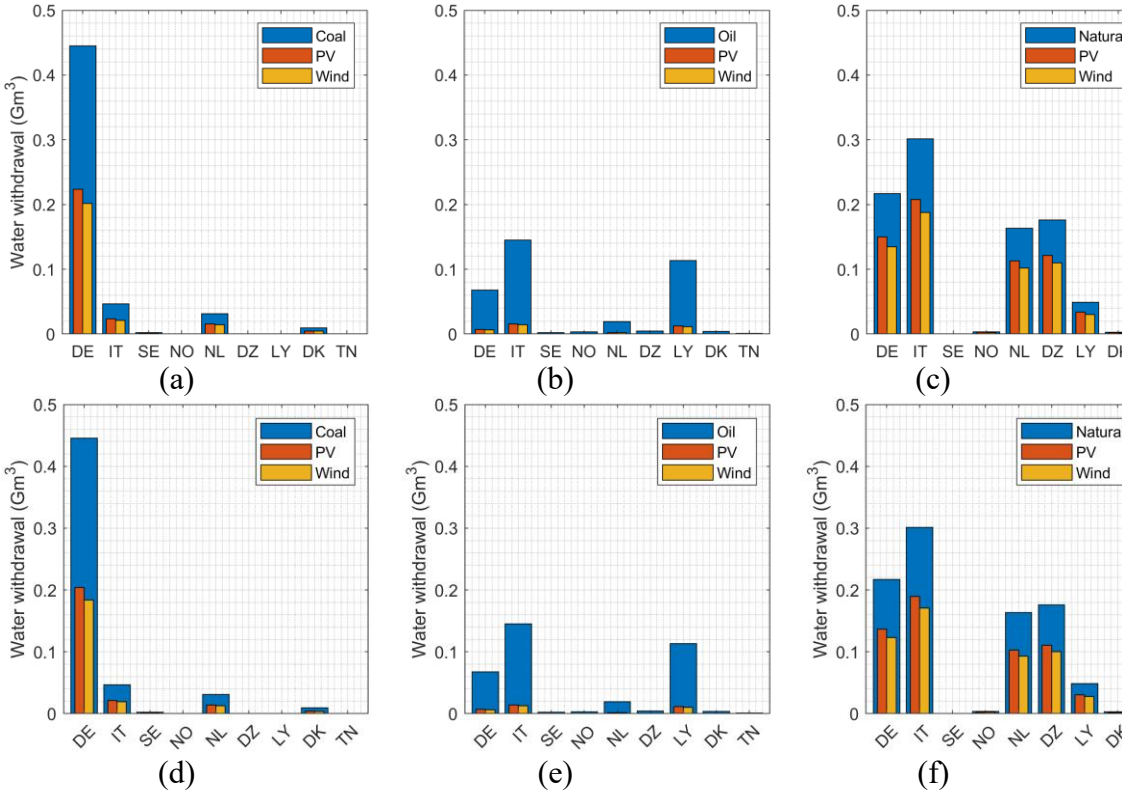

Figure 17. Water withdrawal substituting hydrogen from PEM electrolyzers to (a) coal (b) oil and (c) natural gas, and from alkaline electrolyzers to (d) coal (e) oil and (f) natural gas.

Table 5 shows the results of the analysis, expressed as a percentual reduction of water withdrawal when fossil fuel generation is substituted with PtP green hydrogen processes. A significant reduction in water withdrawal can be observed across all combinations. Comparing the results summarized in Table 5 with the absolute values in Figure 17, even though oil shows the biggest percentage reductions, the total water withdrawal is low when compared to natural gas and coal. In summary, regardless of the combination of electrolysis technology and power source, a considerable reduction in water withdrawal percentage can be achieved by substituting green hydrogen for fossil fuels in the energy sector.

Table 5: Water withdrawal reduction substituting energy generation from fossil fuels with PtP green hydrogen processes.

Electrolyzer technology	RES type	Primary energy source		
		Coal (%)	Oil (%)	Natural gas (%)
PEM	PV	-49.83	-89.23	-31.08
	Wind	-54.75	-90.29	-37.84
Alkaline	PV	-54.23	-90.18	-37.12
	Wind	-58.72	-91.14	-43.29

5.2.6 Seawater electrolysis for green hydrogen production

Electrochemical splitting of seawater appears to be a promising solution to reduce water stress in regions with limited access to freshwater resources. This section discusses the energy and water implications of seawater electrolysis, comparing direct and indirect technologies.

The previous analysis, conducted over 9 different countries, proved that in some regions, especially in northern Europe, increasing RES penetration can lead to lower water stress. However, other countries face tougher challenges because of critical water stress levels and limited access to freshwater. Although all the countries considered have direct access to seawater, only some of them employ purification systems for freshwater production. Table 6 shows the total water desalinated per year.

Table 6. Annual desalinated water production in the considered countries [115].

	DZ	DK	DE	IT	LY	NL	NO	SE	TN
Desalinated water (Mm^3)	631.0	0.0	0.0	200.0	70.0	0.0	0.1	1.0	43.0

As previously mentioned, seawater electrolysis can be achieved with ISE or DSE technologies. ISE requires, as a first step, seawater desalination, and treatment, which, at an industrial scale, is performed with reverse osmosis plants. The energy consumption of these systems has decreased significantly over the past few years to about 2.5 kWh/m^3. DSE instead allows for the elimination of the need for water treatment, and its specific energy consumption is about 53 kWh/kg.

Applying the same procedure discussed earlier, water withdrawal for the two technologies was assessed. DSE performs similarly to conventional electrolyzers, as shown in Figure 18, where the total annual water withdrawal is calculated considering the specific energy consumption using both PV and wind sources. By applying the same procedure, it is calculated that for ISE systems, the seawater purification step increases energy consumption by only 0.1% for both PEM and alkaline electrolyzers, compared to using freshwater sources. However, the comparison between ISE and DSE should consider not only the energy consumption increase of the SWRO, but instead it should consider the entire PtP process. Results show that the ISE system, using SWRO for seawater treatment, requires about 1.8% more energy than DSE, using both PV and wind sources.

In summary, due to the high energy consumption of the electrolysis process compared to SWRO, ISE and DSE offer comparable performance in terms of energy consumption. Their application should be intended mainly for arid and water-stressed regions or where access to freshwater is limited. In these areas, however, ISE could provide services to the community. In fact, by oversizing the seawater treatment plant, purified water can be produced, further reducing stress on freshwater resources.

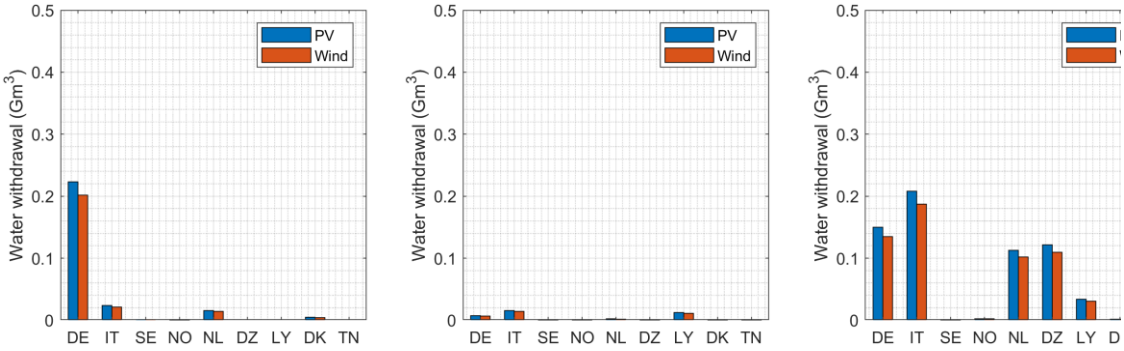

(a) (b) (c)

Figure 18. Water withdrawal for DSE from RES, substituting (a) coal, (b) oil and (c) natural gas with green hydrogen.

5.3 Hydrogen integration in Compressed Air Energy Storage systems

Globally, the increasing share of renewables, prominently driven by intermittent sources such as solar and wind power, poses significant challenges to the reliability of current electrical infrastructures, leading to the adoption of extreme measures such as generation curtailment to preserve grid security. Within this framework, it is essential to develop energy storage systems that contribute to reinforcing the flexibility and security of power grids while simultaneously reducing the share of generation curtailment. Therefore, an integrated storage solution was studied, including green hydrogen production and CAES for mitigating the curtailment of renewable energy.

Current research interest is primarily focused on energy-environmental assessments, and in some cases, on economic analysis of hybrid or integrated CAES systems. For example, a recent study on an integrated CAES configuration was developed by Assareh and Ghafouri [116], which proposed a cogeneration system (electricity, heating, and cooling) based on CAES, solar, and geothermal energy. The system comprises a solar field, a gas turbine, an absorption chiller, and a CAES. The performance of the plant was optimized for exergy efficiency maximization and cost rate minimization, calculating optimal values of 29.25% and 714.25 $/h respectively, in 5 regions in Iran considered as case studies. Also, Xue et al. [117] proposed a combined cycle system using an electrolyzer and a CAES system to store energy, to later be released, generating electricity using a solid oxide fuel cell, a gas turbine, and a steam turbine: the system can reach an efficiency of 39.45%. In the field of hybrid solutions, Bartela et al. [118] studied a hybrid CAES system composed of a hydrogen production system, a methanation unit, a CAES, an oxy-combustion section, and a drying system. Another example of system integration is developed by Alirahmi et al. [119] and regards a solar heliostat-driven combined cycle coupled with a regenerative hydrogen-fed D-CAES system, designed for a thermal-integrated application. In this system, excess electricity from the combined plant is used to power the compression train of the CAES and to produce hydrogen in a PEM electrolyzer. Thermal energy, which is recovered from the compression train, heats up the water for domestic applications and for the electrolyzer. A similar system, involving

a PEM electrolyzer coupled to a CAES, was proposed by Zhao et al. [120], who studied a hydrogen-fueled D-CAES configuration, composed of a gas turbine thermally integrated with a fuel cell. The system components work in combination to smooth the RES power fluctuations and provide hot water and power to a community. The research interest in coupling hydrogen with CAES systems is confirmed by Cao et al. [121], who proposed a hydrogen-fueled CAES, where excess RES energy is used to drive the air compressors and generate hydrogen. The storage system of this layout comprises a high-pressure air storage reservoir, a hydrogen storage tank, and a two-tank thermal energy storage of water. The system of Cao et al. is characterized by a round-trip efficiency of 65.11% and an exergy efficiency of 79.23%. The system efficiency could be further improved by means of higher combustion temperatures and more performing electrolyzers.

Currently, no study assesses the performance of CAES systems based on the flexibility services they can provide to electrical grids. Furthermore, although several studies investigated the integration of hydrogen in the combustion section, none of them considered the optimization of the size of the hydrogen production and storage sections. In addition, very few studies considered the dynamic performance of the CAES components, which mainly operate in off-design conditions, such as the compressor, this being crucial for VRES-powered plants. In this framework, a PV power plant integrated with a hydrogen-fueled D-CAES (PV-H2-CAES) system was specifically designed to improve the flexibility of the electrical grids. In fact, the integrated PV-H2-CAES system is designed to mitigate the variability in VRES feed-ins, reduce curtailments, supply inertial power, and help address high ramp rates and ramping ranges in a flexibility service supply that considers dispatch possibility contingent on grid conditions. In particular, differently to most recent studies on CAES solutions, where all the energy produced is considered fully dispatchable [116] or where the analyses are carried out only at nominal conditions [121], a performance evaluation methodology that considers a real one-year-long grid scenario, characterized by significant and frequent dispatchability issues, was introduced. Moreover, the size of the main plant components is assessed by taking into account the dynamic behavior of the compressor train, to maximize the flexibility services and evaluate the yearly and seasonal performance of an optimized configuration. The energy requirements of both the air compression and hydrogen production sections are thoroughly analyzed under various scenarios, assessing the performance of the integrated system, always with the assumption of utilizing the excess energy production of the PV power plant.

5.3.1 Integrated PV-H2-CAES system configuration

A schematic configuration of the integrated PV-H2-CAES plant is reported in Figure 19. It originated from a downscaled version of the McIntosh CAES plant, which was already demonstrated to be suited for leveling variable wind power [122], with the key difference that hydrogen replaces natural gas as fuel.

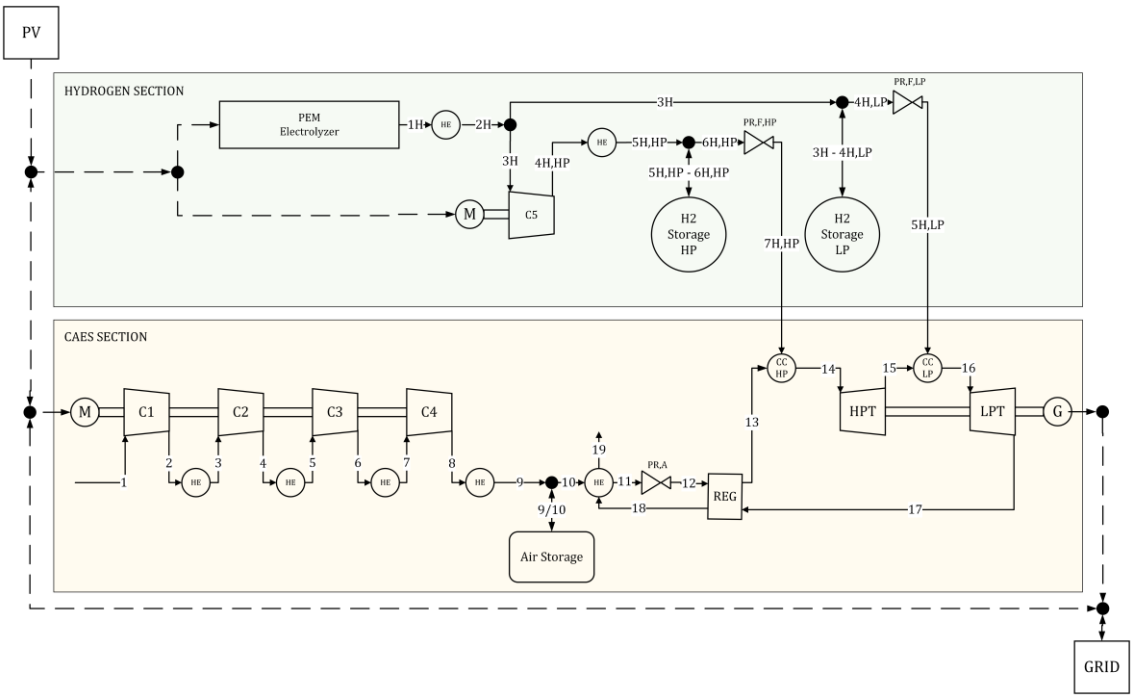

Figure 19. Schematic configuration of the integrated PV-H2-CAES system.

The charge components of the CAES section of the plant include four inter-refrigerated multistage centrifugal compressors (C), an aftercooler, and an Air Storage system. The discharge components include a high-pressure turbine (HPT) and a low-pressure turbine (LPT), each with a dedicated combustion chamber (CC). In order to operate the expansion train in a "constant pressure mode" [123] as for the McIntosh CAES plant, the air pressure during discharge is controlled by a pressure regulator (PR). A regenerator (REG) and an additional heat exchanger allow for the recovery of part of the thermal energy of the exhaust gases. A green hydrogen production and storage section is added to the plant layout and is based on a PEM electrolyzer for hydrogen generation, which is stored in two dedicated (HP and LP) hydrogen storage tanks. The Balance of Plant is completed by a hydrogen compressor, dedicated heat exchangers, pressure regulators, and other minor components. In this integrated PV-H2-CAES plant, the electric power for air compression and hydrogen production comes from a dedicated PV system. However, it is important to note that the flexibility of this integrated configuration also enables it to be powered by other VRES power plants and by the grid, either entirely or partially, allowing it to offer demand-response services. Among the existing technologies for hydrogen production through water electrolysis, a PEM electrolyzer is selected, because of its wide power range, low operating temperature [124] and rapid response time [21], which make it the most suitable technology for VRES integration.

The main energy flows of the integrated PV-H2-CAES plant are shown in Figure 20, where E_{PV} represents the energy that could potentially be produced by the PV system without any generation curtailment; therefore, E_{PV} includes a share of energy that is actually generated ($E_{PV,H2-\mathrm{CAES}} + E_{PV,G}$) and a share of energy that could potentially be

generated if not curtailed ($E_{PV,CURT}$). The energy actually generated by the PV system can be directly fed in the grid ($E_{PV,G}$) or used to charge the CAES system ($E_{PV,H2-CAES}$). When the charge phase occurs, the energy is used for compressing air ($E_{PV,C}$) and producing hydrogen ($E_{PV,PEM}$), which are stored for a later use. During the discharge phase, the stored energy is used to generate electricity ($E_{T,G}$). Therefore, the overall energy delivered to the grid (E_G) is the sum of $E_{PV,G}$ and $E_{T,G}$.

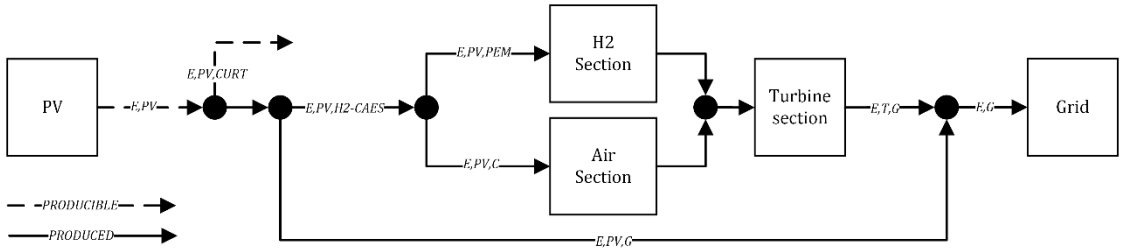

Figure 20. Main energy flows of the integrated PV-H2-CAES system.

5.3.2 Energy management strategy

The EMS of the integrated PV-H2-CAES system is conceived to integrate the PV energy production into electrical grids already characterized by a high VRES penetration, where any additional increase in VRES power would result in further deterioration of flexibility levels (uncertainty in production, extended ramping-ranges, high ramp-rates) and, lastly, generation curtailment.

With reference to the CAISO duck curve on April 16, 2023, Figure 21 shows the daily PV potential energy production (E_{PV}) and the corresponding energy curtailment ($E_{PV,CURT}$). Five periods can be identified, herein denoted by the letters α to ε, where α and ε represent the dark hours and β, γ, δ the daylight hours, when PV generation occurs. During early morning (β) and late evening (δ) hours, all the generated PV energy is consumed. Conversely, during the central daylight hours (γ), the PV production exceeds the demand to the extent that the surplus energy cannot be traded with neighboring countries and must be curtailed. The generation curtailment occurs because of the reached minimum limit in the net load curve, which cannot be reduced to zero due to the technical minimum and the response times of those power facilities that are crucial for ensuring grid safety. Given this, it is evident that for such a grid, it would be desirable to minimize PV curtailment by storing the excess production for subsequent use. New PV installations would lead to an increase in the generation curtailment shares. Therefore, the EMS proposed for the PV-H2-CAES system is conceived to enhance the grid flexibility, thus enabling the installation of new PV capacity.

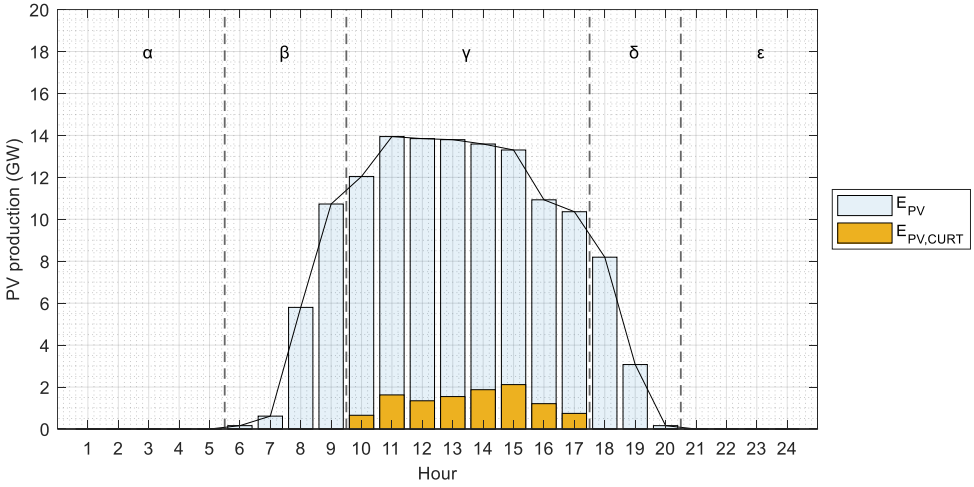

Figure 21. Daily PV curtailment in the CAISO grid on April 16, 2023.

The PV-H2-CAES system can directly feed the PV power into the grid or use it for charging the energy storage sections. From an efficiency point of view, direct feed-in is the preferred option. However, with reference to the five periods experienced in electrical grids with high shares of VRES plants, the EMS applied to the PV-H2-CAES plant considers that:

- during the early morning (β) and late evening (δ) hours, the PV power is directly fed to the grid;
- during the generation curtailment periods (γ), the PV power is used to power both the air compressor and the PEM electrolyzer, prioritizing the air compressor;
- during dark hours (α and ε), the CAES is discharged.

The EMS of the PV-H2-CAES systems is better explained in Figure 22. During early morning (β) and late evening (δ) hours, the considered grid has the capacity to dispatch additional PV power (no curtailments), and therefore, the PV power can be directly fed into the grid, resulting in valuable support for ramp rate reduction. Although it is not the case for the EMS considered, in grids without the capacity to dispatch additional VRES power, the PV power can be used to charge the CAES section even during β and δ periods.

During the generation curtailment periods (γ), since any additional PV feed-in would be curtailed, the PV power is used to charge the CAES section. This way, the PV generation is not curtailed, nor does it worsen the flexibility of the grid. In more detail, during the charge phase, the PV power is used to power both the air compressor and the PEM electrolyzer. The electrolyzer is powered residually compared to the compressor due to its greater load modulation capability, making it excellent for performing peak shaving of PV plants (smoothing of uncertainty in production). In case of full storage or maximum power capacity of the compressor and electrolyzer, any excess PV power is considered curtailed.

Finally, the discharge of the CAES section during dark hours (α and ε), allows for enhancing the share of energy produced during dark hours from RES, providing inertia, and increasing the energy independence of the grid. However, if the grid were to require additional power during other moments of the day, the flexibility of the system would allow for a discharge phase, operated rapidly thanks to the brief startup time of a conventional gas turbine.

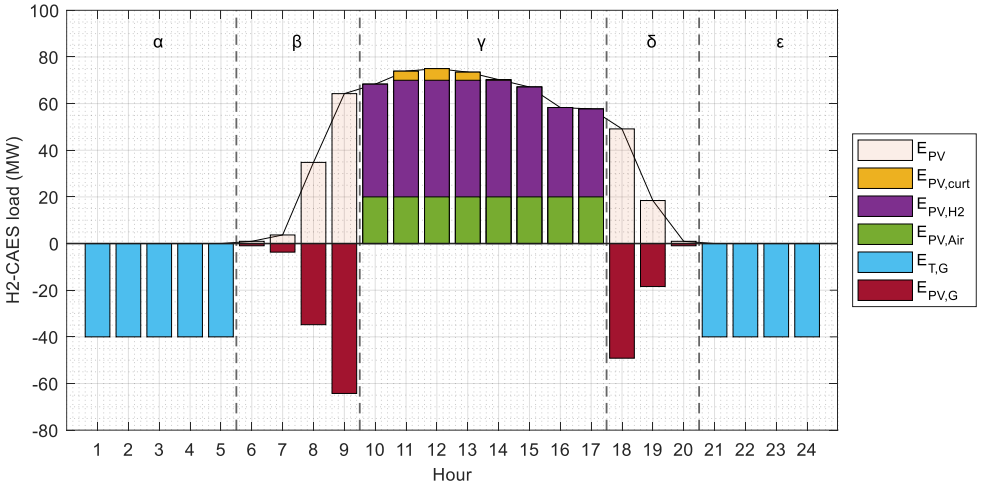

Figure 22. Energy management strategy of the PV-H2-CAES system.

5.3.3 Parameters

Hourly weather data are obtained by Meteonorm software version 7.2 [33] and refer to a site located in California. The main data and assumptions of the PV system are reported in Table 7.

Table 7. PV system design parameters.

Parameter	Value	Unit
Nominal power of a PV module [34]	360	Wp
Tilt angle	30	°
Azimuth angle	0	°
Derating factor (f_{PV})	0.90	
Nominal inverter efficiency (η_{INV})	0.978	
STC conversion efficiency of a module ($\eta_{PV,STC}$)	0.221	
STC cell temperature (T_{STC})	25	°C
Net Operative Cell Temperature ($NOCT$)	41.5	°C
Ambient temperature at NOCT conditions ($T_{AMB,NOCT}$)	20	°C
Global Solar Irradiation at NOCT conditions (GI_{NOCT})	800	W/m^2
Solar transmittance and absorptance (τ_α)	0.9	
Temperature correction factor (θ)	-0.29·10^{-2}	1/K

The PEM design parameters assumed in this analysis are summarized in Table 8.

Table 8. PEM electrolyzer design parameters.

Parameter	Value	Unit
Nominal power [36]	2	MW
Transfer coefficient α_{PEM} [35]	0.34	
Constant coefficient β_{PEM} [35]	0.06	
Membrane thickness δ_m [35]	0.04	cm
Humidification factor λ_E [35]	17	
Membrane cross-sectional area A [35]	100	cm^2
Faraday constant F	96485.33	$\frac{C}{mol}$
Diffusion limit current density i_{lim} [35]	1.55	$\frac{A}{cm^2}$
Exchange current density i_0 [35]	0.0013	$\frac{A}{cm^2}$
Pump and heater energy consumption*	0.3	%
Operating pressure [36]	30	
Operating temperature [36]	40	
Specific H_2 production	17	

*Referred to the total energy required by the electrolyzer

5.3.4 Compression and expansion trains

The air compressor train comprises four multistage centrifugal compressors. The choice of centrifugal compressors is made according to Baljé [37] because of the low mass flow rate and the high-pressure ratio. The mathematical model is developed based on the Casey-Robinson method [38], used to estimate the design and off-design performance of compressors. At the outlet side of each compressor, an aftercooler is used to reduce the temperature of the compressed air, thus lowering the total power required by the compression train. The compressor is designed for a maximum pressure of 70 bar.

The expansion train includes two turbines, two combustion chambers, and a regenerator. The system is assumed to operate in a steady-state condition and with constant isentropic efficiencies for the turbines. To operate the expansion train in constant pressure mode, as for the McIntosh CAES plant, pressure regulators (PR) are modeled as adiabatic processes. The heat exchanger before the PR prevents the air stream temperature from dropping below the freezing point.

5.3.5 Storage units

The minimum pressure for the air storage volume is determined by the operating range of the air compressors. The minimum pressure for each of the hydrogen storage tanks is instead assumed according to the operating pressure of the combustion chambers.

5.3.6 Performance indicators

The performance of the integrated PV-H2-CAES system is evaluated by means of the three performance indicators described in the present section. The performance indicators measure the system efficiency, the system capacity to minimize PV curtailment, and the capacity factor of the plant during dark hours.

The system efficiency ($\eta_{\mathrm{PV-H_2-CAES}}$) measures the overall efficiency of the integrated system in delivering PV energy to the grid, either directly or through the CAES process:

$$\eta_{\mathrm{PV-H_2-CAES}} = \frac{E_{PV,G} + E_{T,G}}{E_{PV}} \tag{5.1}$$

where $E_{PV,G}$ represents the energy directly fed into the grid, $E_{T,G}$ the energy generated during the CAES discharge phase and E_{PV} the PV potential energy production.

The curtailment of PV energy (PV_{CURT}) quantifies the ratio of PV energy that is curtailed due to reaching the maximum storage capacity and the impossibility of further dispatch (neither stored nor directly fed into the grid) over the potential energy production of the PV system:

$$PV_{CURT} = \frac{E_{PV,CURT}}{E_{PV}} \tag{5.2}$$

The capacity factor during dark hours (CF_{DH}) is an evolution of the traditional capacity factor and measures the number of CAES equivalent generation hours over the total dark hours:

$$CF_{DH} = \frac{\dot{E}_{T,G} \cdot EOH_T}{\dot{E}_{T,G} \cdot DH} = \frac{EOH_T}{DH} \tag{5.3}$$

where EOH_T represents the Equivalent Operating Hours of the CAES section (during discharge) and DH is the number of dark hours over a given period. CF_{DH} can also be intended as a flexibility indicator which assesses the capacity of the system to assist the grid through feed-ins of inertial energy from RES during periods of PV absence.

5.3.7 PV-H2-CAES plant sensitivity analysis

A sensitivity analysis is carried out by varying four design parameters: the rated power of the PV plant, the rated power of the compressor train, the rated power of the electrolyzer, and the storage capacity. The rated power of the PV plant ($\dot{E}_{PV}$) ranges between 0.5 to 2 times the turbine power ($\dot{E}_T$), while, considering that the compressor and the electrolyzer are powered by the PV system, their sizes ($\dot{E}_C$ and $\dot{E}_{PEM}$) vary independently in a range between 0.1 to 1 time the size of the PV plant. The storage capacity, expressed in terms of the nominal discharge duration of the CAES system at

full power, is considered within the range of 7-13 hours: this range is determined considering the cumulative frequency of consecutive dark hours that occurred in California in 2022 and reported in Figure 23. It can be observed that a storage capacity of 13 hours is potentially sufficient to cover nearly all (99.5%) of the consecutive dark hours of the year. The lower storage capacity (7 hours) is instead chosen as the nearest integer to the cumulative frequency value at about 20%.

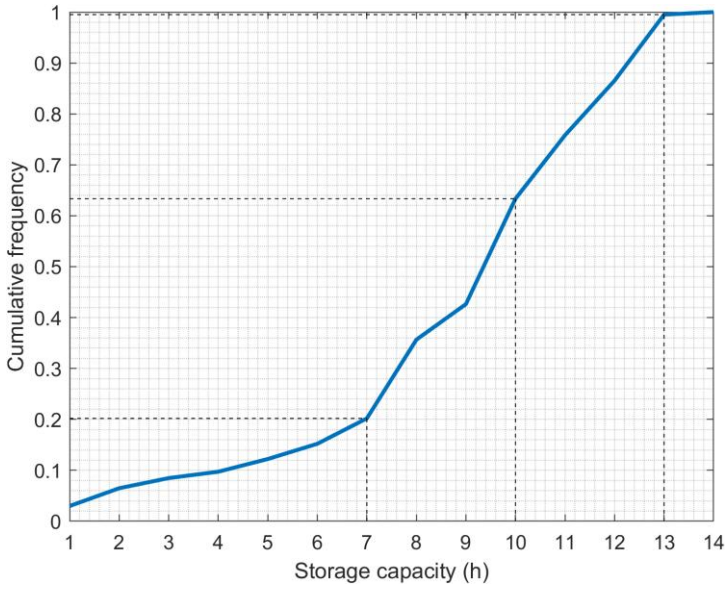

Figure 23. Cumulative frequency of consecutive dark hours in California in 2022.

The main design parameters of the integrated PV-H2-CAES plant are summarized in Table 9.

Table 9. Integrated PV-H2-CAES plant design parameters.

Parameter	Value	Unit
Turboexpander power $\dot{E}_T$	42	MW
Photovoltaic power $\dot{E}_{PV}$	$(0.5 - 2) \cdot \dot{E}_T$	MW
Compressor power $\dot{E}_C$	$(0.1 - 1) \cdot \dot{E}_{PV}$	MW
Electrolyzer power $\dot{E}_{PEM}$	$(0.1 - 1) \cdot \dot{E}_{PV}$	MW
Storage capacity t_{dch}	$7 - 13$	hours
Air Storage capacity	$(4.8 - 8.9) \cdot 10^4$	m^3
Air storage pressure range	$46 - 75$	bar
HP H_2 Storage capacity	$(1.5 - 2.8) \cdot 10^3$	m^3
HP H_2 storage pressure range	$46 - 75$	bar
LP H_2 Storage capacity	$(6.4 - 1.2) \cdot 10^3$	m^3
LP H_2 storage pressure range	$16 - 30$	bar

5.3.8 PV-H2-CAES system efficiency

Figure 24 shows the variations of η_{PV-H_2-CAES} across the four design parameters ($\dot{E}_{PV}, \dot{E}_C, \dot{E}_{PEM}, t_{dch}$). Each subplot displays the system efficiency while considering variations in the compression train and the electrolyzer powers for a given value of $\dot{E}_{PV}$ and t_{dch}. The analysis is carried out over a wide range of PV power and storage capacity values, and the results are presented for three values of $\dot{E}_{PV}/\dot{E}_T$ and three values of t_{dch}.

For the design parameters here considered, the system efficiency is always included in the range of $0.45-0.62$. Independent of $\dot{E}_{PV}$ and t_{dch}, the highest η_{PV-H_2-CAES} values are observed for $\dot{E}_{PEM}/\dot{E}_{PV}$ within the range of $0.7-0.9$ and for $\dot{E}_C/\dot{E}_{PV}$ within the range of $0.20-0.25$. Solutions minimizing the sizes of the electrolyzer and of the compressor train are preferable when efficiencies are equivalent. Lower $\dot{E}_{PV}/\dot{E}_T$ values lead to higher efficiencies at the expense of lower capacity factors, as reported in the following subsections.

For a given storage capacity (t_{dch}), high PV power values lead to lower system efficiencies. In fact, high amounts of PV generation are lost due to limitations in dispatchability and CAES storage capacity. As a result, the share of curtailed energy increases and, consequently, the system efficiency decreases.

Focusing on the area with the highest system efficiencies (orange/red colored areas), for a given $\dot{E}_{PV}/\dot{E}_T$, increasing t_{dch} from 7h to 10h results in a system efficiency increment, but no further relevant improvements are observed for greater storage capacities. This implies that a 10-hour storage capacity is adequate to maximize the PV energy shift towards dark hours. From a perspective that combines economic and technical aspects, a smaller storage capacity under comparable conditions is certainly preferable.

Finally, all the graphs of Figure 24 show the influence of $\dot{E}_{PEM}/\dot{E}_{PV}$ and $\dot{E}_C/\dot{E}_{PV}$ on system efficiency. Increasing the power of the PEM electrolyzer improves the system efficiency up to a plateau, while the growth of the compression train power results in raising the system efficiency to a maximum before declining. In fact, while the electrolyzer is a modular system with a broad power range, capable of managing a wide range of fluctuating power inputs, the compressor operating power range is limited, and it is related to the air cavern pressure at any given time. As a result, not enough power is averagely provided by the PV plant for excessively large-sized compression trains, resulting in the curtailment of an increasing share of the PV power. Essentially, for compressor sizes significantly larger than the PV size, it would be necessary to substantially increase the size of the PEM electrolyzer to achieve results like those obtained with much smaller compressor and electrolyzer sizes.

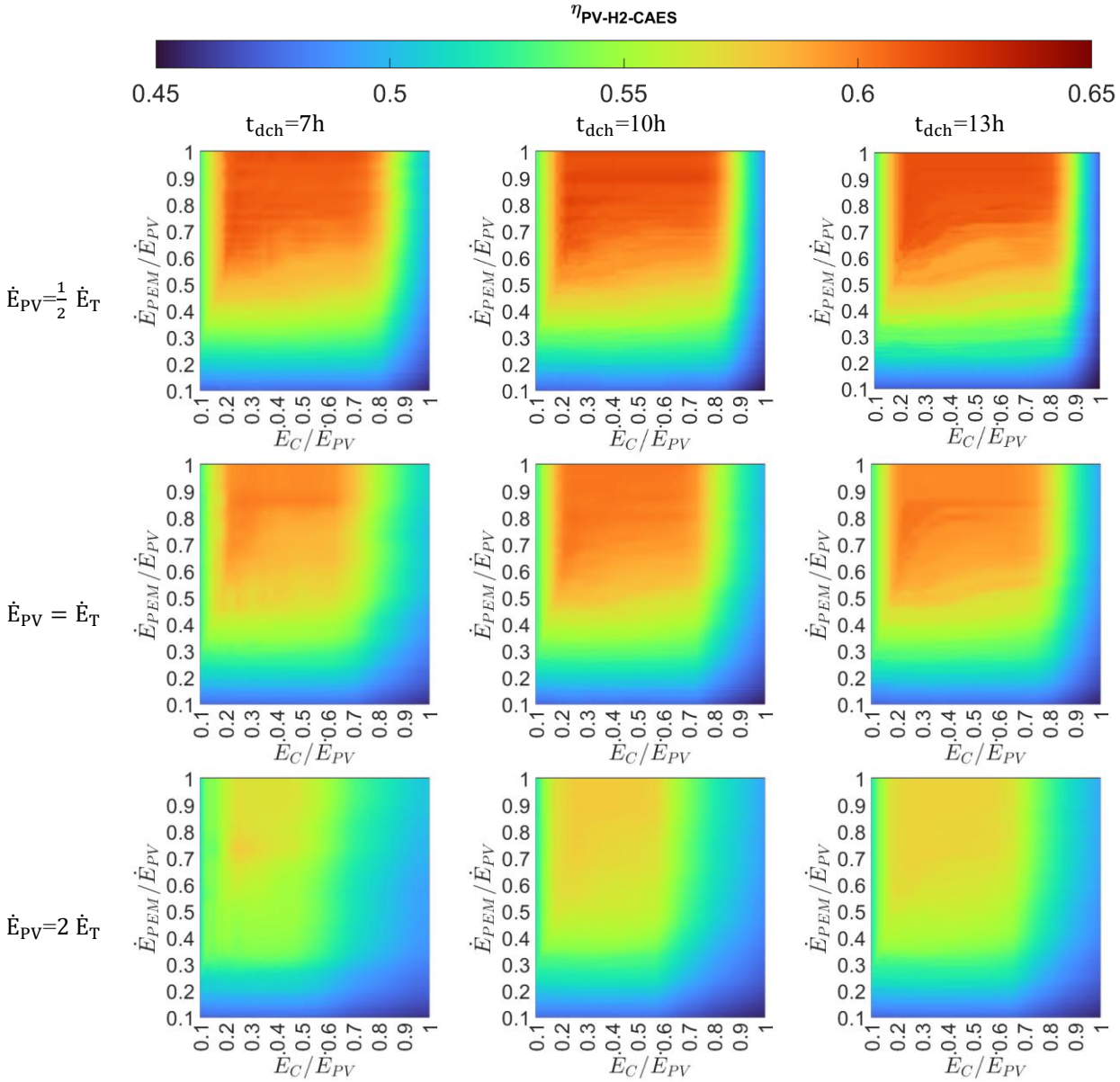

Figure 24. η_{PV-H_2-CAES} as a function of the PV-H2-CAES design parameters.

5.3.9 PV-H2-CAES system photovoltaic curtailment

Figure 25 shows the variations of PV_{CURT} across the four design parameters. The curtailment of PV energy is included in the range of $0.04-0.50$ and increases with $\dot{E}_{PV}$. In particular, for each configuration, the minimum curtailment rises from 4% for $\dot{E}_{PV} = 0.5\,\dot{E}_T$ up to 15% for $\dot{E}_{PV}= 2\dot{E}_T$, with an intermediate value of 8% for $\dot{E}_{PV} = \dot{E}_T$. Independently of $\dot{E}_{PV}$ and t_{dch}, lowest PV_{CURT} values are found within a range of $\dot{E}_{PEM}/\dot{E}_{PV}$ between 0.7 and 0.9, and for $\dot{E}_C/\dot{E}_{PV}$ between 0.20 and 0.25. As expected, these ranges are the same, which leads to the highest system efficiencies.

For a given t_{dch}, increasing the power of the PV plant leads to greater curtailment values due to the growing amount of PV energy that cannot be fed into the grid, and because the CAES is unable to store it. As for the system efficiency, for a given value of $\dot{E}_{PV}/\dot{E}_T$, storage capacities exceeding 10 hours have a negligible effect on PV curtailment.

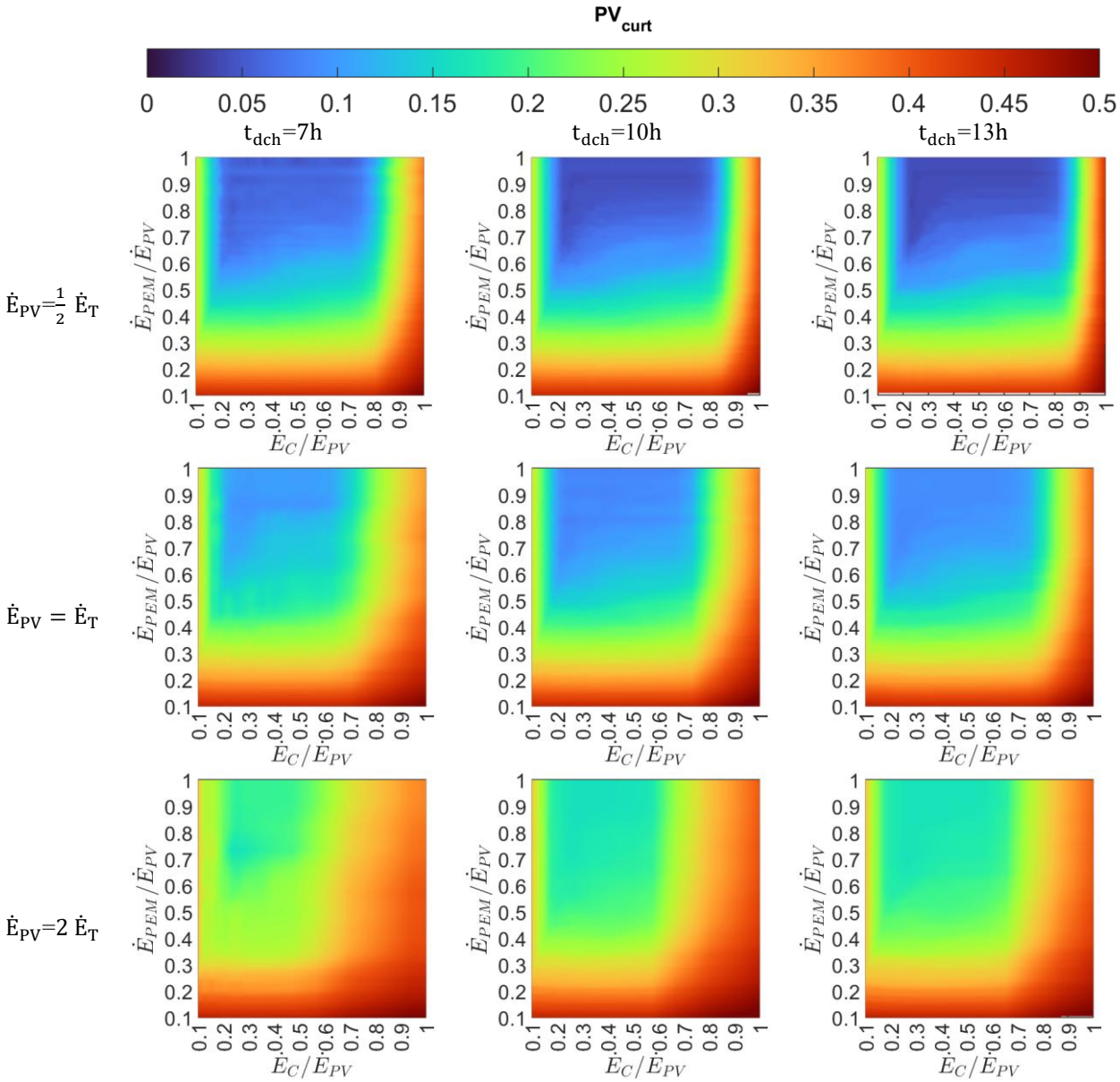

Figure 25. PV_{curt} as a function of the PV-H2-CAES design parameters

5.3.10 PV-H2-CAES system capacity factor during dark hours

Figure 26 shows the capacity factor CF_{DH} across the four design parameters. Overall, CF_{DH} varies between 0.02 and 0.21. Maximum values of CF_{DH} are 0.06, 0.12 and 0.21 and are achieved for $\dot{E}_{PV} = 0.5\dot{E}_T$, $\dot{E}_{PV} = \dot{E}_T$ and $\dot{E}_{PV} = 2\dot{E}_T$, respectively. As observed for the other performance indicators, the highest CF_{DH} values are found for $\dot{E}_{PEM}/\dot{E}_{PV}$ within the range $0.7-0.9$ and for $\dot{E}_C/\dot{E}_{PV}$ within the range $0.20-0.25$, independently of $\dot{E}_{PV}$ and t_{dch}. For a given t_{dch}, higher PV power leads to higher capacity factors. In fact, as more energy is made available to the CAES system, the amount of energy shifted to the dark hours increases as well. Given that the turbine power is kept constant in this analysis, increasing the PV size increases CF_{DH}. This means that the system is capable of producing electrical energy for 6%, 12%, and 21% of the dark hours throughout the year. Consistent with the trends described in the previous sections, for a given $\dot{E}_{PV}/\dot{E}_T$,

increasing the storage capacity over 10 h does not lead to significant improvements in CF_{DH}.

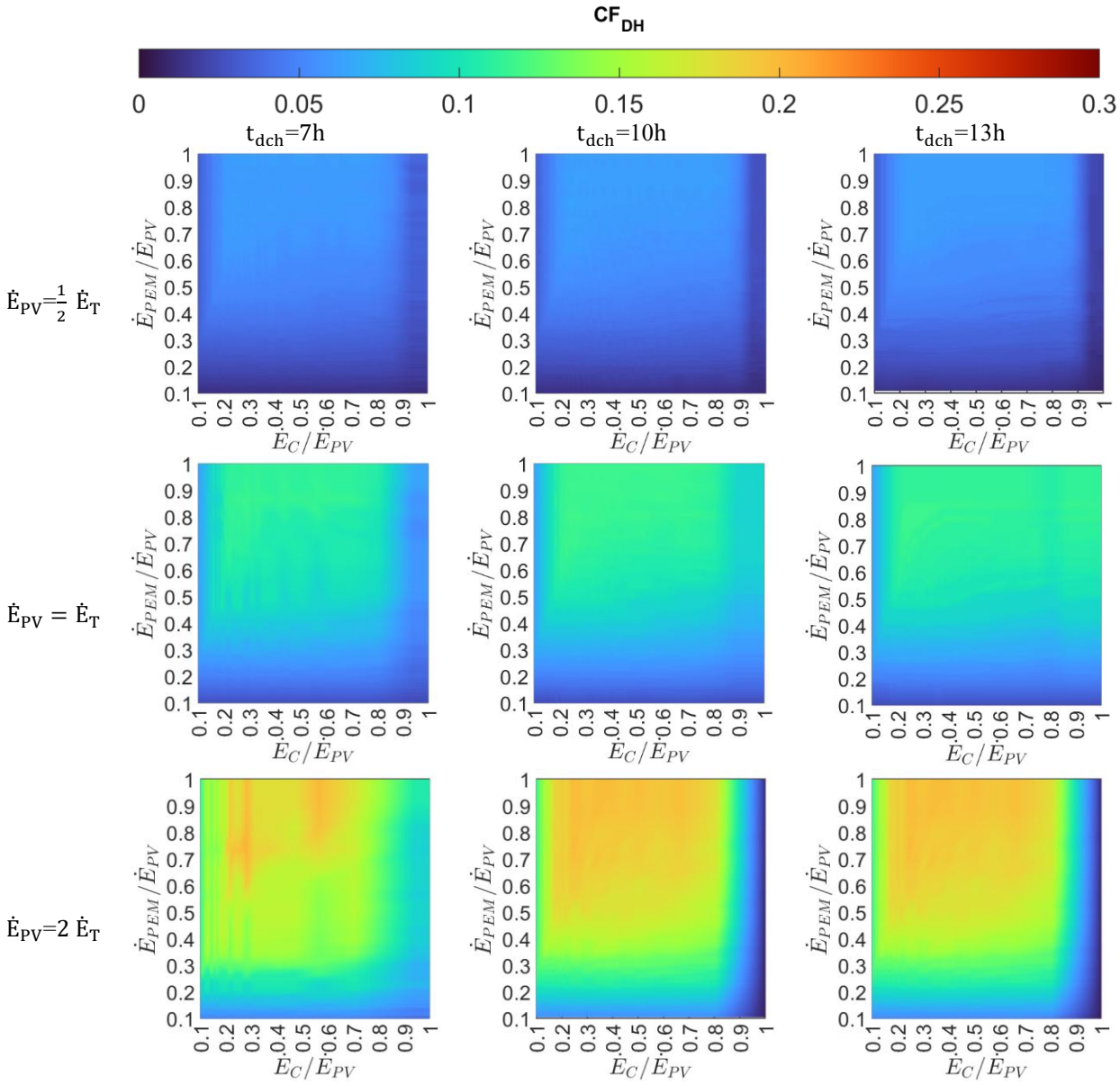

Figure 26. CF_{DH} as a function of the PV-H2-CAES design parameters.

5.3.11 PV-H2-CAES optimal performance

The analyses of the three performance indicators reported above allow to identify a combination of design parameters ($\dot{E}_{PEM}, \dot{E}_C, t_{dch}$) that maximizes the overall yearly performance of the plant, for each considered $\dot{E}_{PV}$. Each combination of parameters and the relative system performance are reported in Table 10.

Table 10. Design parameters for maximizing the PV-H2-CAES performance.

Parameter			
$\dot{E}_{PV}$ (MW)	$\frac{1}{2}\ \dot{E}_T$ (21)	1 $\dot{E}_T$ (42)	2 $\dot{E}_T$ (84)
t_{dch} (h)	9	10	7
$\dot{E}_{PEM}$ (MW)	0.80 $\dot{E}_{PV}$ (16.8)	0.81 $\dot{E}_{PV}$ (34.0)	0.73 $\dot{E}_{PV}$ (61.3)
$\dot{E}_C$ (MW)	0.24 $\dot{E}_{PV}$ (5.0)	0.24 $\dot{E}_{PV}$ (10.1)	0.28 $\dot{E}_{PV}$ (23.5)
$\eta_{\mathrm{PV-H_2-CAES}}$ (-)	0.619	0.606	0.581
$\mathrm{PV_{CURT}}$ (-)	0.035	0.075	0.148
$\mathrm{CF_{DH}}$ (-)	0.064	0.119	0.202
H_2-CAES round-trip efficiency η_{RT}* (-)	0.345	0.345	0.345
Air storage volume (m^3)	$6.2 \cdot 10^4$	$6.9 \cdot 10^4$	$4.8 \cdot 10^4$
HP H_2 storage volume (m^3)	$1.9 \cdot 10^3$	$2.1 \cdot 10^3$	$1.5 \cdot 10^3$
LP H_2 storage volume (m^3)	$8.2 \cdot 10^2$	$9.2 \cdot 10^3$	$6.4 \cdot 10^3$
E_{PV} (GWh/y)	55.08	158.63	220.41
$E_{PV,G}$ (GWh/y)	24.20	96.86	96.86
$E_{PV,CURT}$ (GWh/y)	2.18	8.30	32.53
$E_{PV,H2-\mathrm{CAES}}$ (GWh/y)	28.70	53.47	91.02
$E_{PV,PEM}$ (GWh/y)	20.93	38.96	66.30
$E_{PV,C}$ (GWh/y)	7.77	14.51	24.72
$E_{T,G}$ (GWh/y)	9.87	18.37	31.29
E_G (GWh/y)	34.07	115.23	128.16

$* \eta_{RT} = E_{T,G}/E_{PV,H_2-\mathrm{CAES}}$

A 3D view of the three performance indicator values for $\dot{E}_{PV} = \dot{E}_T$ is reported in Figure 27.

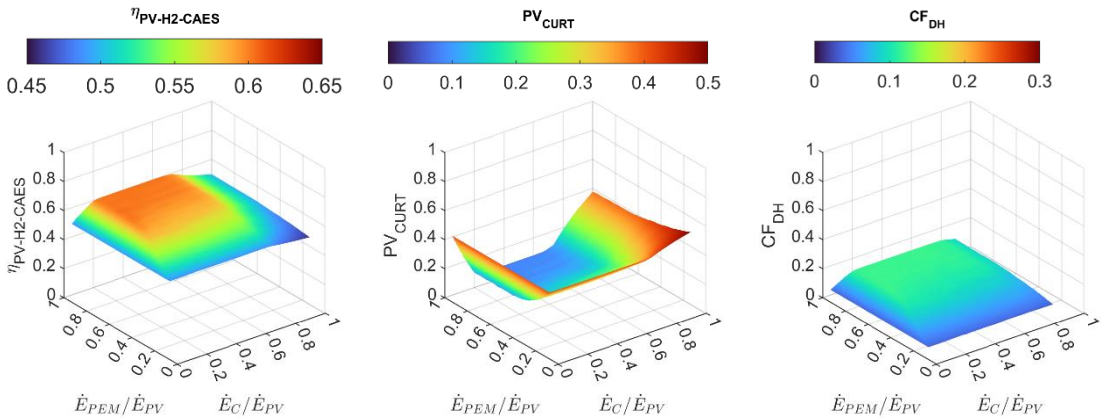

(a) (b) (c)

Figure 27. Performance indicators η_{PV-H_2-CAES} (a), PV_{CURT} (b) and CF_{DH}(c) for $\dot{E}_{PV} = \dot{E}_T$

5.3.12 PV-H2-CAES system seasonal performance

Figure 28 shows the seasonal trend of PV_{CURT} as well as the distribution of the potential PV energy generation between the three main flows: $E_{PV,G}$, E_{PV,H_2-CAES} and $E_{PV,CURT}$. Figure 29 displays the seasonal variations of η_{PV-H_2-CAES} as well as the distribution of the seasonal energy generation of the PV-H2-CAES plant, highlighting the contributions from both the direct PV feed-ins and the CAES feed-ins. Figure 30 displays the seasonal CF_{DH} of the H2-CAES plant, along with the seasonal maximum potential and effective CAES feed-ins.

During winter, which is the season characterized by the lowest levels of solar irradiance in California, the potential of the PV system can be fully exploited: in fact, there is no curtailment, and 100% of the PV energy is directly fed into the grid. Consequently, the η_{PV-H_2-CAES} is equal to one and the winter CF_{DH} of the plant is equal to zero. On the contrary, during seasons with high levels of solar irradiance, namely spring and summer, only a small amount of PV energy is directly fed into the grid (22% in spring and 7% in summer), and almost all the remaining energy, otherwise curtailed, can be stored by the CAES system. The stored energy is subsequently used to produce energy during dark hours. Indeed, the CF_{DH} during spring and summer reaches values within the range of $0.2-0.3$. The energy transformation processes involved in the H2-CAES section during spring and summer determine lower η_{PV-H_2-CAES} values compared to winter, with a minimum of about 0.36.

During autumn, the behavior of the PV-H2-CAES system lies between the two scenarios previously described. In fact, a significant share of energy is directly fed into the grid, while the remaining is mostly stored by the CAES system, with only 3% of generation curtailment. In scenarios with even higher RES penetration, these results suggest that such a system could be considered a viable solution also for seasonal energy storage, although this entails a significant increase in the size of the storage sections. This way, the plant could theoretically eliminate any curtailment during the seasons with overgeneration and generate inertial power even during winter.

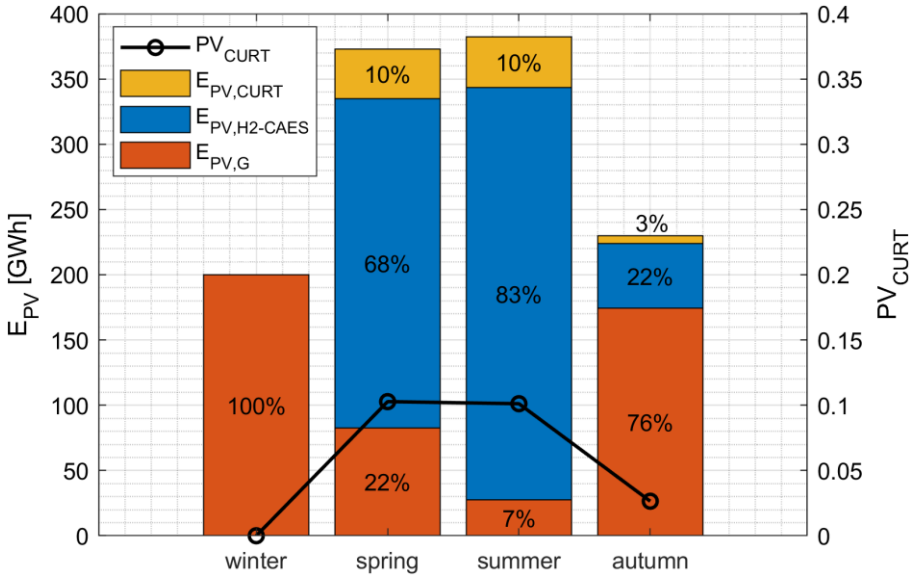

Figure 28. Seasonal E_{PV} ($E_{PV,CAES}$, $E_{PV,G}$, $E_{PV,CURT}$) and PV_{CURT} for the set of design parameters which maximizes the performance when $\dot{E}_{PV}$=$\dot{E}_T$.

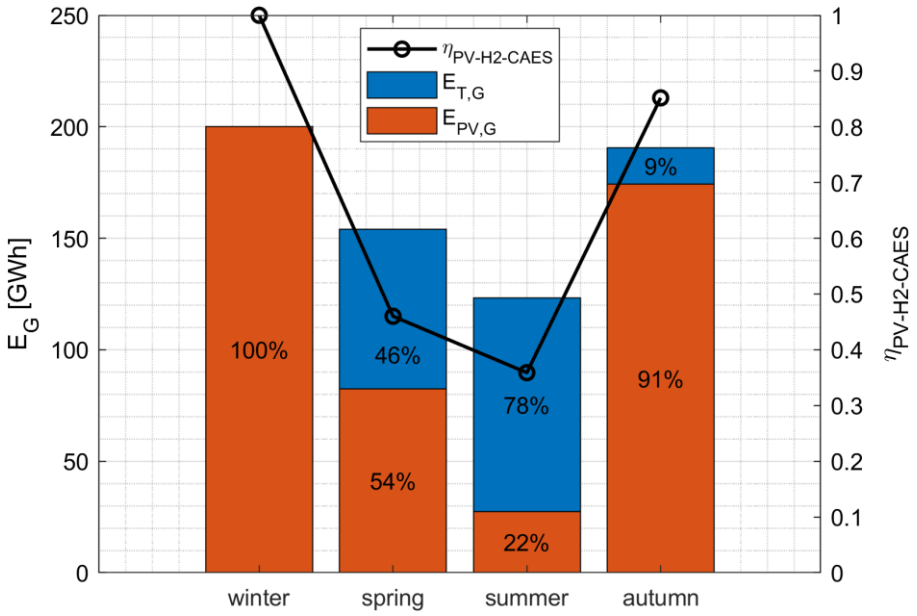

Figure 29. Seasonal E_G ($E_{T,G}$, $E_{PV,G}$) and η_{PV-H_2-CAES} for the set of design parameters which maximizes the performance when $\dot{E}_{PV}$=$\dot{E}_T$.

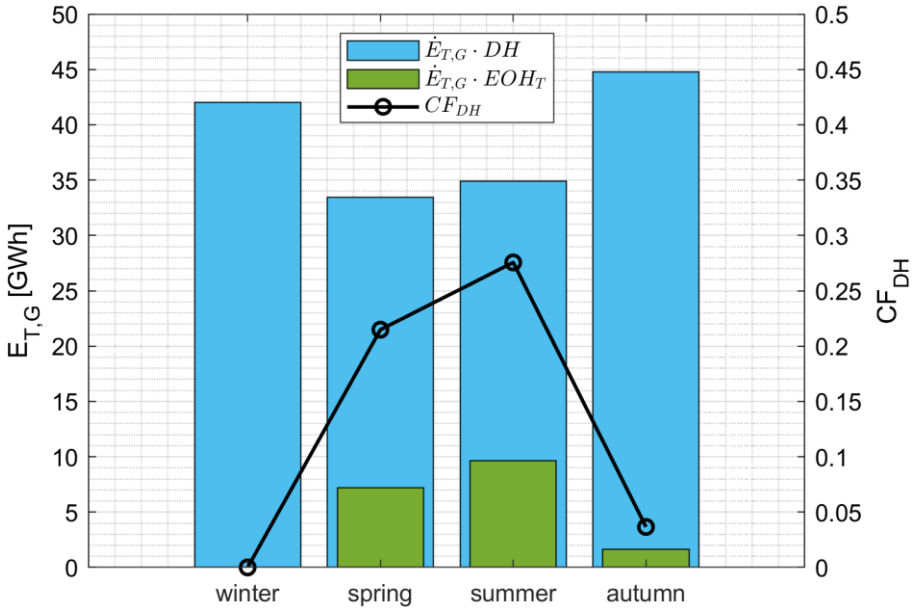

Figure 30. Seasonal $E_{T,G}$ $(\dot{E}_{T,G} \cdot EOH_T, \dot{E}_{T,G} \cdot DH)$ and CF_{DH} for the set of design parameters which maximizes the performance when $\dot{E}_{PV}$=$\dot{E}_T$.

5.3.13 Summary of PV-H2-CAES performance

In a case study represented by a real grid with high-variable renewables penetration and frequent dispatchability issues, the analysis demonstrates that the hydrogen-fueled CAES system is capable of storing for subsequent use the otherwise curtailed renewable energy, with a system efficiency of about 62% and a capacity factor during dark hours of about 20%, reducing curtailment to a minimum of 4%. The system is particularly suited to exploit PV generation during spring and summer, as it can store up to 88% of the excess generation.

In light of the results, the integrated PV-H2-CAES system appears to be a promising option to allow the connection of additional RES power even in grids with high variable renewables penetration. Additionally, the system assists in addressing high ramp rates and ramping ranges and provides inertial power during dark hours, reinforcing the grid resilience and increasing the RES share on the energy mix.

5.4 Hydrogen integration in Pumped Hydro systems

Techno-economic performance of unpredictable renewables is often assessed without considering dispatch limitations over the lifetime. This assumption is increasingly less likely, and generation curtailment can reduce performance and increase LCOE. For this reason, this analysis first examines the efficiency decline and LCOE rise for floating photovoltaics coupled with pumped hydro storage connected to grids with high curtailment levels. Findings confirm that performance degradation is mitigated by enhancing self-consumption. Subsequently, the integration of a water electrolyzer is studied to consume photovoltaic electricity with secondary priority to the pumped hydro, to improve efficiency, reduce LCOE, and produce green hydrogen. Unlike other

curtailment mitigation techniques, hydrogen production from excess generation allows decarbonizing hard-to-abate sectors. The analysis is conducted considering a pumped hydro energy storage system setup in Sardinia (Italy), integrated with floating photovoltaics and anion exchange membrane electrolyzers of various sizes.

In this framework, power generation and energy storage integrated systems capable of storing great amounts of surplus VRES generation will be particularly valuable in the future [125], as they allow for the reduction of VRES curtailment while increasing the overall revenue. Numerous promising solutions are currently studied, such as integrated plants [126], [127] that leverage the advantages of coupling the same natural resource with different conversion and storage technologies [128]. Among them, one of the most interesting options focuses on floating photovoltaic integrated with PHES systems and water electrolyzers.

FPV systems [129] allow for decoupling the required PV generation from land consumption [130]. Unlike Ground-mounted Photovoltaic (GPV), FPV technology involves installing PV modules on water surfaces, such as seas and lakes, with comparable OPEX costs and an average of 10% higher CAPEX costs. According to Elminshawy et al. [131], who conducted an experimental study in the region of Port Fuad in Egypt, FPV systems present a Levelized Cost Of Electricity (LCOE) below 60 $/MWh for a lifetime of 25 years, considering an average daily solar radiation of 718.3 W/m^2 and a daily average temperature of 33.5 °C. FPV systems provide numerous benefits, including higher efficiency due to the cooling effect of water on cell temperature and the minimized shading effects on modules [132], lower dust accumulation [133], and the potential for using bifacial modules [132]. Moreover, capital costs for land acquisition and preparation are reduced [134]. Additionally, FPV reduces evaporation of water bodies by about 7,000-10,000 cubic meters per MW of installed capacity, while mitigating algae growth [134]. On the other hand, the effect of large-scale FPV installations on water quality and the related ecosystem is not yet fully understood [135]. It is established that, when FPV systems are installed in saltwater, there is accelerated degradation of cables, reduced electrical insulation, and copper release into the water [136].

Integrating FPV systems into existing PHES systems effectively provides an ESS without additional CAPEX [137], significantly enhancing its economic viability [138]. Ghandehariun et al. [139] proposed a PHES system comprising both photovoltaic and wind technologies, calculating an LCOE lower than 100 $/MWh. The proposed plant is located in Iran, where the maximum irradiance throughout the year is 1,081 W/m^2 with an average monthly temperature of 36.6 °C.

Integrating FPV technology with hydrogen production is seen as a promising solution for the energy transition, as described by Temiz et al. [140]. In their study, they assessed the performance of a PEM electrolyzer integrated with an FPV plant and a hydrogen fuel cell, for a case study in Turkey. The study demonstrated excellent results in terms of increased

Self-Consumption (SC), but with an unsustainable LCOE of 612 $/MWh. However, better profitability indices can be achieved if hydrogen is used for external applications, such as in hard-to-abate sectors. This underscores why green hydrogen production via FPV systems is seen as a promising area for further research [134].

5.4.1 FPV-PHES-AEM plant configuration

The analysis considers integrating an FPV system first, and later an AEM electrolyzer, into a baseline PHES setup. The schematic of the complete FPV-PHES-AEM configuration is reported in Figure 31, showing the main energy and material flows. The analysis considers an existing river-based PHES system. Due to the high energy costs associated with pumping water, the existing PHES facility is currently used as an impoundment facility, generating energy (EHPP) only in response to the water demand of the downstream district. The integration of an FPV plant enables the PHES system to effectively provide an energy storage service (EPHES).

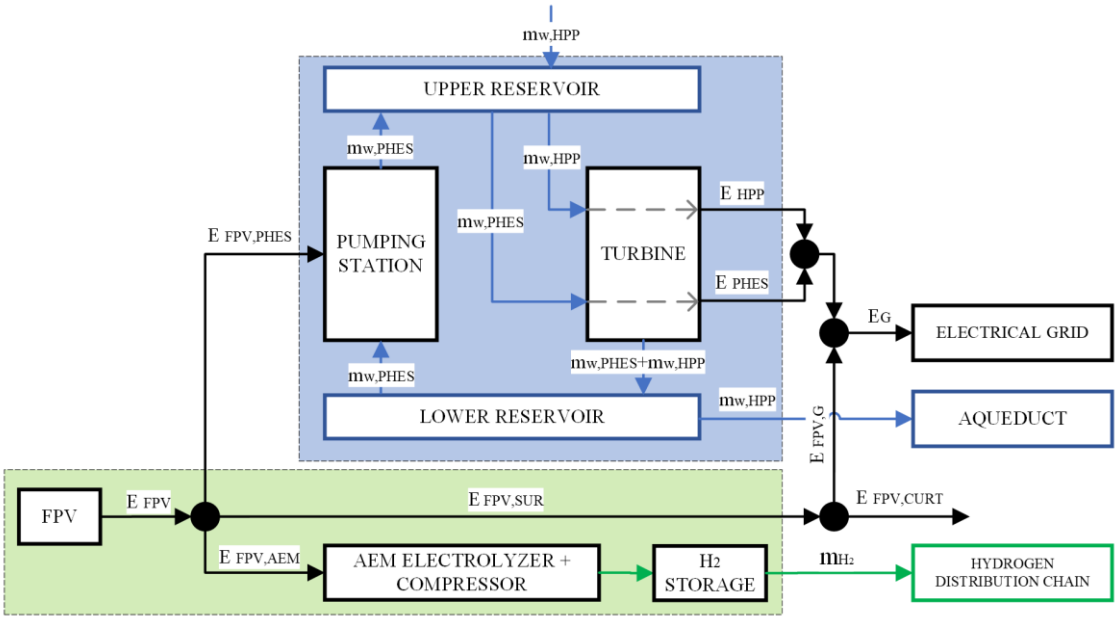

Figure 31. Energy and material flows of the FPV-PHES-AEM system.

The FPV system supplies the energy for pumping water ($E_{FPV,PHES}$) and for operating the AEM electrolyzer ($E_{FPV,AEM}$). Starting from the stored water, the hydro turbine generates additional electricity (E_{PHES}) for the grid. Depending on the possibility of dispatch, the surplus FPV energy ($E_{FPV,SUR}$) is fed into the grid ($E_{FPV,G}$) or curtailed ($E_{FPV,CURT}$). The first case is herein named NO-CURT scenario, while the latter CURT scenario. The two scenarios are opposite: in the CURT the FPV power dispatch is never allowed ($E_{FPV,SUR}=E_{FPV,CURT}$ and $E_{FPV,G}=0$), while in the NO-CURT the surplus FPV power dispatch is always allowed ($E_{FPV,SUR}= E_{FPV,G}$ and $E_{FPV,CURT}=0$). These two scenarios are useful for evaluating PV-based systems connected to grids with very high levels of photovoltaic curtailment (CURT scenario) compared to grids that accept photovoltaic feed-ins (NO-CURT scenario). Many intermediate solutions will lie between these two

opposite scenarios. While the CURT is a forward-looking scenario, the NO-CURT represents an increasingly unlikely scenario.

A logical scheme of the energy management strategy considered in the analysis is reported in Figure 32. FPV energy is firstly used for PHES charging ($E_{FPV,PHES}$), and secondly, to operate the electrolyzer ($E_{FPV,AEM}$). Any excess FPV production represents the energy surplus ($E_{FPV,SURP}$). If the dispatch is allowed (NO-CURT scenario), energy surplus is fed in the grid; otherwise (CURT scenario), it is curtailed. Referring to the PHES discharge, it starts only if the turbine is not already in operation in response to the district water demand. Additionally, discharge starts only after sunset, lasting 4 hours at nominal flow conditions. The choice of the 4-hour discharge period is based on an analysis of the highest hourly zonal marginal prices of electricity for non-PV production hours, typically corresponding to the four hours immediately after sunset. This period reflects the higher residual electricity demand during the evening peaks, compared to other times of the day. Therefore, by generating energy during these hours, a valuable service is provided to the electricity grid.

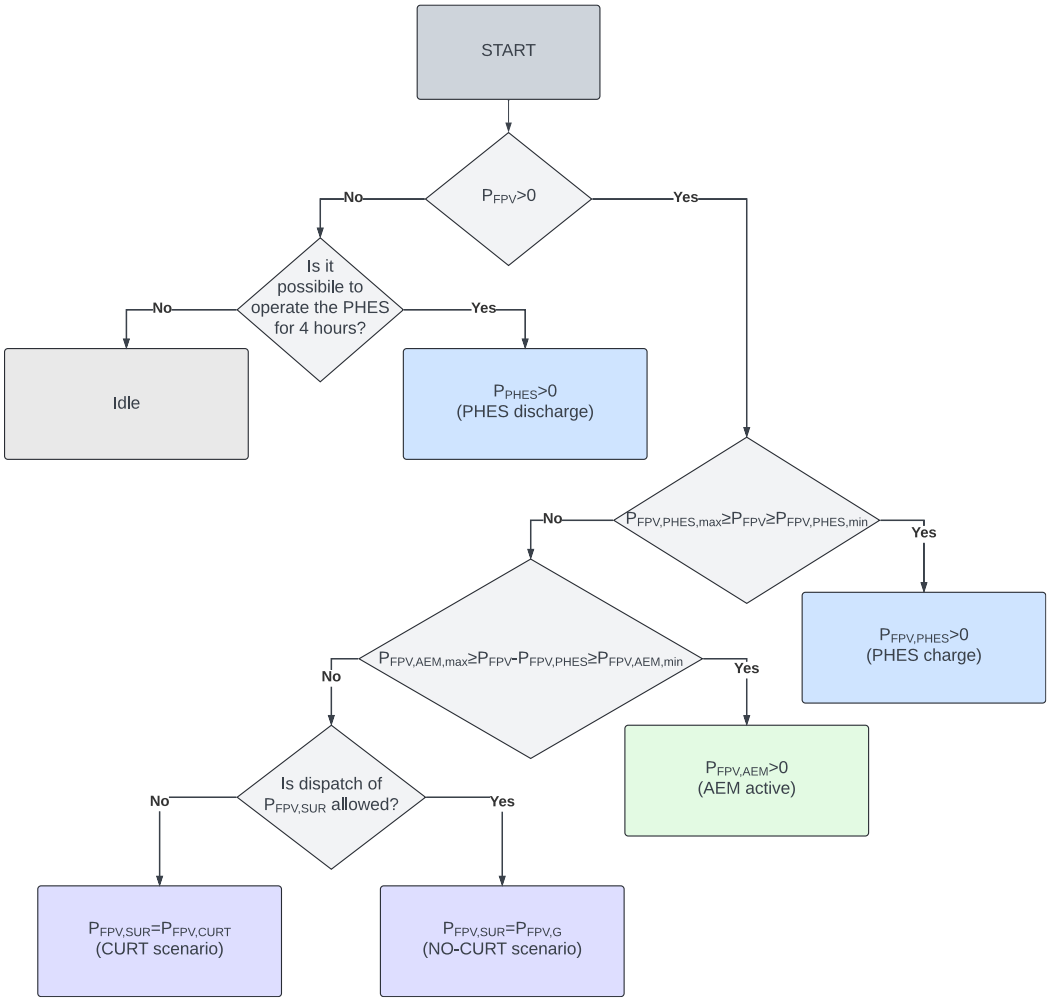

Figure 32. Logical scheme of the FPV-PHES-AEM energy management strategy.

Figure 33 illustrates the results of the EMS applied to the FPV-PHES-AEM system throughout a typical day. In the diagram, positive values represent the electricity self-consumption of the system (charge phase), either for water pumping or hydrogen production, while negative values represent the electricity generated by the system. $E_{FPV,SUR}$ is represented for completeness, although it can be entirely fed into the grid ($E_{FPV,G}$) or partially/totally curtailed ($E_{FPV,CURT}$) and consequently not produced, depending on the dispatch possibilities. As previously mentioned, EHPP is a constraint, but it is not accounted for in the system's performance evaluation.

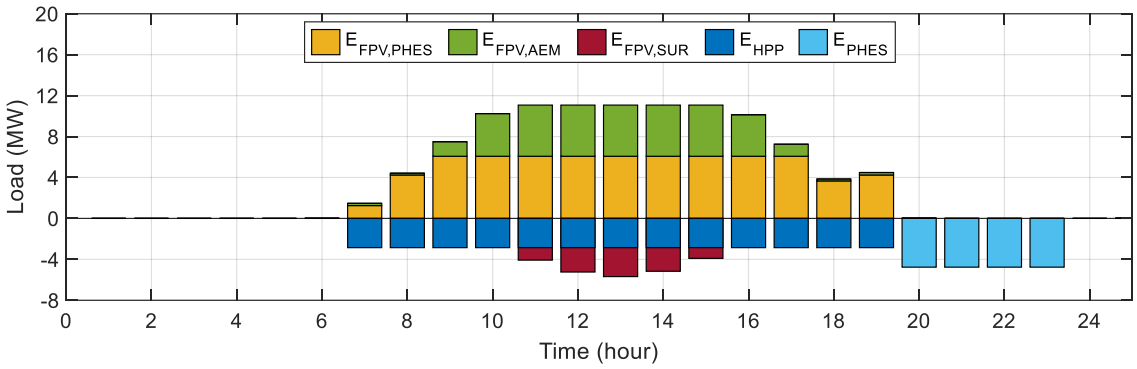

Figure 33. Energy management strategy of the FPV-PHES-AEM system. Positive values: consumption, negative values: feed-in.

5.4.2 Mathematical model and parameters

The mathematical model of each section of the integrated FPV-PHES-AEM system was developed utilizing MATLAB version R2024a. Computational simulations were conducted considering a time horizon of one Typical Meteorological Year (TMY) sourced by NREL [141] and a time step of one hour.

The PHES system considered in this analysis is located in Sardinia, Italy, and includes a Francis turbine, a pumping station, and two reservoirs. The design parameters are reported in Table 11, and the capacity curve and monthly filling profile of the upper reservoir are reported in Figure 34a and Figure 34b, respectively.

Table 11. PHES plant design parameters.

Component	Parameter		Value	Unit
Upper reservoir	Authorized capacity	$V_{UP,auth}$	420	10^6 m^3
	Maximum capacity	$V_{UP,max}$	792	10^6 m^3
	Elevation (min-max)	h_{UP}	55.45 – 118	m
Lower reservoir	Authorized capacity	$V_{LOW,auth}$	9.5	10^6 m^3
	Maximum capacity	$V_{LOW,max}$	9.5	10^6 m^3
	Elevation (min-max)	h_{LOW}	38 – 45	m
Hydraulic turbine (Francis)	Nominal power	$P_{T,nom}$	19.6	MW
	Nominal flow	Q_T	30	m^3/s
	Maximum head	$h_{T,max}$	118	m
	Minimum head	$h_{T,min}$	66	m
	Useful head (design conditions)	$h_{T,des}$	78.2	m
	Efficiency (nominal conditions)	$\eta_{T,nom}$	0.91	-
Pump type 1 (constant speed)	Number of pumps	-	2	-
	Nominal power	$P_{P1,nom}$	0.627	MW
	Nominal flow	$Q_{P1,nom}$	0.625	m^3/s
	Nominal head	$h_{P1,nom}$	80.5	m
	Nominal efficiency	$\eta_{P1,nom}$	0.78	-
Pump type 2 (constant speed)	Number of pumps	-	4	-
	Nominal power	$P_{P2,nom}$	1.205	MW
	Nominal flow	$Q_{P2,nom}$	1.2	m^3/s
	Nominal head	$h_{P2,nom}$	80.5	m
	Nominal efficiency	$\eta_{P2,nom}$	0.78	-

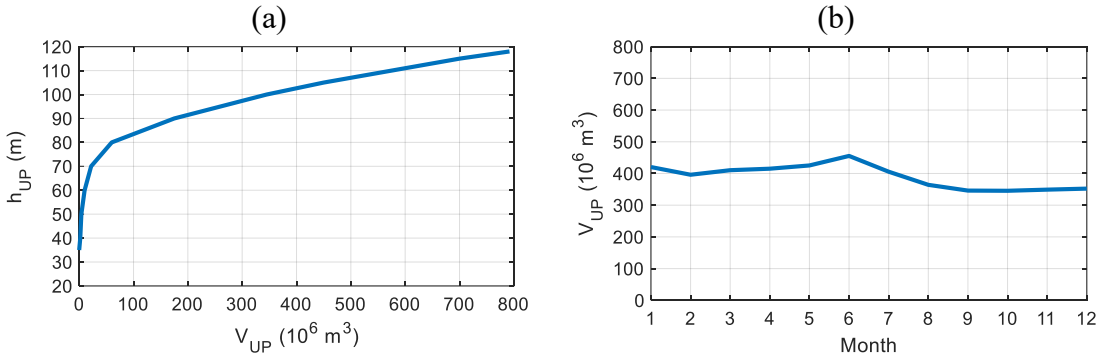

Figure 34. Capacity curve (a) and monthly filling profile during 2023 (b) of the upper reservoir.

The pumping station includes six constant-speed electric pumps: two of Type 1 (0.627 MW) and four of Type 2 (1.205 MW). The number and type of pumps activated are optimized hour by hour by the EMS to maximize the utilization of the FPV power production.

Table 12 reports the FPV system design parameters assumed in this study, primarily derived from the technical data of a commercial 500 W module [142]. Figure 35 shows the GI, T_{amb} and U_{wind}, obtained from the NREL database for a TMY for the considered location (40°06'40.6"N 8°54'00.6"E). The site is characterized by an average and maximum GI of 0.2 kW/m^2 and 1.1 kW/m^2 respectively, and a yearly global irradiation of 1,758 kWh/m^2.

Table 12. FPV system design parameters.

Parameter	Ref.	Value	Unit
Nominal power of a PV module	[61]	500	Wp
Area of a PV module	[61]	2.12	m^2
Tilt/azimuth angle	[60]	10/0	°
Derating factor (f_{PV})	[60]	0.90	-
Nominal inverter efficiency (η_{INV})	[62]	0.978	-
Temperature correction factor (β_{ref})	[61]	$-0.275 \cdot 10^{-2}$	K^{-1}

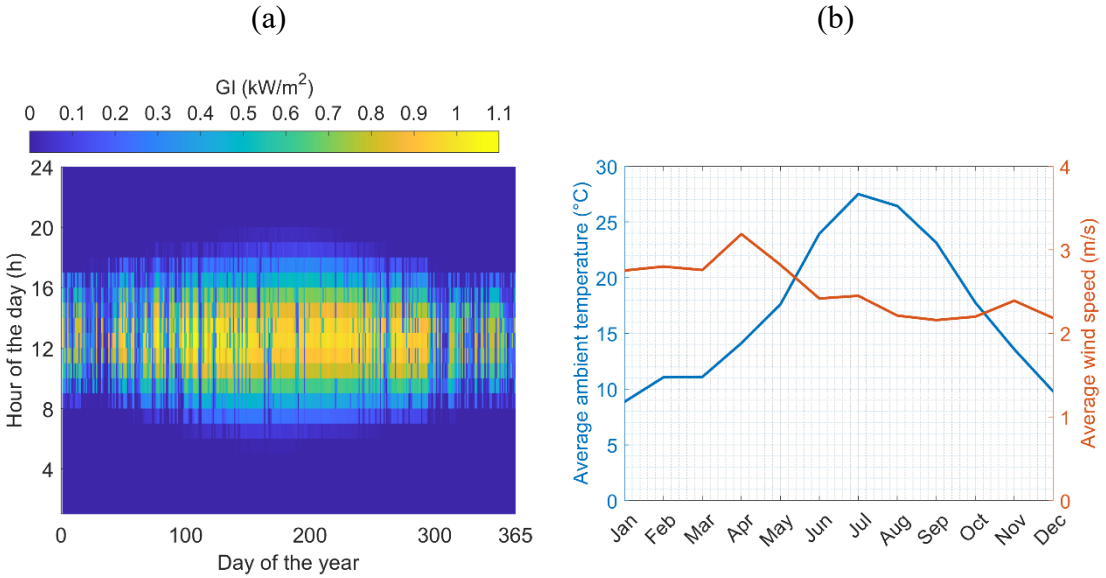

Figure 35. Global irradiance (a) and average ambient temperature and wind speed (b) for the considered location (TMY).

The hydrogen production, compression, and storage system considered in the analysis is composed of an AEM electrolyzer, a hydrogen compressor, and a pressurized tank.

The model was validated by comparing the calculated performance with that of a commercial AEM electrolyzer [143]. Validation results are reported in Table 13 together with the AEM electrolyzer design parameters.

Table 13. AEM electrolyzer design parameters and validation results.

Parameter	Ref.	Value		Unit
		Commercial	Present study	
AC voltage		3x400	3x400	V
Number of cells	[143]	420	420	-
Nominal power	[143]	1.008	1.008	MW
H_2 outlet pressure	[143]	35	35	bar
H_2 outlet temperature	[143]	55	55	°C
Operational flexibility	[143]	3%-100%	3%-100%	-
H_2 nominal flow rate	[143]	18.875	18.889	kg/h
Specific power consumption	[143]	53.30	53.30	kWh/kgH_2
Membrane cross-sectional area	[144]	n.a.	500	cm^2
Electrode cross-sectional area	[144]	n.a.	500	cm^2
Membrane thickness	[47]	n.a.	$50 \cdot 10^{-6}$	cm
Electrode thickness	[47]	n.a.	$8 \cdot 10^{-3}$	cm

To ensure compatibility with hydrogen-tube trailers, the most prevalent hydrogen transport system for hard-to-abate sectors [145], a pressurized hydrogen tank operating at

200 bar is selected. According to Tjarks et al. [146], the compression energy needed to raise hydrogen pressure from 35 (AEM outlet) to 200 bar (storage) equals 0.75 kWh/kgH_2. Since this energy represents less than 1.5% of the electrolyzer specific energy consumption (53.30 kWh/kgH_2), it is included in the total electrolyzer consumption. Therefore, when referring to the AEM's power (P_{AEM}), it is understood that this includes the power of the compressor as well.

5.4.3 Performance indicators

The performance assessment, carried out for both the FPV-PHES-AEM and the FPV-PHES configuration, is conducted by means of the First-law efficiency (η_I), the Self-Consumption of the FPV energy, the LCOE, and the LCOH. Performance is also discussed in terms of electricity flows, enabling combined assessments of both the PHES and FPV system generations, and yearly hydrogen generation.

More in detail, the first-law efficiency (η_I), hereafter referred to simply as "efficiency", is calculated as:

$$\eta_I = \frac{E_{PHES} + E_{FPV,G} + E_{H2}}{E_{FPV}} \tag{5.4}$$

Where the energy associated with hydrogen E_{H2} has been calculated considering a Lower Heating Value of 120 MJ/kg.

The self-consumption SC is defined as the ratio between the sum of the FPV energy self-consumed by the plant to power the PHES system (in the FPV-PHES configuration) or the PHES and AEM systems (in the FPV-PHES-AEM configuration), over the total FPV generation for one year.

$$SC = \frac{E_{FPV,PHES} + E_{FPV,AEM}}{E_{FPV}} = 1 - \frac{E_{FPV,SUR}}{E_{FPV}} \tag{5.5}$$

The levelized cost of electricity for both the FPV-PHES-AEM configuration and the FPV-PHES configuration is calculated as:

$$LCOE = \frac{c_{FPV}\, E_{FPV,G} + \, c_{PHES}\, E_{PHES}}{E_{FPV,G} + E_{PHES}} \tag{5.6}$$

The cost of electricity produced from the FPV system c_{FPV} is evaluated according to Elminshawy et al. [131], considering a yearly PV module degradation (d) of 0.5% and the actual generation (net of curtailment):

$$c_{FPV} = \frac{\sum_n \frac{(CAPEX + OPEX)_n}{(1+i)^n}}{\sum_n \frac{(E_{FPV} - E_{FPV,CURT})(1-d)^n}{(1+i)^n}} \tag{5.7}$$

While the cost of electricity produced from the PHES system c_{PHES} is calculated based on Ghandehariun et al. [139]. In particular, c_{PHES} includes both the operational expenditures and the initial expenses for the revamping of the existing PHES

electromechanical components (REVEX), estimated at 10% of the greenfield construction cost [139] based on a preliminary assessment for the specific plant:

$$c_{PHES} = \frac{\sum_n \frac{\left(REVEX + OPEX + E_{FPV,PHES} \cdot c_{FPV}\right)_n}{(1+i)^n}}{\sum_n \frac{E_{PHES}}{(1+i)^n}} \tag{5.8}$$

Referring to the FPV-PHES-AEM configuration, the levelized cost of hydrogen is calculated according to Kim et al. [48] as well as Moran et al. [147] as:

$$LCOH = \frac{\sum_n \frac{\left(CAPEX + OPEX + E_{FPV,AEM} \cdot c_{FPV}\right)_n}{(1+i)^n} + \sum_n \frac{(CAPEX + OPEX)_n}{(1+i)^n}}{\sum_n \frac{m_{H2,y}}{(1+i)^n}} \tag{5.9}$$

where the first term refers to hydrogen production and compression, and the second to storage.

Because the PHES pumping system, hydrogen electrolyzer, and compressor use the electrical energy produced by the FPV plant, the LCOE of the PHES and the LCOH are calculated starting from the cost of electricity generation of the FPV section. All costs are calculated considering the cost assumptions reported in Table 14, with a discount rate (i) of 4.5% and a lifetime of 25 years. This lifetime represents the minimum among the operational life spans of the PHES system, the FPV system [148], and the AEM electrolyzer [149]. Regarding the degradation of the components, the economic model accounts for the yearly efficiency loss of the photovoltaic modules which reduces the energy available for hydrogen production over time. For the electrolyzer, distinct capital expenditures for periodic stack replacements are considered by matching the stack lifetime with the project horizon of 25 years. Therefore, the costs associated with performance degradation are considered within the OPEX costs.

Table 14. LCOE and LCOH assessment assumptions.

Subsystem	Parameter	Ref.	Value	Unit
FPV	PV module	[131], [150]	0.22	$/W
	Electrical components	[131]	0.12	$/W
	Supplementary costs	[131], [150]	0.23	$/W
	Balance Of System	[131]	0.13	$/W
	Floater system	[131]	0.14	$/W
	Operation and maintenance	[131]	0.026	$/W/y
PHES	Investment cost for revamping	[139]	0.13	$/W
	Operation and maintenance	[139]	0.025	$/W/y
AEM	Stack components	[48]	0.19	$/W
	Balance of Plant	[48]	0.26	$/W
	Supplementary costs	[48]	0.37	$/W
	Operation and maintenance	[48]	0.056	$/W/y
H_2 storage (200 bar)	Capital cost	[151]	385	$/kg
	Operation and maintenance	[151]	7.7	$/kg/y
H_2 compressor	Capital cost	[151]	$4{,}948 \cdot P^{0.66}$	$
	Operation and maintenance	[151]	$98 \cdot P^{0.66}$	$/y

5.4.4 FPV-PHES configuration results

For the case study, the floating photovoltaic system has been sized to maximize the use of the existing electrical connection of the turbine (25 MW). This approach is typically adopted to enable the dispatch of 100% of the FPV power. Given that, the AEM electrolyzer size is varied within the range from 1 to 20 MW, which ensures 100% self-consumption even at the highest P_{FPV}. The hydrogen tank size is calculated, for each configuration, to store the maximum daily hydrogen production realized throughout the year.

With reference to the FPV-PHES configuration, Figure 36a shows the components of the energy produced by the FPV system EFPV ($E_{FPV,PHES}$, $E_{FPV,SUR}$) and the self-consumption SC for different FPV sizes. Figure 36b shows the PHES and FPV surplus energy generation, as well as the efficiency (η_I). Figure 36c shows the LCOE under the two scenarios (CURT and NO-CURT), while Figure 36d displays the total volume of water flowing through the turbine of the PHES systems for one year.

In Figure 36a, the trend is caused by the fact that, to the left of the peak, the FPV system is undersized relative to the PHES pumping system duty point (3.9 MW), while to the right of the peak, the FPV system is oversized. As the size of the FPV grows, an increasing amount of energy is available to the PHES pumps, up to their maximum capacity (around 6 MW). Beyond this point, increasing shares of FPV energy cannot be utilized by the pumping system, and therefore, the surplus FPV energy grows faster.

The efficiency (η_I) of the FPV-PHES system is shown in Figure 36b for both the CURT ($E_{FPV,SUR}$=$E_{FPV,CURT}$ and $E_{FPV,G}$=0) and the NO-CURT ($E_{FPV,SUR}$=$E_{FPV,G}$ and $E_{FPV,CURT}$=0) scenarios. For low FPV sizes, the PHES generation (E_{PHES}) increases with increasing PV power, while the share of surplus PV energy ($E_{FPV,SUR}$) remains constant. Beyond the maximum SC point, as P_{FPV} increases, in the NO-CURT scenario, the efficiency increases because direct FPV feed-ins increase; in the CURT scenario, the efficiency decreases because FPV production is increasingly curtailed. An effective method to mitigate the variation in system efficiency caused by the level of curtailment is to maximize self-consumption.

Figure 36c shows the LCOE of the FPV-PHES system for both the CURT and the NO-CURT scenarios. The trend of the two LCOEs is strongly correlated with the efficiency trends described above. In fact, the LCOE of the NO-CURT scenario decreases as the FPV size increases, and consequently, the share of FPV feed-ins (and efficiency) rises. Like the efficiency trends, larger shares of FPV energy are curtailed rather than used. The gap between the LCOE in the CURT scenario and the LCOE in the NO-CURT scenario widens as the level of self-consumption decreases, while it is minimized at higher self-consumption values.

Figure 36d shows that increasing the power of the FPV system results in an increased water transfer between the two reservoirs because a larger amount of energy can be provided to the pumping system. As the energy production of the PHES is directly related to the volume of water transferred, E_{PHES} increases with the size of the FPV plant.

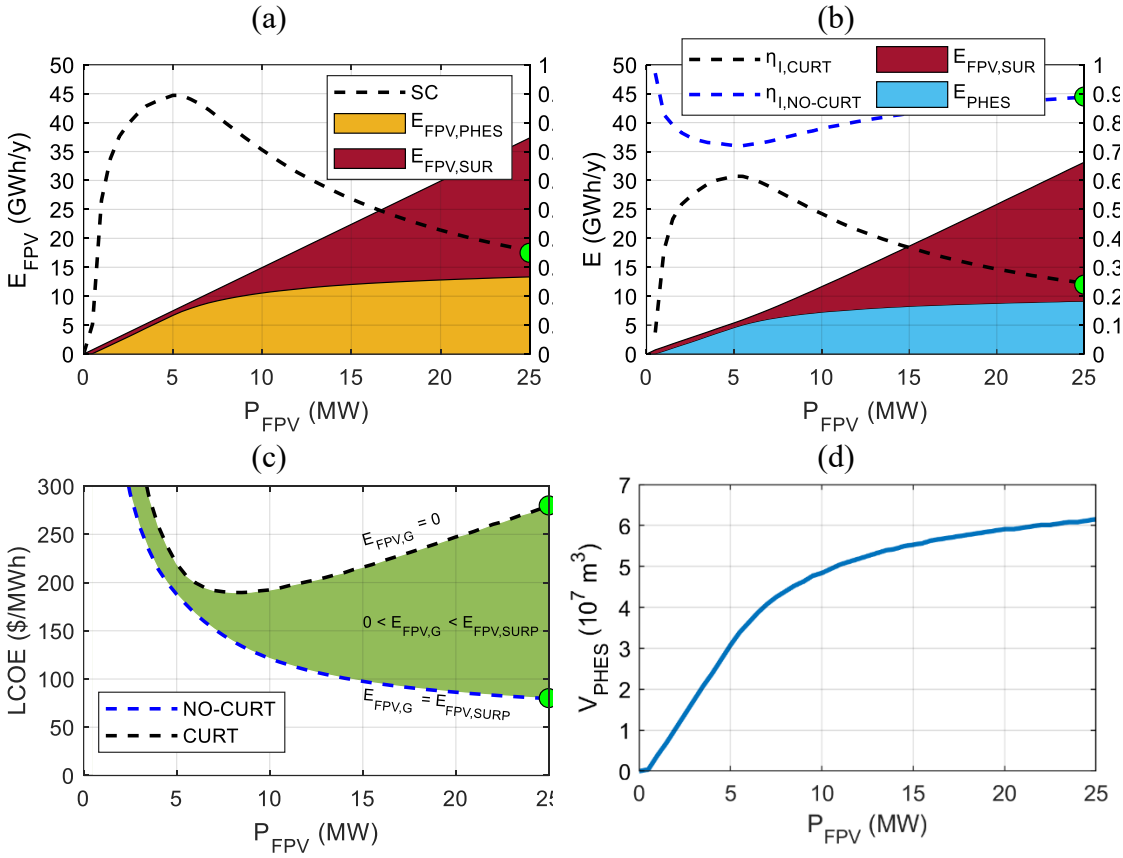

Figure 36. FPV generation and Self-Consumption (a), Electricity feed-ins and efficiency (b), LCOE (c), and VPHES (d) for various sizes of the FPV system (FPV-PHES configuration). Green dot: case study.

5.4.5 FPV-PHES-AEM configuration results

One viable approach to mitigate the increase in LCOE, even if dispatch conditions change, is to integrate an electrolyzer into the FPV-PHES configuration to simultaneously produce hydrogen. For the case study, an electrolyzer size that maximizes the self-consumption is selected.

Figure 37 presents the results in terms of self-consumption, PHES, and hydrogen generation as a function of the size of the components. A region where the FPV energy is entirely self-consumed by the PHES pumping system and by the AEM electrolyzer is identified in Figure 37a,b in the yellow area. Outside of this area, as the size of the FPV increases, the system is no longer capable of utilizing all the FPV energy, the self-consumption decreases, and the system performance is increasingly exposed to the risk of curtailment. In Figure 37d, a flat region can be observed, where the FPV generation is sufficient only to power the PHES, but not the electrolyzer.

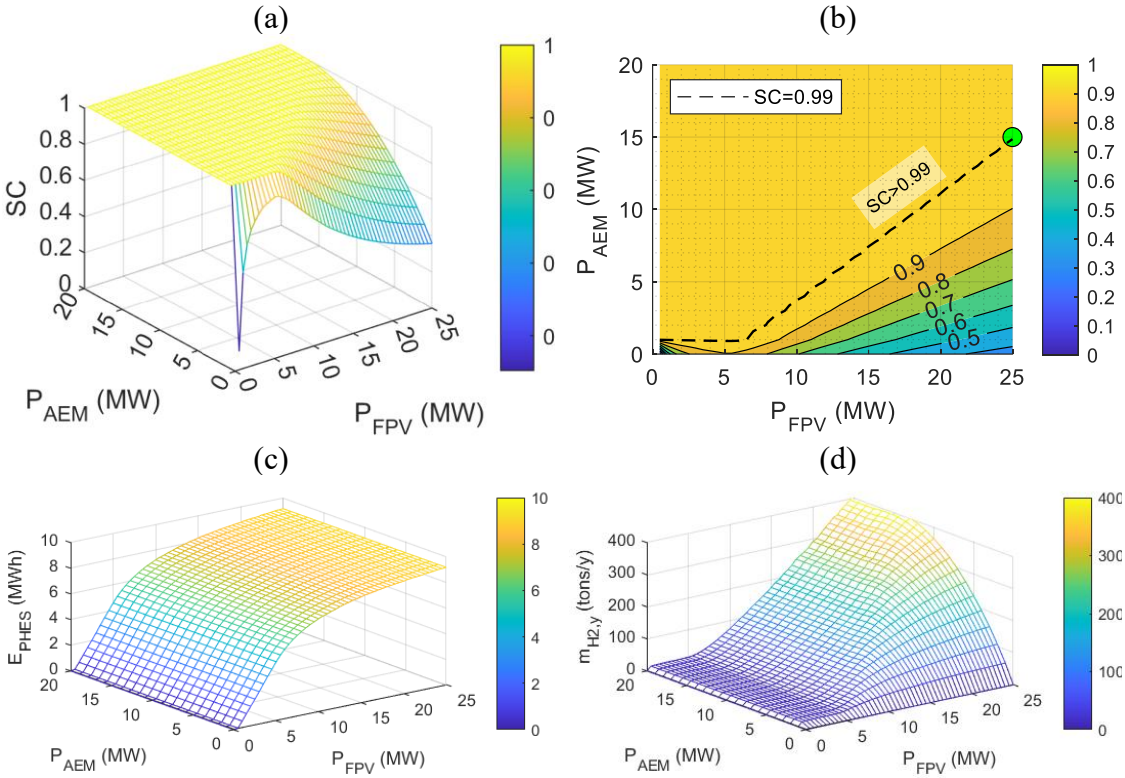

Figure 37. Self-Consumption (a), PHES (b), and hydrogen (c) generation for various sizes of the FPV and AEM systems (FPV-PHES-AEM configuration).

The annual performance of the system is presented in Figure 38. A dashed line separates the zone where the design conditions allow a SC > 0.99 (indicating a zone without FPV surplus generation) from the zone where SC < 0.99. The area where SC > 0.99 is a zone where the risk of generation curtailment is zero, regardless of the scenario.

Figure 38a shows that for FPV sizes up to about 6.5 MW (EFPV = 9.7 GWh/y), more than 85% of the FPV energy can be consumed by the pumping section of the PHES (Figure 38b). A 1 MW electrolyzer would be sufficient to achieve a self-consumption of almost 1, and, consequently, avoid surplus FPV energy (Figure 38d). Above 6.5 MW, the electrolyzer size becomes crucial for achieving high values of self-consumption. A correlation between AEM and FPV capacities for SC=0.99 can be observed. Within the region where SC<0.99, FPV surplus generation increases with increasing P_{FPV} and decreasing P_{AEM}. From Figure 38e, the electrical energy fed to the grid by the PHES (E_{PHES}) increases with increasing FPV size up to the saturation limit of the PHES system. Beyond this point, within the SC>0.99 zone, all the residual FPV energy is used to generate hydrogen. As shown by Figure 38f, for fixed values of FPV power, the surplus FPV energy generally decreases with increasing electrolyzer capacity, due to the fact that larger electrolyzers can more effectively use the surplus FPV energy, allowing for up to 99% surplus utilization. Furthermore, increasing the FPV size for a given electrolyzer capacity leads to hydrogen production and surplus FPV energy increase.

With reference to the case study, E_{FPV} is equal to 37.3 GWh/y, 35.6% of which is consumed by the PHES (13.3 GWh/y), 63.6% is consumed by the electrolyzer (23.7

GWh/y), and 0.8% is surplus (0.3 GWh/y). The resulting PHES energy generation is 9.1 GWh/y, and the hydrogen production equals 412 tons/y.

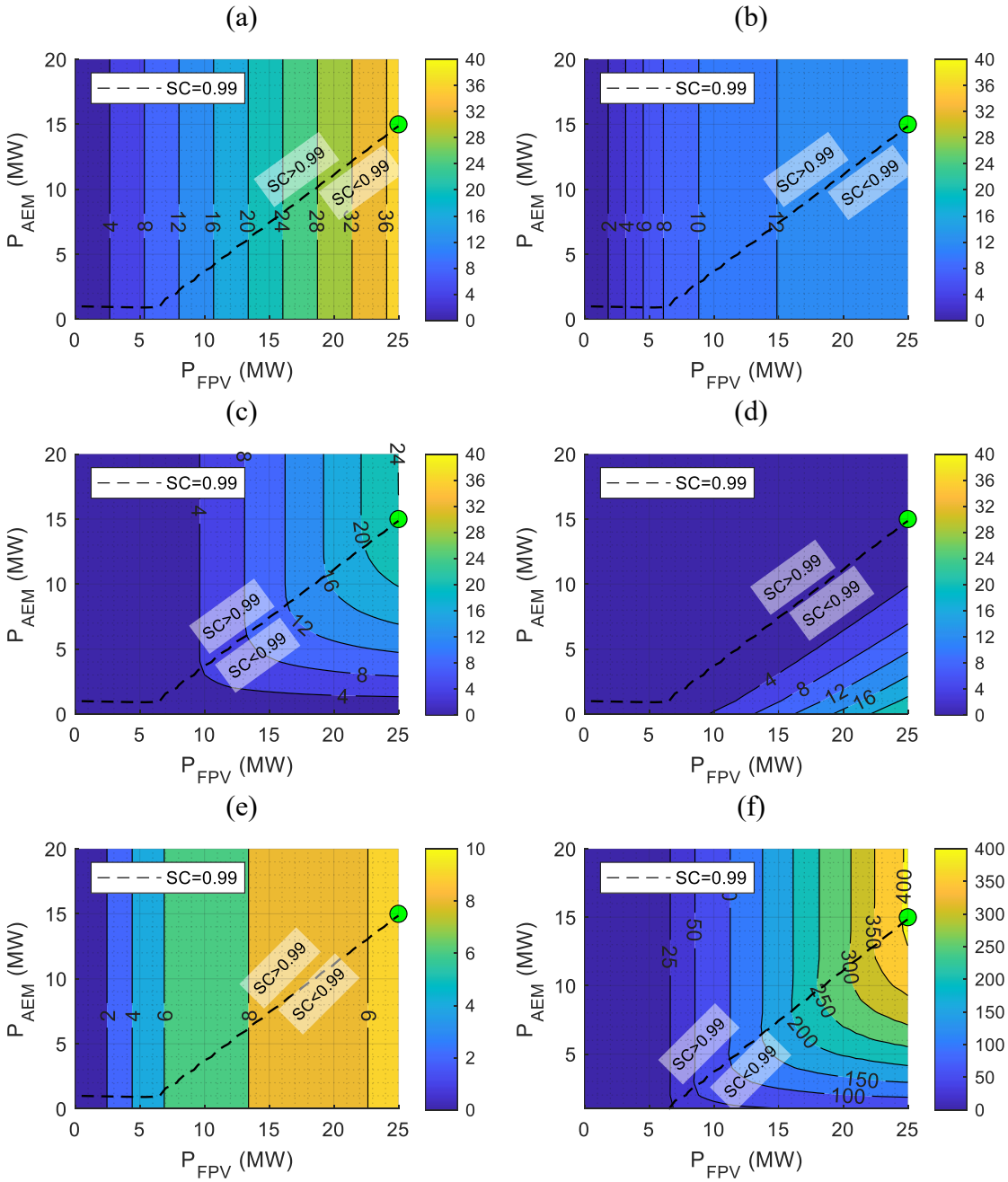

Figure 38. FPV generation (a), PHES consumption (b), AEM electrolyzer consumption (c), Surplus FPV energy (d), PHES generation (e), and hydrogen generation (f) for various sizes of the FPV and AEM systems (FPV-PHES-AEM configuration). Green dot: case study.

The results are presented in Figure 39, considering the performance indicators efficiency, LCOE, and LCOH.

As shown in Figure 39a,b, for fixed PFPV values in the NO-CURT scenario, the efficiency decreases as the P_{AEM} increases; in the CURT scenario, the opposite occurs. In

the NO-CURT scenario, feeding the FPV energy into the grid is more efficient than powering the electrolyzer; this is not possible in the CURT scenario, where it is preferable to supply power to the electrolyzer rather than lose excess energy. In the case study, the integration of an AEM allows the system's efficiency to be independent of the generation curtailment value.

From Figure 39c,d, the lowest LCOE values in the NO-CURT scenario are consistently associated with no hydrogen production. In contrast, in the CURT scenario, the lowest values for LCOE are associated with solutions that maximize self-consumption. Like for the efficiency, LCOE values for the two scenarios are comparable at SC = 0.99. In the case study, the LCOE of the FPV-PHES-AEM system is the same for both scenarios. The integration of the AEM thus allows the LCOE to be independent from generation curtailment.

Figure 39e,f shows that the LCOH ranges from 5 $/kg to over 75 $/kg for both scenarios. The lowest LCOH values are observed in the NO-CURT scenario, at the highest efficiency levels, primarily due to the lower production costs of the FPV energy that powers the electrolyzer.

In the analysis, the electrolyzer is primarily conceived to use the surplus energy that would otherwise be curtailed, giving priority to PHES energy use. Therefore, although certain combinations achieve remarkably high SC values, the capacity factor of the electrolyzer remains around 27% for minimum LCOH.

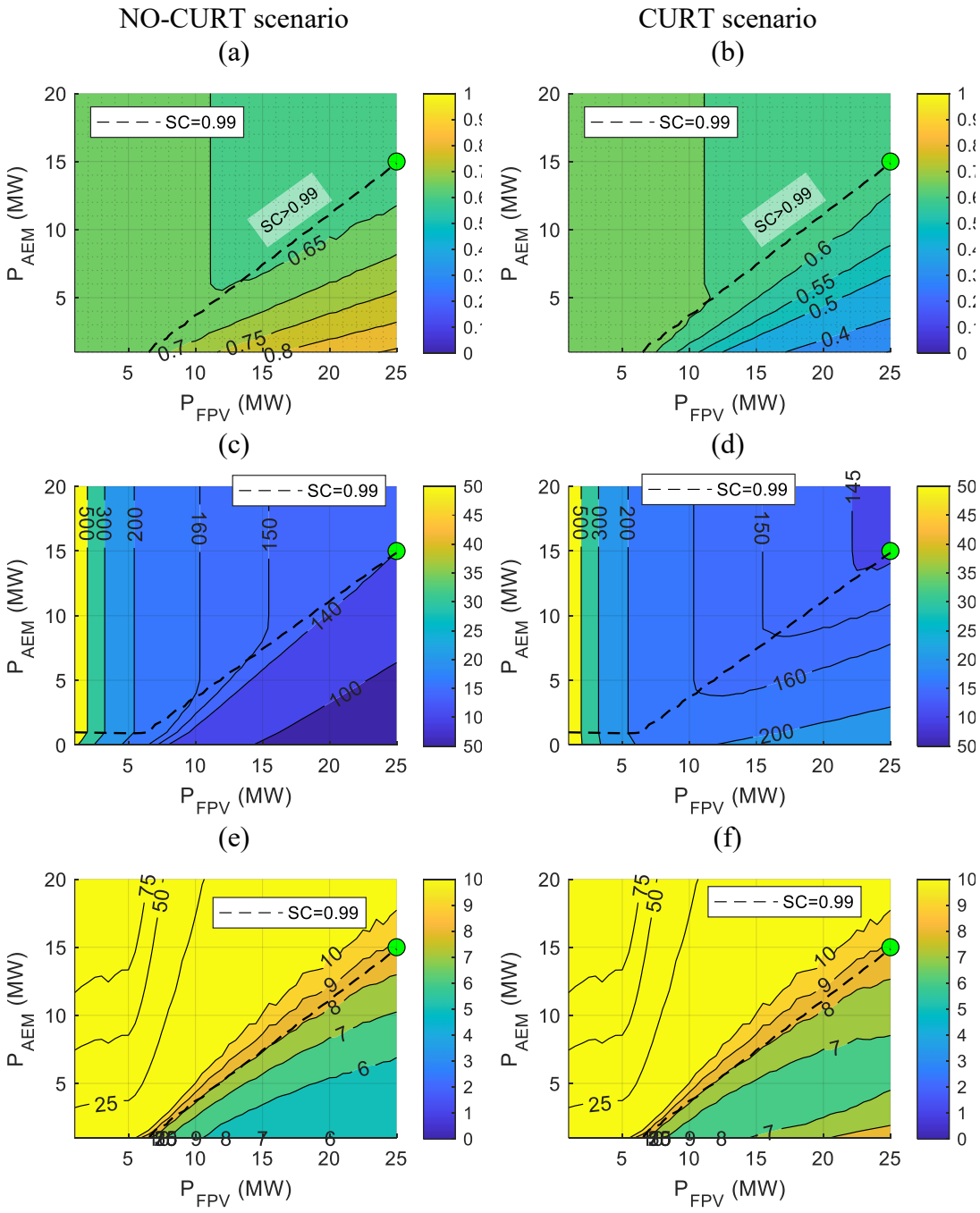

Figure 39. Efficiency (a,b), LCOE(c,d) and LCOH(e,f) for various sizes of the FPV and AEM systems (FPV-PHES-AEM configuration) in the NO-CURT and CURT scenarios. Green dot: case study.

5.5 Ammonia production

In the transition to decarbonized energy systems, green ammonia will play a key role in reducing greenhouse gas emissions. However, its production remains an energy-intensive and economically demanding process.

RES-powered ammonia production offers a low-carbon alternative to the conventional process and enables the storage and transport of renewable energy. Its potential applications include use in the mobility sector, particularly as a fuel for maritime shipping, storage and cracking into hydrogen, and direct use for electricity production in the energy sector [26]. The electrification of the Haber-Bosch process could increase the process energy efficiency by approximately 50% and reduce CO_2 emissions by 78%, aiding the transition to more sustainable ammonia production [78]. Since the HB synthesis process requires stable temperature and pressure conditions, as well as stable hydrogen and nitrogen feeds to operate efficiently, a significant challenge arises from directly powering the process with intermittent RES generation. Potential solutions include electric energy storage via batteries, hydrogen storage tanks, combining different RES sources, increasing the flexibility of the HB process, or developing new electrochemical ammonia synthesis processes [25], [152], [153].

Regarding ammonia production costs, estimates of the LCOA in literature vary widely, but are generally higher for green ammonia (720-1,400 $/ton) than for grey ammonia (110-340 $/ton), produced with fossil fuels. Green ammonia LCOA is predicted to decrease (310-610 $/ton) by 2050 [153], due to economies of scale, renewable energy cost reduction, increased flexibility of the Haber-Bosch synthesis loop, and other solutions to minimize hydrogen cost, in addition to dedicated policies [78], [153].

Several studies have investigated the LCOA. Nayak-Luke et al [154] assessed the viability of islanded green ammonia production, suggesting that the LCOA of 473 $/ton in 2020 can be reduced to 310 $/ton by 2030 in sites with optimal production. They suggest that the revenue of the plant could be increased by selling byproducts such as oxygen, argon, and excess hydrogen. Similar results are obtained in the analysis by Cesaro et al [155], which estimated an LCOA of less than 400 $/ton by 2040. Additionally, a strong key driver for ammonia cost reduction is the minimization of the cost of electricity that drives the process.

Optimization models are employed to design plants and schedule operations. Among them, MILP is widely used to minimize ammonia production costs. Yu et al [156] studied green ammonia production in isolated systems by formulating a mixed integer linear fractional programming problem to minimize the LCOA. Their study achieved a 43.53% reduction in LCOA by exploiting the flexibility of the ammonia synthesis unit. Edmons et al [157] developed an MILP model to study green ammonia production as a demand-response strategy to mitigate RES fluctuations, including a direct ammonia fuel cell for emergency power delivery. They determined that operational flexibility in the green ammonia plant allows for reducing RES curtailment, thereby improving plant profitability. Zhou et al [75] used a two-step optimization model based on particle swarm optimization and MILP to account for non-linearities in the problem. For the ammonia synthesis loop, they considered a wide partial load range of 30% to 110% and a ramp rate of ±20% to better respond to variations in RES power production, though off-design efficiency variations and component degradation were not included. Their results showed

a promising reduction in LCOA from an inflexible scenario, where the LCOA is calculated at 549 $/ton, to a multi-stable flexible scenario with an LCOA of 475 $/ton. Smith and Torrente-Murciano [158] determined that green ammonia costs strongly depend on seasonal variability, production scale, and plant flexibility. In their study, they compared different ammonia synthesis technologies, from conventional Haber-Bosch to electrochemical processes. By employing a MILP optimization model, they determined that flexible operations allow for a drastic reduction and even elimination of buffer storage. Salmon et al [159] determined that further increasing the flexibility of conventional HB processes, reducing the minimum operating rate from 60% to 20%, would not result in significantly reduced LCOA, even in future scenarios. In combination with MILP optimization, they determined that operating with imperfect weather forecasts is feasible when employing model predictive control techniques.

With increased integration of renewable energy in the grid energy mix, specific challenges arise regarding the balancing of production and demand. Often, excess energy that cannot be stored must be curtailed. Therefore, the relationship between RES curtailment, system component optimization, and operational strategies needs extended research. In this regard, research has been carried out by Zhao et al [160], which studied green ammonia production as a way to reduce power curtailment in China, estimating an LCOA of 820 $/ton, by means of MILP optimization. They also suggested that oxygen synergy, generated as a byproduct of electrolysis and nitrogen separation, could reduce LCOA by about 100 $/ton. In their work, Laimon and Goh [161] explored the use of curtailed renewable energy as a primary source for green ammonia production in Jordan. Their analysis was carried out, including the curtailment in the capacity factor calculation, and the added revenue coming from the commercialization of byproducts like oxygen and rare gases. The LCOA, calculated at 600 $/ton, can be reduced to about 400 $/ton by utilizing oxygen and argon. A recent study by Smith and Torrente-Murciano [162] investigates the relation between renewable curtailment and green ammonia production costs, discovering that exploiting all curtailed energy from intermittent sources does not directly translate to minimization of the LCOA. In fact, utilizing all curtailed energy requires large hydrogen storage, which drastically increases costs. Increasing the ramping range of the HB process and combining solar and wind can provide beneficial effects to reduce the LCOA.

Many of these studies, where ammonia is produced from RES, still assume that sales of surplus energy to the grid are always possible. Thus, the revenue from energy sales to the grid is used to reduce the value of the LCOA. However, an increasing share of energy from RES is subject to curtailment, and this revenue decreases [162].

5.5.1 Green ammonia production plant

Figure 40 shows a graphical representation of the plant components, including energy and mass flows. The plant includes a PV system, serving as the primary energy source, a Lithium-ion BESS for electricity storage, a PEM water electrolyzer unit (EL) for hydrogen production, a low-pressure (30 bar) Hydrogen Storage System (HSS) tank, a

hydrogen compressor, an ammonia synthesis unit (HB), and an ASU for nitrogen production. The PV system can power the plant components, charge the BESS, or transfer electricity into the grid. Ammonia is produced using only water and air, and surplus electricity can be sent to the grid. Hydrogen produced by the EL unit can be directly fed to the HB reactor or stored in the HSS. Both the BESS and the HSS, therefore, provide operational flexibility by storing excess production, thus reducing the plant's operational dependency on fluctuating RES power production. This allows for a partial decoupling of green ammonia production from the variable output of the PV system.

In this analysis, the HB unit is modelled as operating at fixed nominal conditions. While recent research explores the potential for flexible operation [74], [159], [163], this study adopts a conservative approach due to the lack of comprehensive experimental validation and modelling data regarding the part-load behavior of Haber-Bosch reactors [77]. The intermittent nature of RES requires new and flexible Haber-Bosch processes capable of operating efficiently under varying power conditions. Conversely, traditional Haber-Bosch plants are designed for continuous operation at high capacity, making them inherently inflexible. Operational flexibility can be achieved by controlling the H_2 to N_2 ratio, by adjusting the concentration of inert gases in the synthesis loop, by varying the total mass feed flow rate, and to a lesser extent by managing other process variables [72].

The EL unit consists of several 1 MW electrolyzer modules connected in parallel, modelled according to a commercial Proton OnSite M Series PEM electrolyzer [164]. This modularity allows for operating only one electrolyzer at partial load, thereby minimizing off-design operations and reducing overall degradation.

The HSS is designed to operate at the same pressure level as the electrolyzer (30 bar) to minimize storage costs. Optimizing the components scheduling allows for minimizing the storage size, requiring only a small hydrogen buffer to decouple EL and HB operations. Since the HB unit operates at approximately 200 bar, hydrogen compression is required. However, hydrogen compression and nitrogen production contribute to about 6% of the total energy consumption of the HB unit.

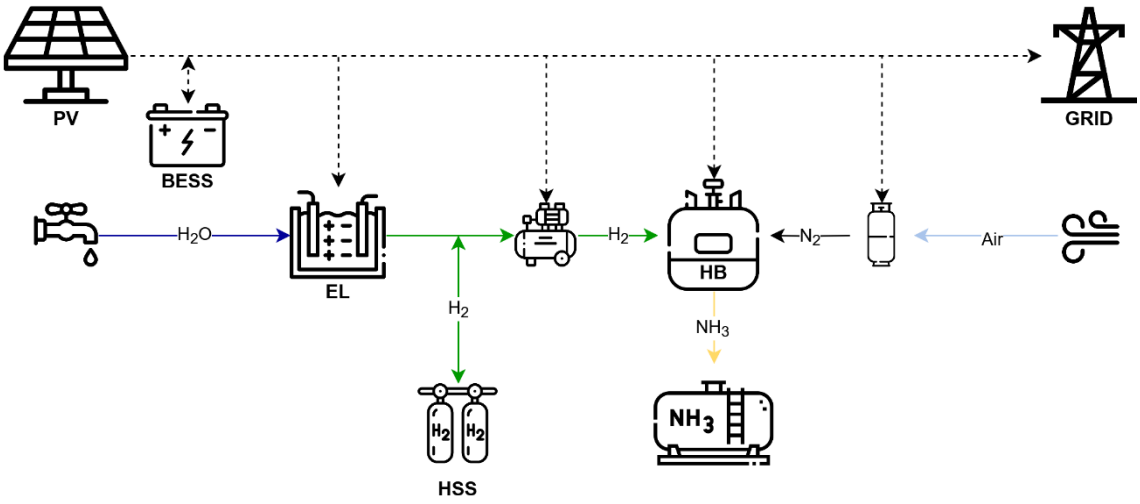

Figure 40. Green ammonia production plant.

5.5.2 Modeling and parameters

A MILP model was developed to optimize the size and scheduling of the plant components. The model aims to minimize the total system cost over its lifetime while determining both the optimal sizing and the optimal hourly operational strategy of each component of the plant. This is done to meet a predefined ammonia production target (1 kton) while minimizing the LCOA. The model is characterized by an optimization horizon of 8,760 hours (1 year) with a time step of 1 hour. The model was implemented using the General Algebraic Modeling System (GAMS) software, version 39.3.0 [91] and employing the CPLEX solver.

Decision variables include power dispatch from the PV plant to various components, the number of active electrolyzer units, BESS charge and discharge cycle scheduling, HB operation, and the respective loads of the components. To avoid residual energy associated with the BESS and hydrogen storage at the end of the optimization horizon, the initial and final storage units' state of charge must be the same.

To minimize LCOA, considering that the annual ammonia production in the study is a fixed target, the objective function minimizes the Net Present Cost (NPC) of the system over the plant lifetime of 20 years, accounting for the discount rate (5%) [92]. To simulate the effects of component degradation, especially for the electrochemical degradation of the electrolyzer stacks, the model considers a linear increase in OPEX of 2.5% per year applied to all components. This economic approach follows the physical degradation of the system, accounting for the progressive loss of efficiency and therefore for the increase in maintenance costs required to maintain the performance of the system over its lifetime. When considering the additional revenue from the sale of electricity to the grid, the adjusted LCOA is calculated by subtracting the revenue generated per unit mass of ammonia produced from the LCOA calculated based on the NPC.

Table 15 summarizes the cost assumptions of the study. Prices originally reported in dollars were converted to euros with an exchange rate of 0.89 $/€ [165].

Table 15. Cost summary for the components of the plant.

		Unit	Value	Reference
CAPEX	PV	€/kW	740	[74]
	BESS	€/kWh	218	[155]
	EL	€/kW	652	[166]
	HSS	€/kg	600	[163]
	HB	€/kW	804	[74]
OPEX	PV	€/kW/year	1.7% CAPEX	[74]
	BESS	€/kWh/year	2% CAPEX	[155]
	EL	€/kW/year	5% CAPEX	[166]
	HSS	€/kg/year	1% CAPEX	[163]
	HB	€/kW/year	2% CAPEX	[74]

The PV power output is calculated using data for a typical meteorological year collected from the NREL database [141] for a location in the south of Sardinia, Italy, and considering the characteristics of a commercial 500 W PV module [167].

The SOC of the BESS is calculated at each time step, considering charge and discharge power and efficiencies of 95% for both charging and discharging. The power and capacity of the BESS are correlated by the C-rate, set to 0.25 [93], and a minimum capacity of 20% of the total capacity is set to prevent excessive degradation. Similarly, the SOC of the HSS is calculated at each time step, considering the mass flow rate of hydrogen produced by the EL unit and consumed by the HB unit.

The EL unit is constituted by several 1 MW electrolyzers, whose part load performance is modelled considering the nonlinear correlation between power and hydrogen production. The nonlinear relationship is implemented in the linear optimization model by employing a PWA function for the linear approximation [94], [95]. The input power and the hydrogen production mass flow rate are linked by means of weight variables at various power breakpoints. Additionally, the power of the electrolyzer is constrained by the minimum and maximum power limits of the operating unit, as well as the Ramp Up (RU_{EL}) and Ramp Down (RD_{EL}) rates.

As previously mentioned, the HB unit is assumed to always operate at design conditions. Its energy consumption is mainly due to the Haber-Bosch synthesis loop, the ASU, and the hydrogen compressor. The energy consumption of the Haber-Bosch unit is calculated based on the reaction's stoichiometric ratio and the specific energy consumption of its main components, equal to 0.144 MWh/tonNH_3 for the Haber-Bosch loop and 0.243 MWh/tonN_2 for the ASU [157], while the energy consumption of the compressor is calculated using its mathematical model.

In this analysis, the components of the plant are sized and operated through an optimization aimed at minimizing the LCOA. This optimization is performed for two curtailment scenarios, differentiated by the economic value assigned, throughout the entire lifetime of the system, to the surplus photovoltaic production. In the Fixed Value scenario, grid feed-ins are valued, over the entire plant lifetime, at the current (2025) LCOE of the photovoltaic technology (51.7 €/MWh [168]). In the Zero Value scenario, grid feed-ins generate no revenue. Both cases represent possible scenarios of curtailment: in the former, it is assumed that policy mechanisms support PV deployment by guaranteeing producers at least the current marginal cost of the technology, which is the LCOE; in the latter (extreme) case, it is assumed that the ongoing decline in the market value of PV electricity continues until reaching a lower bound of 0 €/MWh for all feed-ins. Negative prices are not considered here, as they typically result from speculative behaviors linked to incentive schemes. The Fixed Value scenario allows the green ammonia producer to obtain revenue from electricity sales, enabling a reduction in the plant's LCOA, while the Zero Value scenario does not.

5.5.3 Energy performance

Table 16 summarizes the component sizes obtained by solving the optimization problem. The primary energy is provided by an 8.7 MW PV plant, which generates 13,207 MWh of energy annually. The other components are sized accordingly: a 4 MW electrolyzer provides the required hydrogen to the 1 MW HB unit. The optimized scheduling allows for minimizing the size of the HSS. A capacity of approximately 294.4 kg of hydrogen is required to balance mismatches between hydrogen production from the EL and usage by the HB. The HSS (185.3 m^3 at 25 °C) is designed to operate within a pressure range of 10–30 bar, where the lower limit corresponds to the minimum pressure required for compressor operation [169], and the upper limit represents the EL output pressure. In total, the stored hydrogen mass amounts to 444.3 kg. In addition, a 0.75 MW/3 MWh BESS provides short-term electrical buffering.

Table 16. Optimized component sizes.

Component	Unit	Value
PV plant	MW	8.7
EL	MW	4
HB	MW	1
BESS	MW / MWh	0.75 / 3
HSS	kg / m^3	444.3 / 185.3

The optimization process yielded a system configuration that minimizes LCOA by appropriately sizing plant components and managing energy and material flows. Since the minimization of the NPC is the objective of the optimization, component sizes and plant management are identical in both scenarios. What differs between the two scenarios is the revenue obtainable from surplus electricity feed-ins.

Table 17 summarizes the results of the optimized energy and mass productions. Out of the total 13,207 MWh of PV energy production, 9,192 MWh are required by the EL unit for hydrogen production, and 3,090 MWh by the HB unit, achieving a total ammonia production of 1 kton. Ultimately, the plant utilizes most of the primary energy from the PV plant, with a surplus limited to about 6.4% of the total energy generation.

Table 17. Optimized energy and mass production.

Component	Unit	Value
PV energy production	MWh	13,207
EL energy consumption	MWh	9,192
HB energy consumption	MWh	3,090
Energy to the grid	%	6.4
NH_3 production	ton/year	1,000

Figure 41 represents the annual energy flows, including losses, of the green ammonia plant, from PV energy generation to the final ammonia product. Energy in the form of hydrogen and ammonia is calculated considering Lower Heating Values of 120 MJ/kg and 18.6 MJ/kg, respectively. PV production is mostly provided directly to each component of the plant, while only a small share (about 6%) is stored in the BESS, later provided to the EL and HB units. Due to its high efficiency, only a small portion of BESS energy is lost during cyclical charging and discharging. As expected, the electrolyzer is the most energy-intensive component, consuming approximately 70% of all PV generation, with significant conversion losses resulting in an efficiency of 64%. The HB unit requires 3,090 MWh of electrical energy and 5,885 MWh in the form of hydrogen. The HB process yields 5,170 MWh of energy associated with a mass of ammonia of 1 kton. Lastly, surplus PV generation results in about 845 MWh of grid feed-ins. Overall, the plant is characterized by a first law efficiency of 45.5%.

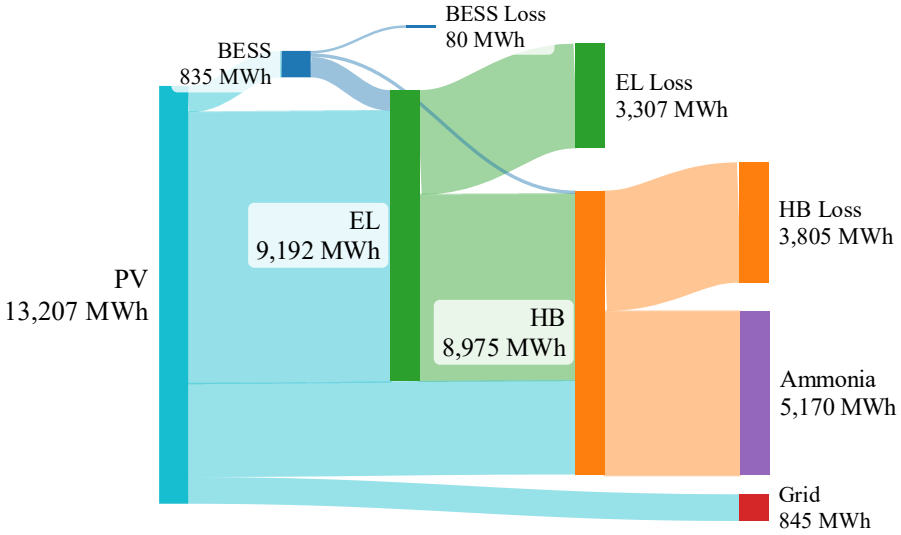

Figure 41. Energy flows for the green ammonia plant.

5.5.4 Economic performance

The economic performance of the plant in the two scenarios is reported in Table 18. The optimization leads to a minimum LCOA of 1,038 €/ton, corresponding to a total capital cost of approximately 9.87 M€ and yearly expenses of about 250 k€. The Fixed Value scenario, however, allows for an additional revenue of about 43.6 k€/year (around 17% of the yearly OPEX of the system) from selling surplus electricity at the LCOE price. The additional revenue of the Fixed Value scenario allows the Adjusted LCOA to be reduced to 995 €/ton, about 4% lower than the LCOA. No additional revenue is reported in the Zero Value scenario, as the value of feed-ins is zero; therefore, its adjusted LCOA coincides with LCOA. It's important to note that relying on the adjusted LCOA rather than on the LCOA might lead to an underestimation of the investment risk.

Table 18. Economic performance comparison of the two scenarios considered.

	Unit	Fixed Value scenario	Zero Value scenario
LCOA	€/ton	1,038	1,038
Adjusted LCOA	€/ton	995	1,038
CAPEX tot	M€	9.87	9.87
OPEX tot	k€/year	250	250
Revenue from grid feed-ins	k€/year	43.6	0

A breakdown of the costs of the components is reported in Figure 42. Figure 42a shows that the PV plant is responsible for more than half of the total capital investment. Among the components directly involved in ammonia production, electrolysis is vastly the most energy-intensive process. Together, the PV plant and the EL unit account for over 84%

of the total initial investment. In accordance with the literature, the economic feasibility of green ammonia is highly dependent on the costs and efficiency of PV and electrolyzer technologies. In fact, renewable energy and hydrogen production costs contribute to the increase in the levelized cost of green ammonia production when compared to conventional grey ammonia processes. In contrast, the HB unit itself constitutes only about 7% of the total capital costs. The buffer units, BESS and HSS, account for about 9% of the total investment costs. Due to optimized operational scheduling, the HSS investment cost is limited. Figure 42b shows that the EL unit is the largest contributor to operational costs (approximately 52%), followed by the PV plant. The operational costs of all other components are relatively low. This cost distribution highlights that the economic viability of green ammonia is primarily driven by the costs associated with renewable electricity generation and hydrogen production via electrolysis.

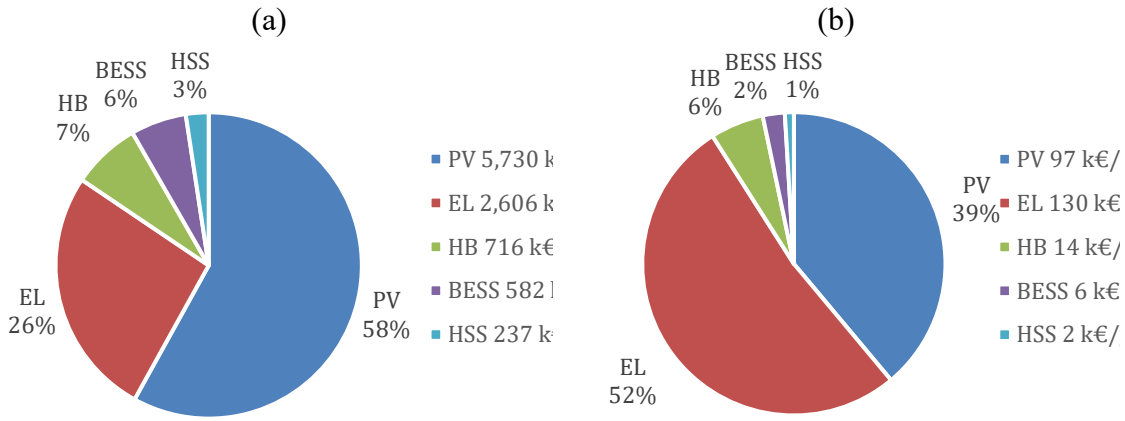

Figure 42. Breakdown of the total capital (a) and operational costs (b).

5.5.5 Operation scheduling

Figure 43a shows the monthly and cumulative ammonia production profile over the year for the optimized system. The monthly production clearly exhibits a seasonal trend, reflecting the variability of PV energy generation. Ammonia production is low during the winter months (43.4 ton in January) and increases steadily to reach peak production from June to August (119.1 ton in July). However, the plant operational strategy, optimized with the MILP model, allows for adapting this fluctuating energy input to reach the annual target production while maximizing ammonia output when PV energy is abundant and maintaining a limited production when PV production is low. The BESS and HSS storage units allow for partial decoupling of RES and ammonia production. In fact, the cumulative production shows an almost steady increase throughout the year, even if the slope of the curve is steeper during summer months and flatter during winter months. This profile shows how the optimized system is capable of meeting the annual production target while maintaining a nearly stable production, smoothing intermittent RES generation.

Figure 43b shows the monthly grid feed-in derived from energy surplus, as well as the revenue generated in the Fixed Value scenario. Electricity surplus exported to the grid exhibits a strong seasonal trend, depending on the correlation between PV production and

ammonia plant operations. Monthly revenues vary accordingly, reaching the highest values during the summer. The additional income of the Fixed Value scenario is therefore mostly concentrated in months with high solar availability, after ammonia production targets are met.

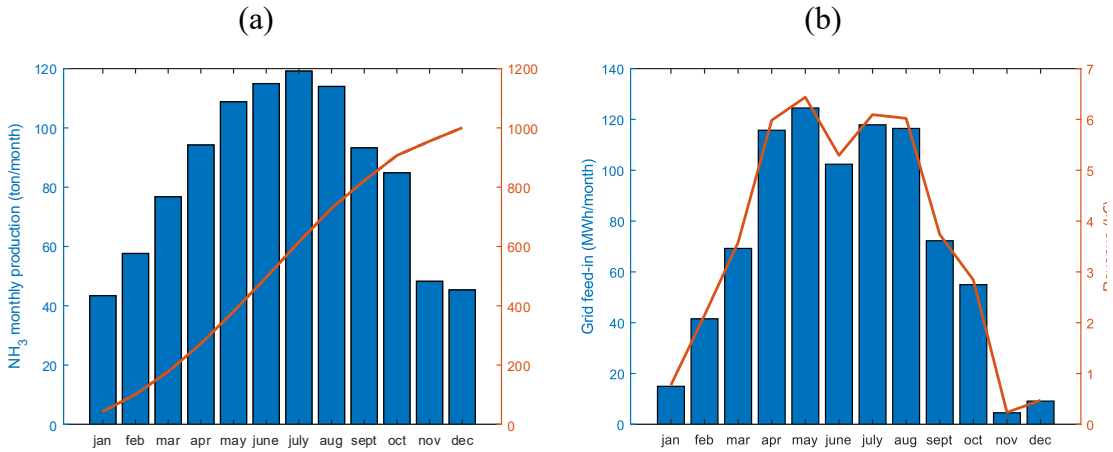

Figure 43. (a) monthly and cumulative ammonia production profile and (b) monthly grid feed-ins and revenue for the Fixed Value scenario.

5.5.6 Synthesis and comparison of the findings

The analyses of the PV-H2-CAES and FPV-PHES-AEM systems approach green hydrogen integration in diverse ways: the former uses on-site hydrogen production for decarbonizing a mechanical energy storage system, the latter uses surplus electricity to provide green hydrogen to local communities.

In the PV-H2-CAES configuration, hydrogen is primarily an energy vector used as a carbon-free fuel to enable the dispatchability of renewable energy stored as mechanical energy. The optimization yielded a system efficiency of approximately 62%, achieved with specific component size ratios of $\dot{E}_{PEM}/\dot{E}_{PV}$ of $0.7-0.9$ and $\dot{E}_{C}/\dot{E}_{PV}$ of $0.20-0.25$.

Conversely, in the FPV-PHES-AEM system, the electrolyzer allows for increasing the flexibility of the system and produces a valuable chemical by exploiting surplus electricity. Maximizing self-consumption is critical to allow for optimized dispatch. In a scenario of high self-consumption greater than 0.99, green hydrogen can be produced in large quantities at a competitive LCOH.

While green hydrogen is employed in diverse ways, the core conclusion in both studies is that strategic integration allows for mitigating VRES curtailment and enhancing the techno-economic performance of renewable energy systems.

The green ammonia plant represents a configuration where hydrogen is not an energy carrier for the grid but instead the primary feedstock for a chemical synthesis process. Consequently, the optimization is directed to minimize the production cost for the chemicals. The analysis shows that this requires a different operational approach compared to the other integrated configurations, where BESS and HSS are sized for short-

term operational decoupling and not for large-scale storage. This enables the steady-state operation of the Haber-Bosch, effectively decoupling ammonia production from the variable PV input. This approach achieves an overall system efficiency of 45.5% and achieves an LCOA of 995 €/ton.

Chapter 6

Conclusions and future work

The global transition towards a sustainable energy sector is one of the most significant challenges of the current research landscape. Mitigating the impacts of climate change requires a transformation of global energy systems towards carbon-free technological solutions. These changes are largely dependent on the vast deployment of renewable sources. However, the inherently intermittent nature of VRES poses significant challenges to grid stability, leading to energy curtailment and economic inefficiencies. Indeed, as the penetration of VRES continues to increase, large capacity and long duration energy storage technologies will become increasingly more critical for ensuring grid stability and security. Green hydrogen and ammonia offer a potential solution to increase VRES integration and create alternative ways to effectively aid in decarbonizing hard-to-abate sectors such as heavy industry and transport, and energy generation by converting surplus renewable energy into stable chemical energy carriers.

This thesis addressed these critical challenges by investigating the design, optimization, and techno-economic performance of energy systems that integrate VRES generation with the production of green hydrogen and ammonia. Hydrogen and ammonia are considered not only as chemical products but as means to enhance the flexibility of the power grid and mitigate RES curtailment. In the thesis, two principal integration solutions are analyzed: the first focuses on the integration of green hydrogen production and use with mechanical energy storage such as CAES and PHES to provide grid services or produce hydrogen by exploiting surplus generation, while the second investigates a dedicated green ammonia production system. In all configurations, the core is composed of a VRES plant (PV or FPV) powering an electrolyzer unit to produce hydrogen, which can either be utilized as a carbon-free fuel in power generation, distributed to local networks, or used as a feedstock for ammonia production. The integration in energy systems allows for decoupling energy intermittency with final product generation, mitigating RES curtailment and increasing the overall system efficiency. The component models were parameterized and validated considering performance data from commercial technologies and results from the scientific literature. The performance of the integrated systems was evaluated to determine optimal configurations and operational strategies.

A critical issue deriving from vast green hydrogen production was investigated, quantifying the impact of green hydrogen production on freshwater resources, comparing water withdrawal savings for a Power-to-Power hydrogen cycle with fossil fuel-based power generation. Furthermore, the analysis established the viability of seawater electrolysis as an alternative in water-stressed regions, with only a marginal energy penalty for indirect seawater electrolysis, requiring desalination before water splitting.

Two integrated hydrogen systems were analyzed: a PV-H2-CAES system and an FPV-PHES-AEM system. In the integrated PV-H2-CAES system, hydrogen is used to abate the carbon emissions of conventional CAES mechanical storage. The integrated system demonstrated its capacity to provide grid flexibility services, achieving a system efficiency of approximately 62%, reducing PV curtailment to a minimum of 4%, using green hydrogen produced on-site as a carbon-free fuel. An FPV-PHES-AEM system was developed to efficiently exploit surplus production of a floating PV plant, which directly supplies energy to a reconverted pumped hydro facility, to produce green hydrogen. The findings showed that maximizing system self-consumption is crucial for achieving the best economic performance with varying grid curtailment scenarios.

Finally, a dedicated green ammonia production plant was optimized, using a mixed integer linear programming approach. The analysis demonstrated that optimized component size and operation scheduling allow for effective decoupling of green ammonia production throughout the year from the variable PV input. Moreover, this can be achieved with minimal buffer storage, achieving an overall system efficiency of 45.5% and an LCOA of 995 €/ton.

Overall, in this thesis, various configurations were developed and analyzed for cost-effective green hydrogen and ammonia production. The integrated systems allowed for mitigating VRES curtailment, achieving up to 99.2% of energy use, decoupling VRES generation and ammonia production, with an optimized LCOA and energy efficiency.

Given the results in terms of efficiency and economic performance of the analyzed systems, several pathways for future research can be identified. To enhance the economic and technical viability, future work should focus on further improving the thermodynamic and operational efficiency of the integrated systems. This requires improving the part-load performance analysis for the Haber-Bosch process using dynamic models. Improved operational flexibility could allow for better coupling with VRES production. Furthermore, the current analysis focuses on single PV inputs, while further research should consider mixed RES configurations such as PV and wind energy systems, to analyze the performance under smoother input power profiles and evaluate their impact on optimal component sizing and operation scheduling, to further reduce storage size, increase capacity factor, and reduce levelized costs. An additional tool to improve economic performance includes assessing the value of grid ancillary services. This includes incorporating market prices for flexibility services, such as frequency regulation, rapid ramping, and inertia with mechanical storage integration. Finally, the impact of various incentive policies on the final production cost should be considered.

Bibliography

[1] IEA, 'Net Zero Roadmap: A Global Pathway to Keep the 1.5 °C Goal in Reach', IEA, Paris, 2023. [Online]. Available: https://www.iea.org/reports/net-zero-roadmap-a-global-pathway-to-keep-the-15-0c-goal-in-reach

[2] IPCC, 'Climate Change 2023: Synthesis Report. Contribution of Working Groups I, II and III to the Sixth Assessment Report of the Intergovernmental Panel on Climate Change', IPCC, Geneva, 2023. [Online]. Available: doi: 10.59327/IPCC/AR6-9789291691647

[3] M. Kabir *et al.*, 'Climate change due to increasing concentration of carbon dioxide and its impacts on environment in 21st century; a mini review', *Journal of King Saud University - Science*, vol. 35, no. 5, p. 102693, Jul. 2023, doi: 10.1016/j.jksus.2023.102693.

[4] UNFCCC, 'The Paris Agreement', Paris Climate Change Conference - November 2015, 2018.

[5] IRENA, 'NDCs and renewable energy targets in 2023: Tripling renewable power by 2030', International Renewable Energy Agency, Abu Dhabi, 2023.

[6] IEA, 'Global Energy Review 2025', IEA, Paris, 2025. [Online]. Available: https://www.iea.org/reports/global-energy-review-2025

[7] European Union (EU), 'Long-term low greenhouse gas emission development strategy of the European Union and its Member States'. 2020. [Online]. Available: https://unfccc.int/documents/210328

[8] European Commission: Directorate-General for Research and Innovation, 'European Green Deal – Research & innovation call'. Publications Office of the European Union, 2021. [Online]. Available: https://data.europa.eu/doi/10.2777/33415

[9] European Commission, '"Fit for 55": delivering the EU's 2030 Climate Target on the way to climate neutrality'. Communication from the Commission to the European Parliament, the Council, the European Economic and Social Committee and the Committee of the Regions, 2021.

[10] A. I. Osman *et al.*, 'Cost, environmental impact, and resilience of renewable energy under a changing climate: a review', *Environ Chem Lett*, vol. 21, no. 2, pp. 741–764, Apr. 2023, doi: 10.1007/s10311-022-01532-8.

[11] IEA, 'Achieving Net Zero Heavy Industry Sectors in G7 Members', IEA, Paris, 2022. [Online]. Available: https://www.iea.org/reports/achieving-net-zero-heavy-industry-sectors-in-g7-members

[12] S. Impram, S. V. Nese, and B. Oral, 'Challenges of renewable energy penetration on power system flexibility: A survey', *Energy Strategy Reviews*, vol. 31, p. 100539, Sep. 2020, doi: 10.1016/j.esr.2020.100539.

[13] R. Shah, N. Mithulananthan, R. C. Bansal, and V. K. Ramachandaramurthy, 'A review of key power system stability challenges for large-scale PV integration', *Renewable and Sustainable Energy Reviews*, vol. 41, pp. 1423–1436, Jan. 2015, doi: 10.1016/j.rser.2014.09.027.

[14] L. Bird *et al.*, 'Wind and solar energy curtailment: A review of international experience', *Renewable and Sustainable Energy Reviews*, vol. 65. Elsevier Ltd, pp. 577–586, Nov. 2016. doi: 10.1016/j.rser.2016.06.082.

[15] CAISO, ‘California ISO’. 2024. [Online]. Available: http://www.caiso.com/Pages/default.aspx
[16] U. Helman, B. Kaun, and J. Stekli, ‘Development of Long-Duration Energy Storage Projects in Electric Power Systems in the United States: A Survey of Factors Which Are Shaping the Market’, *Frontiers in Energy Research*, vol. 8, Nov. 2020, doi: 10.3389/fenrg.2020.539752.
[17] IEA, ‘Global Hydrogen Review 2023’, Paris, 2023. Accessed: Mar. 12, 2024. [Online]. Available: https://www.iea.org/reports/global-hydrogen-review-2023
[18] A. M. Oliveira, R. R. Beswick, and Y. Yan, ‘A green hydrogen economy for a renewable energy society’, *Current Opinion in Chemical Engineering*, vol. 33, p. 100701, Sep. 2021, doi: 10.1016/j.coche.2021.100701.
[19] ETN Global, ‘Hydrogen deployment in centralised power generation’. [Online]. Available: https://etn.global/wp-content/uploads/2022/06/H2-deployment-in-centralised-power-generation-techno-economic-study-April2022.pdf
[20] M. Wappler, D. Unguder, X. Lu, H. Ohlmeyer, H. Teschke, and W. Lueke, ‘Building the green hydrogen market – Current state and outlook on green hydrogen demand and electrolyzer manufacturing’, *International Journal of Hydrogen Energy*, vol. 47, no. 79, pp. 33551–33570, Sep. 2022, doi: 10.1016/j.ijhydene.2022.07.253.
[21] S. S. Kumar and H. Lim, ‘An overview of water electrolysis technologies for green hydrogen production’, *Energy Reports*, vol. 8, pp. 13793–13813, Nov. 2022, doi: 10.1016/j.egyr.2022.10.127.
[22] D. Tang *et al.*, ‘State-of-the-art hydrogen generation techniques and storage methods: A critical review’, *Journal of Energy Storage*, vol. 64, p. 107196, Aug. 2023, doi: 10.1016/j.est.2023.107196.
[23] D. Hardie, E. A. Charles, and A. H. Lopez, ‘Hydrogen embrittlement of high strength pipeline steels’, *Corrosion Science*, vol. 48, no. 12, pp. 4378–4385, Dec. 2006, doi: 10.1016/j.corsci.2006.02.011.
[24] D. R. MacFarlane *et al.*, ‘A Roadmap to the Ammonia Economy’, *Joule*, vol. 4, no. 6, pp. 1186–1205, Jun. 2020, doi: 10.1016/j.joule.2020.04.004.
[25] IEA, ‘Ammonia Technology Roadmap’. IEA, 2021. [Online]. Available: https://www.iea.org/reports/ammonia-technology-roadmap
[26] N. Salmon and R. Bañares-Alcántara, ‘Green ammonia as a spatial energy vector: a review’, *Sustainable Energy & Fuels*, vol. 5, no. 11, pp. 2814–2839, 2021, doi: 10.1039/D1SE00345C.
[27] O. Edenhofer *et al.*, Eds., *Renewable Energy Sources and Climate Change Mitigation: Special Report of the Intergovernmental Panel on Climate Change*, 1st ed. Cambridge University Press, 2011. doi: 10.1017/cbo9781139151153.
[28] Fraunhofer Institute for Solar Energy Systems ISE, ‘Annual report 2024/25: Research for the energy transition’, 2025. [Online]. Available: https://www.ise.fraunhofer.de/en/publications.html
[29] IEA, ‘Renewables 2024’, Paris, 2024. [Online]. Available: https://www.iea.org/reports/renewables-2024
[30] IRENA, ‘Hydropower’, 2012. [Online]. Available: https://www.irena.org/Publications/2015/Feb/Hydropower
[31] J. Mitali, S. Dhinakaran, and A. A. Mohamad, ‘Energy storage systems: a review’, *Energy Storage and Saving*, vol. 1, no. 3, pp. 166–216, Sep. 2022, doi: 10.1016/j.enss.2022.07.002.

[32] J. M. M. Arcos and D. M. F. Santos, ‘The Hydrogen Color Spectrum: Techno-Economic Analysis of the Available Technologies for Hydrogen Production’, *Gases*, vol. 3, no. 1, pp. 25–46, Feb. 2023, doi: 10.3390/gases3010002.
[33] J. Incer-Valverde, A. Korayem, G. Tsatsaronis, and T. Morosuk, ‘“Colors” of hydrogen: Definitions and carbon intensity’, *Energy Conversion and Management*, vol. 291, p. 117294, Sep. 2023, doi: 10.1016/j.enconman.2023.117294.
[34] A. Ajanovic, M. Sayer, and R. Haas, ‘The economics and the environmental benignity of different colors of hydrogen’, *International Journal of Hydrogen Energy*, vol. 47, no. 57, pp. 24136–24154, Jul. 2022, doi: 10.1016/j.ijhydene.2022.02.094.
[35] A. Züttel, ‘Materials for hydrogen storage’, *Materials Today*, vol. 6, no. 9, pp. 24–33, Sep. 2003, doi: 10.1016/S1369-7021(03)00922-2.
[36] E. I. Epelle *et al.*, ‘Perspectives and prospects of underground hydrogen storage and natural hydrogen’, *Sustainable Energy Fuels*, vol. 6, no. 14, pp. 3324–3343, 2022, doi: 10.1039/D2SE00618A.
[37] B. Sakintuna, F. Lamaridarkrim, and M. Hirscher, ‘Metal hydride materials for solid hydrogen storage: A review☆’, *International Journal of Hydrogen Energy*, vol. 32, no. 9, pp. 1121–1140, Jun. 2007, doi: 10.1016/j.ijhydene.2006.11.022.
[38] IRENA, ‘Green Hydrogen Cost Reduction: Scaling up Electrolysers to Meet the 1.5^0C Climate Goal’, International Renewable Energy Agency, Abu Dhabi, 2020.
[39] IEA, ‘Ammonia Technology Roadmap’, IEA, Paris, 2021. [Online]. Available: https://www.iea.org/reports/ammonia-technology-roadmap
[40] M. Müller, M. Pfeifer, D. Holtz, and K. Müller, ‘Comparison of green ammonia and green hydrogen pathways in terms of energy efficiency’, *Fuel*, vol. 357, p. 129843, Feb. 2024, doi: 10.1016/j.fuel.2023.129843.
[41] M. Aziz, A. T. Wijayanta, and A. B. D. Nandiyanto, ‘Ammonia as Effective Hydrogen Storage: A Review on Production, Storage and Utilization’, *Energies*, vol. 13, no. 12, p. 3062, Jun. 2020, doi: 10.3390/en13123062.
[42] M. Budt, D. Wolf, R. Span, and J. Yan, ‘A review on compressed air energy storage: Basic principles, past milestones and recent developments’, *Applied Energy*, vol. 170, pp. 250–268, May 2016, doi: 10.1016/j.apenergy.2016.02.108.
[43] M. Nakhamkin *et al.*, ‘AEC 110 MW CAES Plant: Status of Project’, *Journal of Engineering for Gas Turbines and Power*, vol. 114, no. 4, pp. 695–700, Oct. 1992, doi: 10.1115/1.2906644.
[44] F. Crotogino, ‘Huntorf CAES: More than 20 Years of Successful Operation’. 2001.
[45] A. Blakers, M. Stocks, B. Lu, and C. Cheng, ‘A review of pumped hydro energy storage’, *Progress in Energy*, vol. 3, no. 2, p. 022003, Apr. 2021, doi: 10.1088/2516-1083/abeb5b.
[46] M. Kamran and M. Turzyński, ‘Exploring hydrogen energy systems: A comprehensive review of technologies, applications, prevailing trends, and associated challenges’, *Journal of Energy Storage*, vol. 96, p. 112601, Aug. 2024, doi: 10.1016/j.est.2024.112601.
[47] D. Henkensmeier, M. Najibah, C. Harms, J. Žitka, J. Hnát, and K. Bouzek, ‘Overview: State-of-the Art Commercial Membranes for Anion Exchange Membrane Water Electrolysis’, *Journal of Electrochemical Energy Conversion and Storage*, vol. 18, no. 2, May 2021, doi: 10.1115/1.4047963.
[48] M. Kim, D. Lee, M. Qi, and J. Kim, ‘Techno-economic analysis of anion exchange membrane electrolysis process for green hydrogen production under uncertainty’,

Energy Conversion and Management, vol. 302, p. 118134, Feb. 2024, doi: 10.1016/j.enconman.2024.118134.
[49] F. Gambou, D. Guilbert, M. Zasadzinski, and H. Rafaralahy, 'A Comprehensive Survey of Alkaline Electrolyzer Modeling: Electrical Domain and Specific Electrolyte Conductivity', *Energies*, vol. 15, no. 9, p. 3452, May 2022, doi: 10.3390/en15093452.
[50] S. W. Sharshir, A. Joseph, M. M. Elsayad, A. A. Tareemi, A. W. Kandeal, and M. R. Elkadeem, 'A review of recent advances in alkaline electrolyzer for green hydrogen production: Performance improvement and applications', *International Journal of Hydrogen Energy*, vol. 49, pp. 458–488, Jan. 2024, doi: 10.1016/j.ijhydene.2023.08.107.
[51] O. Ulleberg, 'Modeling of advanced alkaline electrolyzers: a system simulation approach', *International Journal of Hydrogen Energy*, vol. 28, no. 1, pp. 21–33, Jan. 2003, doi: 10.1016/S0360-3199(02)00033-2.
[52] D. S. Falcão and A. M. F. R. Pinto, 'A review on PEM electrolyzer modelling: Guidelines for beginners', *Journal of Cleaner Production*, vol. 261, p. 121184, Jul. 2020, doi: 10.1016/j.jclepro.2020.121184.
[53] H. Zhang, S. Su, G. Lin, and J. Chen, 'Efficiency Calculation and Configuration Design of a PEM Electrolyzer System for Hydrogen Production', *International Journal of Electrochemical Science*, vol. 7, no. 5, pp. 4143–4157, 2012, doi: 10.1016/S1452-3981(23)19527-7.
[54] Á. Hernández-Gómez, V. Ramirez, and D. Guilbert, 'Investigation of PEM electrolyzer modeling: Electrical domain, efficiency, and specific energy consumption', *International Journal of Hydrogen Energy*, vol. 45, no. 29, pp. 14625–14639, May 2020, doi: 10.1016/j.ijhydene.2020.03.195.
[55] I. Vincent and D. Bessarabov, 'Low cost hydrogen production by anion exchange membrane electrolysis: A review', *Renewable and Sustainable Energy Reviews*, vol. 81, pp. 1690–1704, Jan. 2018, doi: 10.1016/j.rser.2017.05.258.
[56] K. F. L. Hagesteijn, S. Jiang, and B. P. Ladewig, 'A review of the synthesis and characterization of anion exchange membranes', *J Mater Sci*, vol. 53, no. 16, pp. 11131–11150, Aug. 2018, doi: 10.1007/s10853-018-2409-y.
[57] M. A. Hickner, A. M. Herring, and E. B. Coughlin, 'Anion exchange membranes: Current status and moving forward', *J Polym Sci B Polym Phys*, vol. 51, no. 24, pp. 1727–1735, Dec. 2013, doi: 10.1002/polb.23395.
[58] I. Vincent, A. Kruger, and D. Bessarabov, 'Development of efficient membrane electrode assembly for low cost hydrogen production by anion exchange membrane electrolysis', *International Journal of Hydrogen Energy*, vol. 42, no. 16, pp. 10752–10761, Apr. 2017, doi: 10.1016/j.ijhydene.2017.03.069.
[59] H. Liu, M. Yu, X. Tong, Q. Wang, and M. Chen, 'High Temperature Solid Oxide Electrolysis for Green Hydrogen Production', *Chem. Rev.*, vol. 124, no. 18, pp. 10509–10576, Sep. 2024, doi: 10.1021/acs.chemrev.3c00795.
[60] M. Ni, M. Leung, and D. Leung, 'Technological development of hydrogen production by solid oxide electrolyzer cell (SOEC)', *International Journal of Hydrogen Energy*, vol. 33, no. 9, pp. 2337–2354, May 2008, doi: 10.1016/j.ijhydene.2008.02.048.
[61] D. Ferrero, A. Lanzini, M. Santarelli, and P. Leone, 'A comparative assessment on hydrogen production from low- and high-temperature electrolysis', *International Journal of Hydrogen Energy*, vol. 38, no. 9, pp. 3523–3536, Mar. 2013, doi: 10.1016/j.ijhydene.2013.01.065.

[62] A. Pandiyan, A. Uthayakumar, R. Subrayan, S. W. Cha, and S. B. Krishna Moorthy, ‘Review of solid oxide electrolysis cells: a clean energy strategy for hydrogen generation’, *Nanomaterials and Energy*, vol. 8, no. 1, pp. 2–22, Jun. 2019, doi: 10.1680/jnaen.18.00009.
[63] V. Menon, V. M. Janardhanan, and O. Deutschmann, ‘A mathematical model to analyze solid oxide electrolyzer cells (SOECs) for hydrogen production’, *Chemical Engineering Science*, vol. 110, pp. 83–93, May 2014, doi: 10.1016/j.ces.2013.10.025.
[64] IRENA and Bluerisk, ‘Water for hydrogen production’, International Renewable Energy Agency, Bluerisk, Abu Dhabi, United Arab Emirates, 2023.
[65] M. A. Khan *et al.*, ‘Seawater electrolysis for hydrogen production: a solution looking for a problem?’, *Energy Environ. Sci.*, vol. 14, no. 9, pp. 4831–4839, 2021, doi: 10.1039/D1EE00870F.
[66] P. Farràs, P. Strasser, and A. J. Cowan, ‘Water electrolysis: Direct from the sea or not to be?’, *Joule*, vol. 5, no. 8, pp. 1921–1923, Aug. 2021, doi: 10.1016/j.joule.2021.07.014.
[67] R. R. Beswick, A. M. Oliveira, and Y. Yan, ‘Does the Green Hydrogen Economy Have a Water Problem?’, *ACS Energy Lett.*, vol. 6, no. 9, pp. 3167–3169, Sep. 2021, doi: 10.1021/acsenergylett.1c01375.
[68] J. N. Hausmann, R. Schlögl, P. W. Menezes, and M. Driess, ‘Is direct seawater splitting economically meaningful?’, *Energy Environ. Sci.*, vol. 14, no. 7, pp. 3679–3685, 2021, doi: 10.1039/D0EE03659E.
[69] S. Dresp, F. Dionigi, M. Klingenhof, and P. Strasser, ‘Direct Electrolytic Splitting of Seawater: Opportunities and Challenges’, *ACS Energy Lett.*, vol. 4, no. 4, pp. 933–942, Apr. 2019, doi: 10.1021/acsenergylett.9b00220.
[70] J. Humphreys, R. Lan, and S. Tao, ‘Development and Recent Progress on Ammonia Synthesis Catalysts for Haber–Bosch Process’, *Advanced Energy and Sustainability Research*, vol. 2, no. 1, p. 2000043, 2021, doi: 10.1002/aesr.202000043.
[71] G. Chehade and I. Dincer, ‘Progress in green ammonia production as potential carbon-free fuel’, *Fuel*, vol. 299, p. 120845, Sep. 2021, doi: 10.1016/j.fuel.2021.120845.
[72] I. I. Cheema and U. Krewer, ‘Operating envelope of Haber–Bosch process design for power-to-ammonia’, *RSC Adv.*, vol. 8, no. 61, pp. 34926–34936, 2018, doi: 10.1039/C8RA06821F.
[73] O. A. Ojelade, S. F. Zaman, and B.-J. Ni, ‘Green ammonia production technologies: A review of practical progress’, *Journal of Environmental Management*, vol. 342, p. 118348, Sep. 2023, doi: 10.1016/j.jenvman.2023.118348.
[74] J. Armijo and C. Philibert, ‘Flexible production of green hydrogen and ammonia from variable solar and wind energy: Case study of Chile and Argentina’, *International Journal of Hydrogen Energy*, vol. 45, no. 3, pp. 1541–1558, Jan. 2020, doi: 10.1016/j.ijhydene.2019.11.028.
[75] J. Zhou, Z. Zhang, R. Zhang, W. Zhang, G. Xu, and H. Wang, ‘Optimal capacity and multi-stable flexible operation strategy of green ammonia systems: Adapting to fluctuations in renewable energy’, *Energy Conversion and Management*, vol. 314, p. 118720, Aug. 2024, doi: 10.1016/j.enconman.2024.118720.

[76] H. Zhang, L. Wang, J. Van Herle, F. Maréchal, and U. Desideri, 'Techno-economic comparison of green ammonia production processes', *Applied Energy*, vol. 259, p. 114135, Feb. 2020, doi: 10.1016/j.apenergy.2019.114135.
[77] K. Verleysen, A. Parente, and F. Contino, 'How sensitive is a dynamic ammonia synthesis process? Global sensitivity analysis of a dynamic Haber-Bosch process (for flexible seasonal energy storage)', *Energy*, vol. 232, p. 121016, Oct. 2021, doi: 10.1016/j.energy.2021.121016.
[78] C. Smith, A. K. Hill, and L. Torrente-Murciano, 'Current and future role of Haber–Bosch ammonia in a carbon-free energy landscape', *Energy Environ. Sci.*, vol. 13, no. 2, pp. 331–344, 2020, doi: 10.1039/C9EE02873K.
[79] F. B. Juangsa, A. R. Irhamna, and M. Aziz, 'Production of ammonia as potential hydrogen carrier: Review on thermochemical and electrochemical processes', *International Journal of Hydrogen Energy*, vol. 46, no. 27, pp. 14455–14477, Apr. 2021, doi: 10.1016/j.ijhydene.2021.01.214.
[80] R. Zhao *et al.*, 'Recent progress in the electrochemical ammonia synthesis under ambient conditions', *EnergyChem*, vol. 1, no. 2, p. 100011, Sep. 2019, doi: 10.1016/j.enchem.2019.100011.
[81] T. Wu, W. Fan, Y. Zhang, and F. Zhang, 'Electrochemical synthesis of ammonia: Progress and challenges', *Materials Today Physics*, vol. 16, p. 100310, Jan. 2021, doi: 10.1016/j.mtphys.2020.100310.
[82] V. Kyriakou, I. Garagounis, E. Vasileiou, A. Vourros, and M. Stoukides, 'Progress in the Electrochemical Synthesis of Ammonia', *Catalysis Today*, vol. 286, pp. 2–13, 2017, doi: https://doi.org/10.1016/j.cattod.2016.06.014.
[83] J. R. R. A. Martins and A. Ning, *Engineering Design Optimization*. Cambridge University Press, 2021. doi: 10.1017/9781108980647.
[84] G. Chowdhury, M. Haggag, and J. Poortmans, 'How cool is floating PV? A state-of-the-art review of floating PV's potential gain and computational fluid dynamics modeling to find its root cause', *EPJ Photovoltaics*, vol. 14, p. 24, Aug. 2023, doi: 10.1051/epjpv/2023015.
[85] A. G. Vidales, N. C. Millan, and C. Bock, 'Modeling of anion exchange membrane water electrolyzers: The influence of operating parameters', *Chemical Engineering Research and Design*, vol. 194, pp. 636–648, Jun. 2023, doi: 10.1016/j.cherd.2023.05.004.
[86] J. Milewski, G. Guandalini, and S. Campanari, 'Modeling an alkaline electrolysis cell through reduced-order and loss-estimate approaches', *Journal of Power Sources*, vol. 269, pp. 203–211, Dec. 2014, doi: 10.1016/j.jpowsour.2014.06.138.
[87] R. GILLIAM, J. GRAYDON, D. KIRK, and S. THORPE, 'A review of specific conductivities of potassium hydroxide solutions for various concentrations and temperatures', *International Journal of Hydrogen Energy*, vol. 32, no. 3, pp. 359–364, Mar. 2007, doi: 10.1016/j.ijhydene.2006.10.062.
[88] B. Han, S. M. Steen, J. Mo, and F.-Y. Zhang, 'Electrochemical performance modeling of a proton exchange membrane electrolyzer cell for hydrogen energy', *International Journal of Hydrogen Energy*, vol. 40, no. 22, pp. 7006–7016, Jun. 2015, doi: 10.1016/j.ijhydene.2015.03.164.
[89] M. Casey and C. Robinson, 'A Method to Estimate the Performance Map of a Centrifugal Compressor Stage', *Journal of Turbomachinery*, vol. 135, no. 2, Nov. 2012, doi: 10.1115/1.4006590.

[90] O. E. Balje´, ‘A Study on Design Criteria and Matching of Turbomachines: Part A—Similarity Relations and Design Criteria of Turbines’, *Journal of Engineering for Power*, vol. 84, no. 1, pp. 83–102, Jan. 1962, doi: 10.1115/1.3673386.
[91] GAMS Development Corporation, *General Algebraic Modeling System (GAMS) Release 39.3.0*. (2022). Fairfax, VA, USA.
[92] H. Zhang, L. Wang, J. Van Herle, F. Maréchal, and U. Desideri, ‘Techno-economic comparison of green ammonia production processes’, *Applied Energy*, vol. 259, p. 114135, Feb. 2020, doi: 10.1016/j.apenergy.2019.114135.
[93] Terna, ‘Studio sulle tecnologie di riferimento per lo stoccaggio di energia elettrica’, 2023.
[94] S. Samsatli and N. J. Samsatli, ‘A general mixed integer linear programming model for the design and operation of integrated urban energy systems’, *Journal of Cleaner Production*, vol. 191, pp. 458–479, Aug. 2018, doi: 10.1016/j.jclepro.2018.04.198.
[95] P. Marocco, D. Ferrero, E. Martelli, M. Santarelli, and A. Lanzini, ‘An MILP approach for the optimal design of renewable battery-hydrogen energy systems for off-grid insular communities’, *Energy Conversion and Management*, vol. 245, p. 114564, Oct. 2021, doi: 10.1016/j.enconman.2021.114564.
[96] IEA, ‘Renewable Energy Market Update’, 2023.
[97] CAISO, ‘Managing Oversupply’. [Online]. Available: http://www.caiso.com/informed/Pages/ManagingOversupply.aspx
[98] IRENA, ‘Power system flexibility for the energy transition, Part 1: Overview for policy makers’, International Renewable Energy Agency, Abu Dhabi, 2018.
[99] J. López Prol and D. Zilberman, ‘No alarms and no surprises: Dynamics of renewable energy curtailment in California’, *Energy Economics*, vol. 126, p. 106974, Oct. 2023, doi: 10.1016/j.eneco.2023.106974.
[100] IEA, ‘World Energy Outlook 2023’. 2023. [Online]. Available: https://www.iea.org/reports/world-energy-outlook-2023
[101] Y. Zhang, D. Davis, and M. J. Brear, ‘The role of hydrogen in decarbonizing a coupled energy system’, *Journal of Cleaner Production*, vol. 346, p. 131082, Apr. 2022, doi: 10.1016/j.jclepro.2022.131082.
[102] International Energy Agency, *The Role of Low-Carbon Fuels in the Clean Energy Transitions of the Power Sector*. OECD, 2021. doi: 10.1787/a92fe011-en.
[103] European Commission. Directorate General for Energy. and ETIP SNET., *Hydrogen’s impact on grids: impact of hydrogen integration on power grids and energy systems.* LU: Publications Office, 2023. Accessed: Oct. 05, 2025. [Online]. Available: https://data.europa.eu/doi/10.2833/556144
[104] UN SDG, ‘SDG Indicators Metadata repository’. Accessed: Mar. 12, 2024. [Online]. Available: https://unstats.un.org/sdgs/metadata/?Text=&Goal=6&Target=6.4
[105] UN, ‘UN water’. Accessed: Mar. 12, 2024. [Online]. Available: https://sdg6data.org/en/maps
[106] IEA, ‘IEA’. Accessed: Mar. 12, 2024. [Online]. Available: https://www.iea.org/countries
[107] P. H. Gleick, ‘Water and Energy’, *Annual Review of Environment and Resources*, vol. 19, no. Volume 19, pp. 267–299, Nov. 1994, doi: 10.1146/annurev.eg.19.110194.001411.
[108] J. Macknick, R. Newmark, G. Heath, and K. Hallett, ‘Operational Water Consumption and Withdrawal Factors for Electricity Generating Technologies: A

Review of Existing Literature', *Environmental Research Letters*, vol. 7, Oct. 2012, doi: 10.2172/1009674.
[109] J. Meldrum, S. Nettles-Anderson, G. Heath, and J. Macknick, 'Life cycle water use for electricity generation: a review and harmonization of literature estimates', *Environ. Res. Lett.*, vol. 8, no. 1, p. 015031, Mar. 2013, doi: 10.1088/1748-9326/8/1/015031.
[110] Y. Jin, P. Behrens, A. Tukker, and L. Scherer, 'Water use of electricity technologies: A global meta-analysis', *Renewable and Sustainable Energy Reviews*, vol. 115, Nov. 2019, doi: 10.1016/j.rser.2019.109391.
[111] G. Raimondi and G. Spazzafumo, 'Exploring Renewable Energy Communities integration through a hydrogen Power-to-Power system in Italy', *Renewable Energy*, vol. 206, pp. 710–721, Apr. 2023, doi: 10.1016/j.renene.2023.02.074.
[112] G. Glenk, P. Holler, and S. Reichelstein, 'Advances in power-to-gas technologies: cost and conversion efficiency', *Energy Environ. Sci.*, vol. 16, no. 12, pp. 6058–6070, 2023, doi: 10.1039/D3EE01208E.
[113] F. Dawood, M. Anda, and G. M. Shafiullah, 'Hydrogen production for energy: An overview', *International Journal of Hydrogen Energy*, vol. 45, no. 7, pp. 3847–3869, Feb. 2020, doi: 10.1016/j.ijhydene.2019.12.059.
[114] L. Fan, Z. Tu, and S. H. Chan, 'Recent development of hydrogen and fuel cell technologies: A review', *Energy Reports*, vol. 7, pp. 8421–8446, Nov. 2021, doi: 10.1016/j.egyr.2021.08.003.
[115] FAO AQUASTAT, 'FAO AQUASTAT Dissemination System'. Accessed: Mar. 12, 2024. [Online]. Available: https://data.apps.fao.org/aquastat/?lang=en&share=f-faa701cc-a446-466c-b721-aa8dc5c7dd80
[116] E. Assareh and A. Ghafouri, 'An innovative compressed air energy storage (CAES) using hydrogen energy integrated with geothermal and solar energy technologies: A comprehensive techno-economic analysis - different climate areas-using artificial intelligent (AI)', *International Journal of Hydrogen Energy*, vol. 48, no. 34, pp. 12600–12621, Apr. 2023, doi: 10.1016/j.ijhydene.2022.11.233.
[117] X. Xue *et al.*, 'Thermodynamic and economic analysis of new compressed air energy storage system integrated with water electrolysis and H2-Fueled solid oxide fuel cell', *Energy*, vol. 263, p. 126114, Jan. 2023, doi: 10.1016/j.energy.2022.126114.
[118] Ł. Bartela, 'A hybrid energy storage system using compressed air and hydrogen as the energy carrier', *Energy*, vol. 196, p. 117088, Apr. 2020, doi: 10.1016/j.energy.2020.117088.
[119] S. M. Alirahmi, A. R. Razmi, and A. Arabkoohsar, 'Comprehensive assessment and multi-objective optimization of a green concept based on a combination of hydrogen and compressed air energy storage (CAES) systems', *Renewable and Sustainable Energy Reviews*, vol. 142, p. 110850, May 2021, doi: 10.1016/j.rser.2021.110850.
[120] P. Zhao, W. Xu, A. Liu, W. Wu, J. Wang, and X. Wang, 'Assessment the hydrogen-electric coupled energy storage system based on hydrogen-fueled CAES and power-to-gas-to-power device considering multiple time-scale effect and actual operation constraints', *International Journal of Hydrogen Energy*, vol. 48, no. 25, pp. 9198–9218, Mar. 2023, doi: 10.1016/j.ijhydene.2022.12.097.
[121] R. Cao, Y. Wang, W. Li, H. Ni, and Y. Duan, 'Thermodynamics analysis of a hybrid system based on a combination of hydrogen fueled compressed air energy

storage system and water electrolysis hydrogen generator', *International Journal of Hydrogen Energy*, Apr. 2023, doi: 10.1016/j.ijhydene.2023.03.310.
[122] 'Report F. EPRI-DOE Handbook of Energy Storage for Transmission & Distribution Applications. Power 2003;2'.
[123] E. R. Barbour and D. L. F. Pottie, 'Adiabatic Compressed Air Energy Storage Systems', in *Encyclopedia of Energy Storage*, Elsevier, 2022, pp. 188–203. doi: 10.1016/B978-0-12-819723-3.00061-5.
[124] O. Schmidt, A. Gambhir, I. Staffell, A. Hawkes, J. Nelson, and S. Few, 'Future cost and performance of water electrolysis: An expert elicitation study', *International Journal of Hydrogen Energy*, vol. 42, no. 52, pp. 30470–30492, Dec. 2017, doi: 10.1016/j.ijhydene.2017.10.045.
[125] M. E. Ölmez, I. Ari, and G. Tuzkaya, 'A comprehensive review of the impacts of energy storage on power markets', *Journal of Energy Storage*, vol. 91, p. 111935, Jun. 2024, doi: 10.1016/j.est.2024.111935.
[126] F. Oueslati, 'Hybrid renewable system based on solar wind and fuel cell energies coupled with diesel engines for Tunisian climate: TRNSYS simulation and economic assessment', *International Journal of Green Energy*, vol. 18, no. 4, pp. 402–423, Mar. 2021, doi: 10.1080/15435075.2020.1865366.
[127] S. El Hassani, F. Oueslati, O. Horma, D. Santana, M. A. Moussaoui, and A. Mezrhab, 'Techno-economic feasibility and performance analysis of an islanded hybrid renewable energy system with hydrogen storage in Morocco', *Journal of Energy Storage*, vol. 68, p. 107853, Sep. 2023, doi: 10.1016/j.est.2023.107853.
[128] M. Jafarian, E. Assareh, A. Ershadi, and X. Wang, 'Optimal integration of efficient energy storage and renewable sources in hybrid energy systems: A novel optimization and dynamic evaluation strategy', *Journal of Energy Storage*, vol. 101, p. 113880, Nov. 2024, doi: 10.1016/j.est.2024.113880.
[129] K. Trapani, D. L. Millar, and H. C. M. Smith, 'Novel offshore application of photovoltaics in comparison to conventional marine renewable energy technologies', *Renewable Energy*, vol. 50, pp. 879–888, Feb. 2013, doi: 10.1016/j.renene.2012.08.043.
[130] D. Turney and V. Fthenakis, 'Environmental impacts from the installation and operation of large-scale solar power plants', *Renewable and Sustainable Energy Reviews*, vol. 15, no. 6, pp. 3261–3270, Aug. 2011, doi: 10.1016/j.rser.2011.04.023.
[131] N. A. S. Elminshawy, A. Osama, A. Gagliano, E. Oterkus, and G. M. Tina, 'A technical and economic evaluation of floating photovoltaic systems in the context of the water-energy nexus', *Energy*, vol. 303, p. 131904, Sep. 2024, doi: 10.1016/j.energy.2024.131904.
[132] A. Ghosh, 'A comprehensive review of water based PV: Flotavoltaics, under water, offshore & canal top', *Ocean Engineering*, vol. 281, p. 115044, Aug. 2023, doi: 10.1016/j.oceaneng.2023.115044.
[133] P. K. Enaganti *et al.*, 'Experimental investigations for dust build-up on low-iron glass exterior and its effects on the performance of solar PV systems', *Energy*, vol. 239, p. 122213, Jan. 2022, doi: 10.1016/j.energy.2021.122213.
[134] A. Garrod, S. N. Hussain, A. Ghosh, S. Nahata, C. Wynne, and S. Paver, 'An assessment of floating photovoltaic systems and energy storage methods: A comprehensive review', *Results in Engineering*, vol. 21, p. 101940, Mar. 2024, doi: 10.1016/j.rineng.2024.101940.

[135] L. Essak and A. Ghosh, ‘Floating Photovoltaics: A Review’, *Clean Technol.*, vol. 4, no. 3, pp. 752–769, Aug. 2022, doi: 10.3390/cleantechnol4030046.
[136] R. Rebelo, L. Fialho, and M. H. Novais, ‘Floating photovoltaic systems: photovoltaic cable submersion testing and potential impacts’, *Open Res Europe*, vol. 3, p. 61, Apr. 2023, doi: 10.12688/openreseurope.15122.1.
[137] N. Lee *et al.*, ‘Hybrid floating solar photovoltaics-hydropower systems: Benefits and global assessment of technical potential’, *Renewable Energy*, vol. 162, pp. 1415–1427, Dec. 2020, doi: 10.1016/j.renene.2020.08.080.
[138] T. Ma, H. Yang, and L. Lu, ‘Feasibility study and economic analysis of pumped hydro storage and battery storage for a renewable energy powered island’, *Energy Conversion and Management*, vol. 79, pp. 387–397, Mar. 2014, doi: 10.1016/j.enconman.2013.12.047.
[139] S. Ghandehariun, A. M. Ghandehariun, and N. Bahrami Ziabari, ‘Complementary assessment and design optimization of a hybrid renewable energy system integrated with open-loop pumped hydro energy storage’, *Renewable Energy*, vol. 227, p. 120557, Jun. 2024, doi: 10.1016/j.renene.2024.120557.
[140] M. Temiz and N. Javani, ‘Design and analysis of a combined floating photovoltaic system for electricity and hydrogen production’, *International Journal of Hydrogen Energy*, vol. 45, no. 5, pp. 3457–3469, Jan. 2020, doi: 10.1016/j.ijhydene.2018.12.226.
[141] ‘NREL. https://nsrdb.nrel.gov/data-viewer’.
[142] Sun-Earth n.d, ‘Moduli DXM DXP’. [Online]. Available: https://sun-earth.it/prodotti/moduli-dxm-dxp
[143] Enapter, ‘AEM Nexus 1000’. [Online]. Available: https://www.enapter.com/aem-electrolysers/aem-nexus/
[144] O. Gecgel, C. E. Alvarez-Pugliese, J. Solis, and G. G. Botte, ‘Toward net energy-positive ammonia electrolysis: A 3,000 cm2 Bi-Polar electrolyzer for hydrogen production and ammonia remediation’, *International Journal of Hydrogen Energy*, vol. 141, pp. 1349–1358, Jun. 2025, doi: 10.1016/j.ijhydene.2025.03.191.
[145] Department of Energy n.d., ‘Hydrogen Tube Trailers’. [Online]. Available: https://www.energy.gov/eere/fuelcells/hydrogen-tube-trailers
[146] G. Tjarks, A. Gibelhaus, F. Lanzerath, M. Müller, A. Bardow, and D. Stolten, ‘Energetically-optimal PEM electrolyzer pressure in power-to-gas plants’, *Applied Energy*, vol. 218, pp. 192–198, May 2018, doi: 10.1016/j.apenergy.2018.02.155.
[147] C. Moran, P. Deane, S. Yousefian, and R. F. D. Monaghan, ‘The hydrogen storage challenge: Does storage method and size affect the cost and operational flexibility of hydrogen supply chains?’, *International Journal of Hydrogen Energy*, vol. 52, pp. 1090–1100, Jan. 2024, doi: 10.1016/j.ijhydene.2023.06.269.
[148] A. Goswami and P. K. Sadhu, ‘Degradation analysis and the impacts on feasibility study of floating solar photovoltaic systems’, *Sustainable Energy, Grids and Networks*, vol. 26, p. 100425, Jun. 2021, doi: 10.1016/j.segan.2020.100425.
[149] B. Motealleh, Z. Liu, R. I. Masel, J. P. Sculley, Z. Richard Ni, and L. Meroueh, ‘Next-generation anion exchange membrane water electrolyzers operating for commercially relevant lifetimes’, *International Journal of Hydrogen Energy*, vol. 46, no. 5, pp. 3379–3386, Jan. 2021, doi: 10.1016/j.ijhydene.2020.10.244.
[150] N. A. S. Elminshawy, A. Osama, D. G. El-Damhogi, E. Oterkus, and A. M. I. Mohamed, ‘Simulation and experimental performance analysis of partially floating PV system in windy conditions’, *Solar Energy*, vol. 230, pp. 1106–1121, Dec. 2021, doi: 10.1016/j.solener.2021.11.020.

[151] T. A. Gunawan, A. Singlitico, P. Blount, J. Burchill, J. G. Carton, and R. F. D. Monaghan, ‘At What Cost Can Renewable Hydrogen Offset Fossil Fuel Use in Ireland’s Gas Network?’, *Energies*, vol. 13, no. 7, p. 1798, Apr. 2020, doi: 10.3390/en13071798.
[152] H. Bouaboula, M. Ouikhalfan, I. Saadoune, J. Chaouki, A. Zaabout, and Y. Belmabkhout, ‘Addressing sustainable energy intermittence for green ammonia production’, *Energy Reports*, vol. 9, pp. 4507–4517, Dec. 2023, doi: 10.1016/j.egyr.2023.03.093.
[153] IRENA and AEA, ‘Innovation outlook: renewable ammonia’. International Renewable Energy Agency.
[154] R. M. Nayak-Luke and R. Bañares-Alcántara, ‘Techno-economic viability of islanded green ammonia as a carbon-free energy vector and as a substitute for conventional production’, *Energy Environ. Sci.*, vol. 13, no. 9, pp. 2957–2966, 2020, doi: 10.1039/D0EE01707H.
[155] Z. Cesaro, M. Ives, R. Nayak-Luke, M. Mason, and R. Bañares-Alcántara, ‘Ammonia to power: Forecasting the levelized cost of electricity from green ammonia in large-scale power plants’, *Applied Energy*, vol. 282, p. 116009, Jan. 2021, doi: 10.1016/j.apenergy.2020.116009.
[156] Z. Yu, J. Lin, F. Liu, J. Li, Y. Zhao, and Y. Song, ‘Optimal Sizing of Isolated Renewable Power Systems With Ammonia Synthesis: Model and Solution Approach’, *IEEE Trans. Power Syst.*, vol. 39, no. 5, pp. 6372–6385, Sep. 2024, doi: 10.1109/TPWRS.2024.3360315.
[157] L. Edmonds, P. Pfromm, V. Amanor-Boadu, M. Hill, and H. Wu, ‘Green ammonia production-enabled demand flexibility in agricultural community microgrids with distributed renewables’, *Sustainable Energy, Grids and Networks*, vol. 31, p. 100736, Sep. 2022, doi: 10.1016/j.segan.2022.100736.
[158] C. Smith and L. Torrente-Murciano, ‘The importance of dynamic operation and renewable energy source on the economic feasibility of green ammonia’, *Joule*, vol. 8, no. 1, pp. 157–174, Jan. 2024, doi: 10.1016/j.joule.2023.12.002.
[159] N. Salmon and R. Bañares-Alcántara, ‘Impact of process flexibility and imperfect forecasting on the operation and design of Haber–Bosch green ammonia’, *RSC Sustainability*, vol. 1, no. 4, pp. 923–937, 2023, doi: 10.1039/D3SU00067B.
[160] H. Zhao, L. M. Kamp, and Z. Lukszo, ‘The potential of green ammonia production to reduce renewable power curtailment and encourage the energy transition in China’, *International Journal of Hydrogen Energy*, vol. 47, no. 44, pp. 18935–18954, May 2022, doi: 10.1016/j.ijhydene.2022.04.088.
[161] M. Laimon and S. Goh, ‘Unlocking potential in renewable energy curtailment for green ammonia production’, *International Journal of Hydrogen Energy*, vol. 71, pp. 964–971, Jun. 2024, doi: 10.1016/j.ijhydene.2024.05.022.
[162] C. Smith and L. Torrente-Murciano, ‘Cost efficiency versus energy utilization in green ammonia production from intermittent renewable energy’, *Nat Chem Eng*, vol. 2, no. 4, pp. 261–272, Apr. 2025, doi: 10.1038/s44286-025-00207-9.
[163] C. Wang, S. D. C. Walsh, T. Longden, G. Palmer, I. Lutalo, and R. Dargaville, ‘Optimising renewable generation configurations of off-grid green ammonia production systems considering Haber-Bosch flexibility’, *Energy Conversion and Management*, vol. 280, p. 116790, Mar. 2023, doi: 10.1016/j.enconman.2023.116790.
[164] Proton OnSite, ‘High Capacity Hydrogen Systems M Series PEM Electrolyzers’. 2023.

[165] European Central Bank, ‘Euro reference exchange rates’. 2025. Accessed: May 09, 2025. [Online]. Available: https://www.ecb.europa.eu/stats/policy_and_exchange_rates/euro_reference_exchange_rates/html/eurofxref-graph-usd.en.html
[166] A. Franco, C. Carcasci, A. Ademollo, M. Calabrese, and C. Giovannini, ‘Integrated Plant Design for Green Hydrogen Production and Power Generation in Photovoltaic Systems: Balancing Electrolyzer Sizing and Storage’, *Hydrogen*, vol. 6, no. 1, p. 7, Jan. 2025, doi: 10.3390/hydrogen6010007.
[167] Sun-Earth, ‘DXM8-66H/BF 490-505W M8’. Accessed: May 09, 2025. [Online]. Available: https://sun-earth.it/wp-content/uploads/STEEL_DXM8-66H-BF_M8-490-505W_web.pdf
[168] IEA, ‘Global LCOE and Auction values’.
[169] MAXIMATOR GmbH, ‘MAXIMATOR Hulk’. 2024. Accessed: May 06, 2025. [Online]. Available: https://www.maximator.de/flycms/en/web/522/-/Hydro%2BHulc.html

This thesis was produced while attending the PhD programme in Industrial Engineering at the University of Cagliari, Cycle XXXVIII, with the support of a scholarship co-financed by the Ministerial Decree no. 352 of 9th April 2022, based on the NRRP - funded by the European Union - NextGenerationEU - Mission 4 "Education and Research", Component 2 "From Research to Business", Investment 3.3, and by the company Società Chimica Assemini S.r.l.